

MASTER OF SCIENCE THESIS

Improving the Jensen and Larsen Wake Deficit Models

Using a Free-Wake Vortex Ring Model to Simulate the Near-Wake

Johannes Willem van Heemst

June 1, 2015

Faculty of Aerospace Engineering · Delft University of Technology



Challenge the future

Improving the Jensen and Larsen Wake Deficit Models

Using a Free-Wake Vortex Ring Model to Simulate the Near-Wake

MASTER OF SCIENCE THESIS

For obtaining the degree of Master of Science in Aerospace
Engineering at Delft University of Technology

Johannes Willem van Heemst

June 1, 2015



Copyright © Johannes Willem van Heemst
All rights reserved.

Contact: hans@vanheemst.com

Photograph on cover: Middelgrunden wind farm near Copenhagen, Denmark showing Bonus 2.0MW/76 wind turbines. Photo courtesy of Siemens®.

DELFT UNIVERSITY OF TECHNOLOGY

WIND ENERGY RESEARCH GROUP

The undersigned hereby certify that they have read and recommend to the Faculty of Aerospace Engineering for acceptance a thesis entitled "**Improving the Jensen and Larsen Wake Deficit Models**" by **Johannes Willem van Heemst** in partial fulfillment of the requirements for the degree of **Master of Science**.

Dated: June 1, 2015

Chair holder & supervisor:

Prof. dr. G.J.W. van Bussel

Second supervisor:

Ir. D. Baldacchino

Reader:

Dr. ir. M.B. Zaaijer

Reader:

Dr. ir. A.H. van Zuijlen

Summary

The continued grow of the wind industry has resulted in an increase in turbine cluster density in wind farms. This has made the topic of wind turbine and wind farm wake aerodynamics more relevant than ever. Wind turbine wake models are used to predict the deficit and recovery of the wind velocities in the wake. The currently used wake models in the industry contain a relatively simple approach to model the near-wake of the turbine, assuming an initial hat or Gaussian deficit profile at a fixed location in the wake. This thesis presents an alternative near-wake model based on discrete, inviscid, perfectly circular vortex rings for use in conjuncture with existing far-wake models.

A literature study is carried out to determine the current state-of-the-art on wake modelling. This concludes that the Jensen and Larsen models are most suitable for implementation of the Vortex Ring Model (VRM). The Jensen model is limited in physical representation, yet popular in the industry due to its simplicity and low computational cost and presents a good proof of concept. The Larsen model is modular and suitable due to its distinction between near- and far-wake and has an ongoing development, which makes an improvement to the model relevant.

The numerical implementation of the VRM resulted in two different expansion models. A constrained wake expansion, where the vortex rings are simulated as blade tip vortices and a free-wake expansion model where the vortex rings are allowed to contract/expand. The latter uses a smaller timestep to guarantee numerical stability. A comparison with wind tunnel measurements concluded that the free-wake expansion results in a good agreement with the actuator disc represented by a porous mesh in terms of development of wake deficit and expansion. The constrained method results in an overprediction of the wake expansion and was disregarded for use with the Jensen and Larsen far-wake models.

The VRM is coupled to the Jensen model as a preliminary investigation. The VRM is used to determine the axial velocities at the end of the near-wake and to determine the initial induction velocities and expansion for the Jensen model. It is found that at a distance of $2D$, the initial velocity deficit is converged when using $C_T = 5/9$, which gives the smoothest transition. The resultant coupled model predicts a more general wake recovery when compared to the original Jensen model.

The Ainslie and Larsen models are based on the concept of Eddy Viscosity in the far-wake. The Ainslie model uses a Gaussian near-wake approach which was found highly sensitive to atmospheric turbulence. The Larsen near-wake model is based on a stream-tube momentum approach. The Larsen far-wake model was favoured over Ainslie, due to recent development and empirical calibration of the model. The combined VRM-Larsen model generally results in faster wake recovery and an increased shear layer thickness of the wake.

The VRM-Larsen and streamtube-Larsen models were compared against a single and double turbine modelled with an advanced Large Eddy Simulation (LES) code. In both simulations, the VRM-Larsen model is in better agreement with the LES results when compared to the reference Larsen model. The VRM-Larsen model approaches the results of the LES, whilst maintaining an engineering-type computational cost.

The VRM-Larsen model is applied to an array of wind turbines modelling the power deficit for comparison with measurements from the Horns Rev wind farm. The results were inconclusive, since a high uncertainty exists in the 10-minute averaged SCADA data. A comparison with results from the Larsen model implemented in literature shows a significant difference in power output. There are a large number of unknown simulation parameters which could contribute to this difference, which are not covered in the referenced literature.

Nomenclature

Latin Symbols

a	Axial induction factor	[−]
A	Rotor area	[m^2]
b	Wake half width	[m]
C_S	Smagorinsky constant	[−]
C_T	Thrust coefficient	[−]
C_P	Power coefficient	[−]
D	Rotor diameter	[m]
f	Coriolis parameter	[−]
F	Prandtl's tip loss factor	[−]
G	Geostrophic wind speed	[m/s]
h	Hub height	[m]
k	Turbulence kinetic energy	[m^2/s^2]
k	Wake Decay Coefficient	[−]
k_1	Calibration constant (ambient turbulence)	[−]
k_2	Calibration constant (shear layer contribution)	[−]
k_{amb}	Calibration constant (ambient turbulence)	[−]
L	Lift	[N]
N	Number of blades	[−]
p	Pressure	[N/m^2]
P	Power	[W]
r_c	Vortex ring core radius	[m]
R	Rotor radius	[m]
Re	Reynolds number	[−]
t	Time	[s]
T	Thrust	[N]
TI	Turbulence Intensity	[%]
u	Vortex ring axial velocity	[m/s]
U	Axial wind velocity	[m/s]
v_r	Large scale turbulent velocity at the rotor disc (v-direction)	[m/s]

V	Radial wind velocity	[m/s]
w_r	Large scale turbulent velocity at the rotor disc (w-direction)	[m/s]
z_0	Surface roughness parameter	[m]
z_h	Hub height	[m]

Greek Symbols

α	Angle of attack	[°]
Γ	Vortex ring strength	[Nm/s/kg]
ϵ	Turbulence dissipation	[m ² /s ³]
κ	Von Kármán constant	[—]
λ	Tip speed ratio	[—]
μ	Molecular viscosity	[Ns/m ²]
ν_T	Eddy Viscosity	[m ² /s]
φ	Inflow angle of blade	[°]
ρ	Air density	[kg/m ³]
σ	Blade solidity	[—]
ω	Rotational frequency	[rad/s]

Subscripts and Superscripts

∞	Undisturbed
0	Initial
ax	Axial direction
i	Radial position of discretized cell
j	Axial position of discretized cell
m	Mutual
r	Radial direction
s	Self-induced
t	Time instance
z	Axial direction

Abbreviations

AD	Actuator Disc
ADMS	Atmospheric Dispersion Modelling System
AEP	Annual Energy Production
BEM	Blade Element Momentum
CERC	Cambridge Environmental Research Consultants
CFD	Computational Fluid Dynamics
DNS	Direct Numerical Simulation
DTU	Technical University of Denmark
DWM	Dynamic Wake Meandering
ECN	Energy research Centre of the Netherlands
EU	European Union
EV	Eddy Viscosity
EWEA	European Wind Energy Association

GPU	Graphics Processing Unit
I	Instantaneous
LES	Large Eddy Simulation
N-S	Navier-Stokes
OJF	Open Jet Facility
RANS	Reynolds-Averaged Navier-Stokes
SAM	Storpark Analytical Model
SCADA	Supervisory Control And Data Acquisition
TA	Time Averaged
TL	Thin-shear Layer
UPM	Universidad Politécnica de Madrid
VRM	Vortex Ring Model
WAsP	Wind Atlas Analysis and Application Program
WDC	Wake Decay Coefficient

Acknowledgements

A few people are recognized for their help, guidance, patience and devotion towards this research. I would like to thank my supervisors Prof. dr. Gerard van Bussel and Ir. Daniel Baldacchino. Thank you for your patience, understanding, your positive attitude and motivational support towards the end goal.

I am also grateful to Ir. Lorenzo Lignarolo for sharing the results from his measurements in the TU Delft OJF wind tunnel and his insights on the comparison with the near-wake model.

Thank you Wei Yu for your assistance in developing the vortex ring model and helping me out with the puzzle of determining the vortex ring strength.

The Energy research Centre of the Netherlands (ECN) is acknowledged for providing the LES calculations, which provided a very helpful tool in validating the model. A sincere thank you to M.Sc. Dhruv Mehta for his efforts and devotion and thank you for allowing me to disturb your weekends with requests for data updates.

Finally I would like to thank my family for their great deal of patience throughout my studies. Thank you for believing in me and supporting me whenever necessary. Thank you Tanja for all your emotional support and love throughout my studies.

Delft, The Netherlands
June 1, 2015

Johannes Willem van Heemst

Contents

Summary	v
Nomenclature	vii
Acknowledgements	xi
List of Figures	xx
List of Tables	xxi
1 Introduction	1
1.1 Introduction to Wind Energy	1
1.2 Introduction to Wake Modelling	2
1.3 Research Objectives	3
1.3.1 Problem Statement	3
1.3.2 Approach and Research Questions	3
1.3.3 Scope and Framework of the Research	4
1.4 Report Layout	4
2 Current State of Wind Turbine Wake Modelling	5
2.1 Origins of Wake Modelling	5
2.2 Wake Models based on Vorticity	7
2.3 Current State on Far-Wake Modelling	9
2.3.1 Jensen/PARK Model	9
2.3.2 Ainslie Model	10
2.3.3 Larsen / Dynamic Wake Meandering Model	11
2.3.4 WAKEFARM	12
2.3.5 Frandsen / Storpark Analytical Model	13

2.3.6	Atmospheric Dispersion Modelling System (ADMS)	17
2.4	A Note on Computational Fluid Dynamics	18
2.4.1	Reynolds-Averaged Navier Stokes	19
2.4.2	Large Eddy Simulation	19
2.5	Conclusions from the Literature Study	19
3	The Vortex Ring Model	21
3.1	Analytical Expression of the Velocity Field	21
3.2	Vortex Ring Strength and Rotor Shedding	23
3.3	Vortex Ring Translational Velocity	25
3.3.1	Self-Induced Velocity	25
3.3.2	Mutually-Induced Velocity	26
3.4	Wake Expansion Model	27
3.4.1	Constrained Wake Expansion	27
3.4.2	Wake Expansion by Vortex Interaction	28
3.5	Discussion on the Numerical Implementation of the VRM	30
4	Verification and Validation of the Vortex Ring Model	31
4.1	Verification of the Near-Wake VRM	31
4.1.1	Verification with the Axial Induced Velocity	31
4.1.2	Wake Length Sensitivity Study for the Constrained Wilson Expansion	32
4.1.3	Vortex Ring Interaction	34
4.2	Validation with Wind Tunnel Measurements	35
4.3	Remarks on the VRM Validation Study	39
5	Coupling of the Vortex Ring Model with the Jensen Far-Wake Model	41
5.1	Characteristics of the Jensen Far-Wake Model	41
5.2	VRM and Jensen Coupling Methodology	43
5.3	Results of the VRM-Jensen Coupling	44
5.3.1	Single Wake Solutions for $C_T = 8/9$ (Low Turbulence)	45
5.3.2	Single Wake Solutions for $C_T = 5/9$ (Low Turbulence)	47
5.3.3	Single Wake Solutions for $C_T = 8/9$ (High Turbulence)	49
5.4	Conclusions from the VRM-Jensen Results	51
6	Coupling of the Vortex Ring Model with the Larsen Deficit Model	53
6.1	Initial Wake Deficit of the Dynamic Wake Meandering Model	53
6.1.1	Ainslie's Calculation of the Initial Wake Deficit	54
6.1.2	Streamtube Momentum / BEM Model	55
6.2	Far-Wake and the Eddy Viscosity Concept	56
6.2.1	Ainslie's Concept of Eddy Viscosity	57
6.2.2	Larsen's Concept of Eddy Viscosity	58

6.3	Methodology of the Vortex Ring Model and Larsen Coupling	60
6.3.1	Discretizing of the Momentum and Continuity Equations	61
6.3.2	Discretizing at the Boundaries	63
6.4	A Qualitative Study of the Ainslie and Larsen Models	65
6.4.1	Mutually Comparison of the Ainslie and Larsen EV Models	65
6.4.2	Sensitivity to Turbulence of the Ainslie and Larsen Models	68
6.5	Verification of the Larsen Implementation by Comparison with Literature	69
6.6	Results of a Single Wake VRM-Larsen Coupling	71
6.7	Conclusions from the VRM-Larsen Results	73
7	Validation of the VRM-Larsen Model with an LES CFD Model	75
7.1	Description of the LES CFD Model	75
7.2	Comparison of the VRM-Larsen Model with an LES Single Turbine Case	76
7.3	Increased Resolution	79
7.4	Comparison of the VRM-Larsen Model with a Two-Turbine LES Case .	80
7.4.1	Multiple Wake Modelling in the Streamtube-Larsen Model	81
7.4.2	Multiple Wake Modelling in the VRM-Larsen Model	81
7.4.3	Results of the Multiple Wake Simulations with LES	82
7.5	General Conclusions from the LES Comparison	83
8	Power Predictions Compared with Data from the Horns Rev Wind Farm	85
8.1	The Horns Rev Wind Farm	85
8.2	Prediction of Power Output with the Larsen Models	86
8.3	Results of the Horns Rev Simulation and a Comparison with Literature .	87
8.4	Conclusions from the Horns Rev Power Prediction Case	90
9	Conclusion & Recommendations	91
9.1	Reflection on Research Questions	91
9.2	General Conclusions	92
9.3	Recommendations	92
References		95
A	Prandtl's Lifting Line Method	101
B	Overview of Commercial Wake Modelling Software	103
B.1	WAsP	103
B.2	WindPro	104
B.3	WindFarmer	105
B.4	WindFarm	106
B.5	Discussion on Commercial Wake Modelling Software	107
C	Velocity Field Plots of the VRM-Larsen and Larsen Simulations	109
D	Velocity Field Plots of the Double Turbine LES Simulation	113

List of Figures

1.1	2014 Wind energy installations in the EU. Graphs are courtesy of EWEA [44].	2
2.1	Various methods for wake representation using vorticity	8
2.2	Velocity field from the original Jensen model (no wake interaction) with an undisturbed wind speed of 8 m/s and a WDC of 0.04. The colour variations represent the change in wind speed from 0 to 8 m/s.	10
2.3	Illustration of wake meandering. Note that here, v_c represents v_r with small and medium eddies included[32].	11
2.4	Wake Modelling in the Wakefarm model. Picture from [50]	13
2.5	The three regions of the Frandsen Model	14
2.6	Growth of internal boundary layer as function of distance [16]	15
2.7	Wind profile of an infinite large wind farm. Picture from [46]	16
2.8	Schematic of an expanding stream-tube for use within ADMS [53]	17
3.1	Coordinate system used with a vortex ring and an arbitrary point in space	22
3.2	Velocity field induced by a perfect inviscid vortex ring of unit strength and radius	23
3.3	Schematic illustration of an actuator disc shedding a vortex ring	24
3.4	Comparison by Baldacchino [4] of the self-induced velocity as determined with the Kelvin formula and the analytical formulation	26
3.5	Schematic overview for mutually induced velocities	26
3.6	Wilson wake expansion for various values of C_T	28
3.7	Position of the vortex rings along the wake for a large (left) and small timestep (right) visualized by small circles	29
3.8	Comparison of the Wilson wake expansion method and the free wake induced expansion visualised by constant sized circles	30

4.1	Results from a verification study where the induced velocities at the position of the actuator disc are studied	32
4.2	Graph showing the influence of simulated wake length on the velocities on the centreline for $C_T = 1/2$	33
4.3	Graph showing the influence of simulated wake length on the velocities on the centreline for $C_T = 8/9$	33
4.4	Position of vortex rings plotted showing the vortex ring interaction. Lower C_T values result in a more stable wake, with interaction starting at a further distance compared to higher values for C_T	34
4.5	Comparison of the near-wake VRM (Wilson constrained expansion method) with wind tunnel measurements showing velocity profiles of the porous disc, two-bladed turbine, time-averaged VRM and instantaneous VRM	36
4.6	Comparison of the near-wake VRM (Induced free-wake expansion method) with wind tunnel measurements showing velocity profiles of the porous disc, two-bladed turbine, time-averaged VRM and instantaneous VRM	36
4.7	Comparison of centreline velocities between the wind tunnel data and the model	37
4.8	Non-dimensionalised velocity fields from the experimental results of the 2-bladed turbine and porous disc. Overlaid are the positions of the vortex rings of both expansion models after the simulation	38
5.1	Schematic overview of the Jensen far-wake model	42
5.2	Schematic overview of the VRM-Jensen coupling	44
5.3	Velocity field of a turbine with $C_T = 8/9$ from a VRM-Jensen simulation .	45
5.4	Velocity field of a turbine with $C_T = 8/9$ from a standard Jensen simulation	45
5.5	Velocities along the centerline with $C_T = 8/9$ for the VRM-Jensen coupling and the standard Jensen simulation	46
5.6	Velocities profiles for $C_T = 8/9$ for the VRM-Jensen coupling and the standard Jensen simulation	46
5.7	Velocity field of a turbine with $C_T = 5/9$ from a VRM-Jensen simulation .	47
5.8	Velocity field of a turbine with $C_T = 5/9$ from a standard Jensen simulation	47
5.9	Velocities along the centerline with $C_T = 5/9$ for the VRM-Jensen coupling and the standard Jensen simulation	48
5.10	Velocities profiles for $C_T = 5/9$ for the VRM-Jensen coupling and the standard Jensen simulation	48
5.11	Velocity field of a turbine with $C_T = 8/9$ from a VRM-Jensen simulation with turbulence	49
5.12	Velocity field of a turbine with $C_T = 8/9$ from a standard Jensen simulation with turbulence	49
5.13	Velocities along the centerline with $C_T = 8/9$ for the VRM-Jensen coupling and the standard Jensen simulation with turbulence	50
5.14	Velocities profiles for $C_T = 8/9$ for the VRM-Jensen coupling and the standard Jensen simulation with turbulence	50
6.1	Schematic of the Wake Deficit model in the Dynamic Wake Meandering Model	54
6.2	Example of a Gaussian velocity profile for $C_T = 8/9$ and $A = 10\%$	55

6.3	Schematic Representation of the near-wake	56
6.4	The filter functions from Ainslie and Keck for the atmospheric part of the Eddy Viscosity	60
6.5	Overview of the grid on which the derivatives are discretized	62
6.6	Results from an Ainslie-Larsen comparison with $C_T = 8/9$ and $TI = 0\%$.	66
6.7	Results of a Ainslie-Larsen comparison with $C_T = 5/9$ and $TI = 0\%$. .	67
6.8	Results of a Ainslie-Larsen comparison with $C_T = 8/9$ and $TI = 21\%$. .	68
6.9	Centreline velocities for the Ainslie model (left) and the Larsen model (right) for $C_T = 8/9$ and various values for TI	69
6.10	A comparison of results by Madsen et al. [37] (left) and the implemented model (right) with a uniformly loaded actuator disc of $C_T = 8/9$ in laminar flow	70
6.11	Comparison of the influence of ambient turbulence on the development of the axial velocity deficit downstream at $r/R = 0.8$	70
6.12	Comparison of axial velocities at various radial positions with $U_\infty = 10m/s$ and $TI = 6\%$. The figure left shows a comparison by Keck et al. [28] between the DWM and an actuator line CFD model. The right graph shows results from the discussed streamtube-Larsen implementation.	71
6.13	Simulation results of the VRM-Larsen and BEM-Larsen wake models with $C_T = 8/9$ and $TI = 0\%$	72
6.14	Simulation results of the VRM-Larsen and BEM-Larsen wake models with $C_T = 5/9$ and $TI = 0\%$	72
6.15	Simulation results of the VRM-Larsen and BEM-Larsen wake models with $C_T = 8/9$ and $TI = 25\%$	73
6.16	Simulation results of the VRM-Larsen and BEM-Larsen wake models with $C_T = 5/9$ and $TI = 25\%$	73
7.1	Axial velocities in the down-wake direction from the Larsen, VRM-Larsen and LES computations	77
7.2	Vortex ring positions in the near-wake	77
7.3	Wake profiles at various down-wake positions from the Larsen, VRM-Larsen and LES computations	78
7.4	Axial velocity fields of the Streamtube-Larsen, VRM-Larsen and LES results	79
7.5	Results from the LES actuator disc model where the effective resolution of the grid is doubled	80
7.6	Schematic overview of a multiple wake approach in the VRM-Larsen model	82
7.7	Axial velocities in the down-wake direction from the Larsen, VRM-Larsen and LES double turbine computations	83
8.1	Turbine lay-out of the Horns Rev wind farm. Figure courtesy of Gaumond et al. [17]	86
8.2	Photograph of the Horns Rev wind farm showing wake effects visualised by local condensation. Photo by Steiness [52].	86
8.3	Axial velocities along the centreline of the Horns Rev case simulated with the streamtube-Larsen and VRM-Larsen models	87
8.4	Axial velocity fields of the Horns Rev simulations	88

8.5 Normalised power predictions compared with measurements	89
A.1 Horseshoe Vortex as a result of a finite wing	101
A.2 Superposition of Horseshoe vortices resulting in the lifting line	102
B.1 Example of CFD Mesh creation in the new WAsP 11 program. Picture from wasp.dk	104
B.2 Overview of the available modules for WindPro. Picture from emd.dk	105
B.3 Screenshot of the basic WindFarmer module. From the Windows 98 layout, it is assumed to be an older version. Picture from www.gl-garradhassen.com	106
B.4 Wake Model options in the WindFarm program. Picture from www.resoft.co.uk	107
C.1 Velocity field of a turbine operating at $C_T = 8/9$ in $TI = 0\%$ from the Larsen model	109
C.2 Velocity field of a turbine operating at $C_T = 8/9$ in $TI = 0\%$ from the VRM-Larsen model	109
C.3 Velocity field of a turbine operating at $C_T = 5/9$ in $TI = 0\%$ from the Larsen model	110
C.4 Velocity field of a turbine operating at $C_T = 5/9$ in $TI = 0\%$ from the VRM-Larsen model	110
C.5 Velocity field of a turbine operating at $C_T = 8/9$ in $TI = 25\%$ from the Larsen model	110
C.6 Velocity field of a turbine operating at $C_T = 8/9$ in $TI = 25\%$ from the VRM-Larsen model	111
C.7 Velocity field of a turbine operating at $C_T = 5/9$ in $TI = 25\%$ from the Larsen model	111
C.8 Velocity field of a turbine operating at $C_T = 5/9$ in $TI = 25\%$ from the VRM-Larsen model	111
D.1 Velocity field two turbines operating at $C_T = 8/9$ in $TI = 0\%$ from the LES model	113
D.2 Velocity field two turbines operating at $C_T = 8/9$ in $TI = 0\%$ from the VRM-Larsen model	114
D.3 Velocity field two turbines operating at $C_T = 8/9$ in $TI = 0\%$ from the streamtube-Larsen model	114

List of Tables

4.1	Parameters of the Wind Tunnel Experiment. Values extracted from Lig-narolo et al. [36]	35
5.1	An estimated relation between TI and k from Choi and Shan [9]	42
6.1	Referenced values for k_{amb} and k_2	60
6.2	Discretized derivatives from the Momentum and Continuity equations	61
6.3	Discretized derivatives at the boundaries	65
6.4	Variables in the VRM - Far-wake coupling	65
7.1	Parameters used in the single and double turbine LES calculations	76
8.1	Parameters used in the Horns Rev wake simulation	87
B.1	Commercial Software Packages	108
B.2	Price Comparison of Commercial Wake Modelling Software	108

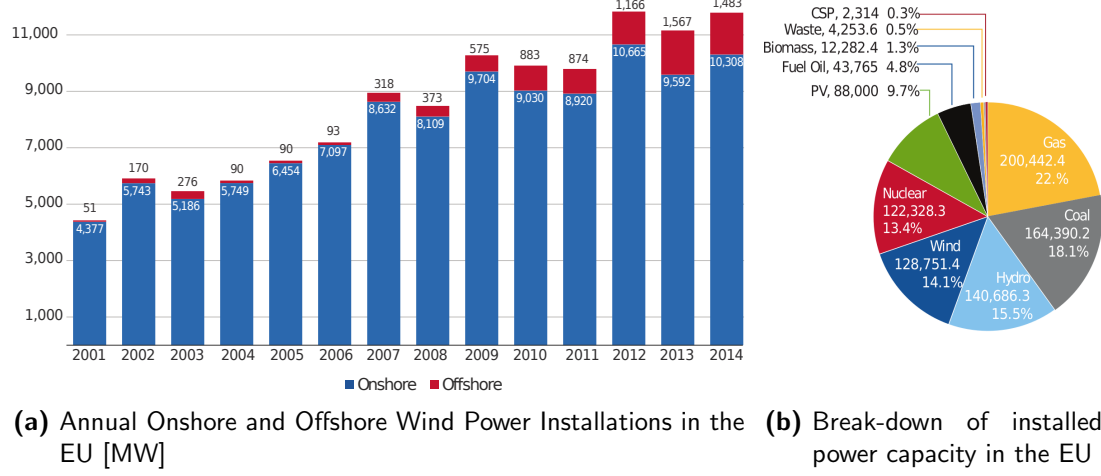
Chapter 1

Introduction

1.1 Introduction to Wind Energy

In the past fifteen years, wind energy has experienced a global growth of installed capacity. The growthspurt has proven to be independent of the global decrease of economy and the rate of installations of new wind turbines has grown nonetheless. In 2014, 44% of new power installations in the European Union (EU) were wind turbines, which is 55% of newly installed renewable energy providers [44]. An energy break-down displayed in figure 1.1b, shows that 14% of all electrical power generating capacity in Europe, is attributed to wind turbines. This increase is observed both onshore and offshore, see figure 1.1a. This figure shows, that the majority of turbines in the European Union is installed on land. However, offshore wind has had a growth of 34% in 2013, and although the same growth was not experienced in 2014, this trend is expected to continue. This development has led to a healthy market with investments, competition and innovation of wind farm and turbine design.

A growing trend is observed in offshore wind farm development. In 2010, the average wind farm size was 155.3 MW, with an average wind turbine capacity of 3.2 MW [58]. This has grown to a mean wind farm size of 485 MW with 4 MW turbines on average [10]. It has resulted in an increase of number of turbines per offshore wind farm. With this increase of wind turbines per wind farm, wake effects and wind farm aerodynamics in offshore conditions have become a more important research aspect.



(a) Annual Onshore and Offshore Wind Power Installations in the EU [MW] (b) Break-down of installed power capacity in the EU

Figure 1.1: 2014 Wind energy installations in the EU. Graphs are courtesy of EWEA [44].

1.2 Introduction to Wake Modelling

The increase in cluster density in wind farms has stimulated the research in wind turbine rotor aerodynamics for the past 10 years. A highly active research topic in rotor aerodynamics is wake modelling. Wake modelling is a research area in which the flow behind a wind turbine rotor is described and predicted with the use of mathematical or physical models. A distinction can be made between models that focus on the area close to the rotor (near-wake) and models that focus on the area far beyond the rotor (far-wake). The near-wake is generally described by the deceleration of the wind velocity due to energy extraction of the rotor and pressure recovery. Other features describing the near-wake are blade tip vortices travelling downstream in a stable manner. The far-wake is characterized by instability of tip vortices and wake recovery and is considered turbulent. Other phenomena observed in the far-wake are wake meandering and shear due to the atmospheric boundary layer.

Wake models have developed from simple linear models developed in the 1980's [23], towards complex numerical models based on 3D Navier-Stokes equations [48]. Wake models can be used as a research tool to study particular wake effects, for instance wake meandering [32], the existence of the ground or the influence of terrain roughness on wake recovery [20]. Wake models are also used in the industry as a tool for wind turbine design and wind farm development, for instance to predict wake added turbulence to determine turbine blade loads or predict the wake deficit to determine wake losses and the Annual Energy Production (AEP). These models are often referred to as engineering models and focus more on computational efficiency, rather than accuracy.

Recent research in near-wake wake modelling by Baldacchino and van Bussel [5] and Micallef et al. [41] have shown that a vortex ring model could serve as an excellent tool to simulate induced velocities in the near-wake. In this model, the shed vorticity from the rotor is concentrated in infinitely thin, perfectly circular discrete tip vortex rings, which are free to travel and interact down-wake.

1.3 Research Objectives

1.3.1 Problem Statement

Current research on wind turbine wake tends to strive more towards an increased accuracy in the far-wake by focussing on viscous effects, wake meandering and the influence of turbulence. This has decelerated development in near-wake prediction models, simply because they are considered less important to the far-wake phenomena. The majority of far-wake models use a simple near-wake modelling technique, which is based on squared hat or Gaussian profiles, that follow from the actuator disc momentum theory or empirical data. The main problem with this approach is that the development of the deficit is not determined, rather assumed at a fixed position, for instance immediately after the rotor ($0D$), neglecting the near-wake completely or at $2D$ where it is assumed that the pressure has recovered. A bladed element momentum (BEM) approach provides a better alternative [37], but requires a high amount of blade parameters as input.

Engineering models used to calculate wake losses in wind farms strive to predict wind velocities in the wake as accurate as possible, they are however limited in the near-wake to the same models. This has led to the use of computational expensive numerical models based on Computational Fluid Dynamics (CFD). CFD provides accurate wake predictions, but requires relatively much computational power with respect to the more commonly used engineering wake models.

A near-wake model based on vortex rings could provide a better alternative to the commonly used far-wake models. The benefit is a model where the deficit is calculated in time and space, rather than an assumed position. This could lead to a better picture of the total wake field with respect to the currently used near-wake models. If so, it is an alternative to CFD, being less accurate, but much faster. The Vortex Ring Model (VRM) would also have a more physical meaning, compared with the currently used near-wake models.

1.3.2 Approach and Research Questions

The problem stated previously has given rise to the following research questions, which will be addressed in this thesis:

1. From the state-of-the-art on wake modelling, what are wake models that could benefit from a different simulation of the near-wake?
2. Is it possible to accurately simulate the near-wake with inviscid perfect vortex rings?
3. How can the near-wake vortex ring model interact with the far-wake models from research question 1?
4. Are the results of this interaction similar to results of the original far-wake model?

1.3.3 Scope and Framework of the Research

This research focusses on coupling a vortex ring model with suitable far-wake models, selected from a literature study. The VRM is validated with wind tunnel measurements and the combined model is validated with an advanced LES model. A multiple wake case study is carried out, but the model is not optimized for this case. The LES code is provided by ECN and is not developed in this research.

The work presented in this report is the result of a master thesis research carried out in obtaining the degree of Master of Science in Aerospace Engineering. The work was carried out at the Delft University of Technology at the faculty of Aerospace Engineering. The Master Track that was followed in preparation of this research is the ‘Aerodynamics & Wind Energy’ track, with the ‘Wind Energy’ profile courses.

1.4 Report Layout

After the introducing chapter, an overview of current literature is presented in Chapter 2. This chapter provides an overview of the state-of-the-art on wake modelling. Various kinds of wake models are elaborated and evaluated. This provides basic background knowledge, to which is referred to throughout this report.

Chapter 3 gives an extensive explanation on the derivation of the near-wake vortex ring model which is used in this research. The chapter explains the determination of the induced velocity field, the strength and velocity of the ring and how expansion in the wake is handled. This model is then verified and validated in Chapter 4. In this chapter, the numerical results of the model are checked and the induced velocity field is validated against experimental wind tunnel results.

The VRM is coupled with the Jensen far-wake model, which is described in Chapter 5. This chapter discusses the methodology of the coupling and shows simulation results, which are compared with the original reference Jensen model.

Chapter 6 describes the coupling of the VRM with the wake deficit model used in Larsen’s Dynamic Wake Meandering Model, which is based on the concept of Eddy Viscosity. The discretization of the model on the grid is explained and results are shown, where the VRM-Larsen combination is compared with the Larsen reference model and the Ainslie wake deficit model.

The results of the VRM-Larsen coupling are compared against numerical CFD calculations based on LES. The result and some background on the LES model are presented in Chapter 7. This chapter gives some closure on the benefit of replacing the near-wake model with vortex rings.

The VRM-Larsen is applied to a row of turbines representing the Horns Rev wind farm. Power predictions of the turbines are compared with literature and discussed in Chapter 8.

Final conclusions, discussion on the results and recommendations for future work are presented in Chapter 9, which concludes this report.

Chapter 2

Current State of Wind Turbine Wake Modelling

A literature study was carried out to gain insight in wake modelling and the current state-of-the-art on the subject. The results are laid-out in this chapter. An introduction and brief history of wake modelling can be found in section 2.1. A summary and explanation on using the concept of vorticity to formulate velocities in the wake is described in section 2.2. An extensive overview of current far-wake models is displayed in section 2.3 and a note on CFD in section 2.4. Finally, a conclusion from this study with a subsequent research hypothesis is presented in section 2.5.

2.1 Origins of Wake Modelling

Wake modelling has a larger history than is generally thought. Its origins are in the early days of rotor aerodynamics and ship propeller hydrodynamics. At the end of the 19th century, research was performed to improve the efficiencies of ship propellers. Fraude, Taylor and Drzewiecki developed the Blade Element Theory, initially designed to determine the performance and behaviour of ship propellers, but widely used for aerodynamic propellers. Later, conservation of momentum was added to the model to create the Blade Element Momentum Theory (BEM). This was subsequently used as a design tool to improve aircraft propellers.

A milestone in rotor aerodynamics was achieved by Albert Betz in 1919. He used the momentum theory or actuator disk theory to prove that a maximum exists of the amount of power that can be extracted from, or added to, a uniform flow field. This limit is called the “Betz Limit”¹. The derivation proves that the maximum power coefficient achievable is 16/27, or 59.3%. This means that no matter what kind of device is used to extract

¹The Betz limit is also referred to as the Joukowsky-limit. A paper by Okulov & Van Kuik[42] suggests to rename the limit to the “Betz-Joukowski Limit”.

energy from the wind, only roughly 60% of the energy can physically be retrieved. Modern wind turbines operate roughly with a maximum C_p between 20 and 40%.

Wake modelling development can globally be divided in three research areas:

1. Short-term energy forecasting
2. Turbine and farm design
3. Academical research in wake dynamics

Short-term energy forecasting models are mainly used in wind turbine asset management. In order to regulate power supply and demand, wind turbine owners are obliged to provide an estimate of the power production of the upcoming day. This information is parsed towards the grid manager, who decides how much power from conventional sources (gas turbine, coal) is required. If the actual supply is far off from the predicted values, financial penalties can be imposed. Therefore short-term atmospheric models are used to predict the electricity output of the upcoming day. Short-term thus refers to a period of 24-72 hours. Although these models are mainly atmospheric and weather prediction models, the wake losses are dependent on the particular wind direction and wind speed, thus wake modelling is also involved in this process. Landberg et al. [31] provides an excellent overview of commonly used systems in the industry in his paper “*Short-Term Prediction - An Overview*”. He clearly distinguishes several building blocks on which most models are based (e.g. Weather Prediction Model, Geography/Wind Farm Layout, Roughness model). This makes the prediction system modular. A published paper by Kariniotakis et al. [24] should also be mentioned, since this provides a good state-of-the-art on short-term prediction as well. It categorizes short-term models in physical and statistical models. The former category describes wake models which are based on the laws of physics, while the latter are purely mathematical models based on empirical data from measurements.

Wake modelling is used in wind turbine design to model the loads at the rotor. One of the driving design factors is the turbulence in the wind field. Therefore wake models that incorporate turbine wake added turbulence to the field are used in this area. In the development phase of a wind farm, multiple turbine lay-outs are designed and the Annual Energy Production (AEP) is estimated to help decide which lay-out will be more profitable. Due to wake losses, at a certain point it is economically infeasible to add more turbines to a restricted area, since the cost will be higher than the revenue of the extra turbine. Wake models used for wind turbine and wind farm design are often called “Engineering Models”. Energy yield prediction models have a high importance in the wind turbine industry. The result is that consultancies have specialized to determine the AEP as accurate as possible from a proposed turbine layout. This commercialisation of analytical wake models to software packages used in the industry are discussed in Appendix B

Finally, wake aerodynamics research has been carried out before wake modelling was a vital part of wind farm design. Wake models have proven to be a valuable tool for research into wake aerodynamics and in this context, many wake models have been derived. Academic research have led to models used to investigate wake interaction, ground effect,

wake stability or turbulence mixing. Initially developed for a greater understanding in rotor aerodynamics and wake velocity field simulation, many of these models turned out to have a great potential for engineering purposes. For instance, the Larsen model as discussed in Chapter 6 was developed to investigate the meandering phenomenon of the wake, but is later used as a wake loss prediction model.

2.2 Wake Models based on Vorticity

Vorticity can best be described as the angular momentum of the flow [3]. It has been a widely used flow property for researching aerodynamics. Vorticity can also be used to describe induced velocities by the rotor. An excellent document on vorticity based models was published by Stock [54] in 2007. His “Summary of Vortex Methods Literature” provides an excellent overview of all vortex models.

The most well-known example of a vorticity based model is the Prandtl Lifting Line Method². This method to predict the aerodynamic properties of a finite wing, was developed by Ludwig Prandtl between 1911 and 1918 [3].

Currently, the concept of a lifting line has not been used to model the wake of a wind turbine directly, but is indirectly used, since the principle of a lifting line is used in other vortex distribution methods as well. For instance, a way to model the vorticity induced by a finite wing, is by discretizing the wing into a number of panels. Each panel or ‘lifting surface’ induces a certain vorticity. By implying boundary conditions on each panel, the vorticity strength of each panel can be determined. The total vorticity induced by the wing can than be obtained by integrating these vorticities over the complete area. An advantage of this method is that the majority of the calculations can be done with linear algebra (requiring vector and matrix notations), which increases the speed of the method. An in-depth explanation of this method can be found in Katz and Plotkin [26].

A similar approach was done by Kloosterman [29]. Here, the near-wake of a wind turbine was modelled with a lifting line induced sheet. The rotor is modelled by a single horse-shoe vortex. Due to the rotation of the blade, the tip vortices follow a helical path with a rotation opposite of the rotor. This leads to the concept of a tubular vortex sheet. Kloosterman’s model performs well within the first diameter downstream of the rotor, providing a fine first order prediction, which can subsequently be used for near-wake prediction for far-wake models. The downside of the model is the relatively great amount of computational power required. The quantity of the required calculation power is unfortunately unclear from the thesis.

A curved vortex lifting line for implementation in 3D was first done by Couët and Bune-man [11]. Such a method is referred to as a curved vortex filament discretization. A good review paper on this was published by Widnall [57] in 1972. It presents the instability modes of a helical vortex filaments and contains a lot of references to earlier work. More recent work is performed by Knio and Klein [30]. Their improvements to the thin-tube model represents the filaments more accurately. This approach was recently applied to model the wake of offshore floating wind turbines by Beyer et al. [7]. Due to the rotating

²The Prandtl Lifting Line Theory is also called the ‘Lanchester-Prandtl Wing Theory’ since it was independently derived by Frederick Lanchester in the same time period [3].

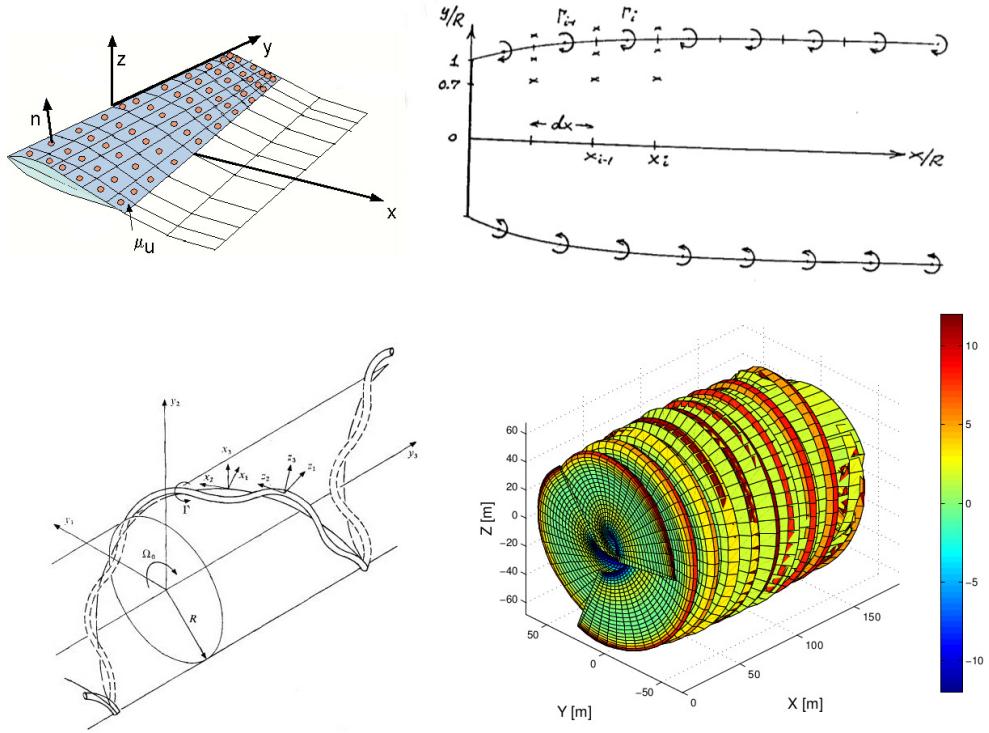


Figure 2.1: Various methods for wake representation using vorticity. Upperright: Vortex rings, picture from [43]. Lowerleft: Curved vortex filament, picture from [57]. Lowerright: Lifting line sheet, picture from [29].

nature of the offshore platform, it was well-suited to cope with the multiple Degrees of freedom present in the system. The model is still being developed, but early validation reports where the curved filament was imitated by discretizing the curved filament in straight vortex filaments have shown that the model is feasible.

The first milestone in wind turbine wake modelling with the use of vortex rings was by the work of Stig Øye in 1989 [43]. He developed a model to describe the wake of a wind turbine by describing the tip vortex as equally spaced, separated vortex rings, combined with a single vortex line created by the root vortices (see figure 2.1). He assumed a uniform disc loading, related thrust and induced velocity and compared the result with those from the ordinary streamtube-momentum method. His findings were that the difference was surprisingly small. Yoon and Heister [60] provided analytical methods to describe the velocity field due to vortex rings. In their paper they provided an analytical solution for any arbitrary point in the velocity field by direct evaluation of the Biot-Savart law. Micallef et al. [41] used this method and adapted the rings to oblique vortex rings to model the shear flow of a wind turbine. The vortex ring model was furthermore used by Baldacchino [4] to investigate ground effects in the wake. Yoon, Micallef and Baldacchino have shown that a model based on vortex rings has proven its usefulness for a near-wake research model. It is possible to investigate wake phenomena, as well as providing a first order near-wake velocity field. The principles of near-wake modelling with vortex rings is

extensively elaborated in Chapter 3.

2.3 Current State on Far-Wake Modelling

This section presents an overview of current wake models that are specifically derived for use in the far-wake. This provides a better understanding of the physical differences between the models. Special attention is divided to the near-wake and the transition from near- to far-wake within the model. In some cases, there is no near-wake modelling at all and assumptions are placed. In other models, a separate near-wake simulation is carried out.

2.3.1 Jensen/PARK Model

The Jensen or PARK model was derived by N.O. Jensen [23] in 1983 and shortly after improved by Katic et al. [25]. It is a basic model which assumes a linear diverging wake and a hat-shaped wake profile. Although dated, it is a widely used model, often praised for its simplicity and ease of application, which gives ample opportunities for validation. This explains why the model is still being used today and researchers are still striving to improve the model.

The model features a linear wake expansion which is based on the terrain roughness. An instant velocity deficit is assumed at the position of the turbine. Figure 2.2 shows the turbine wake simulated with the original Jensen Model, applied to multiple turbines in a wind farm layout. An extensive elaboration on the derivation of the Jensen model can be found in Chapter 5.

A noteworthy mention is the recent update to the model by Choi and Shan [9]. He made three advancements to the model, which are:

1. Partial wake interaction: A method for wake interaction to make the model more suitable for large wind farms.
2. Yaw Misalignment: Predicting a more accurate wake field in yawed flow situations.
3. Adjustment for unsteady wind: A correction for small wind direction changes in the time domain.

Over the years the model has been thoroughly validated. Overall, the model performs very well for a single turbine case. A benchmark study performed by Gaumond et al. [17] proved that the model is still a suitable choice for first order estimations.

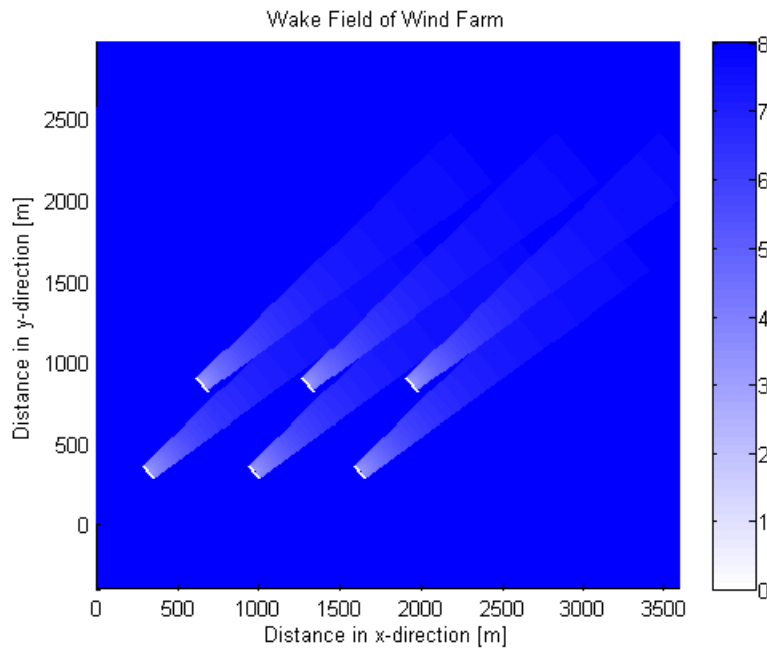


Figure 2.2: Velocity field from the original Jensen model (no wake interaction) with an undisturbed wind speed of 8 m/s and a WDC of 0.04. The colour variations represent the change in wind speed from 0 to 8 m/s.

2.3.2 Ainslie Model

The Ainslie model was published in 1988 by J.F. Ainslie [2]. Ainslie derived his model by considering a two dimensional axi-symmetric field model. It assumes a Gaussian shaped wind profile in the near-wake and the initial velocities are calculated from empirical data, based on the atmospheric turbulence. He derived the equations for the flow field with the continuity and momentum equations. A thin shear layer approximation is used and the viscous stresses are modelled with the concept of Eddy Viscosity (EV). Therefore, the model is often referred to as the Eddy Viscosity model.

In the near-wake (up to $5D$), a filter function is applied to correct for the lack of equilibrium between the mean velocity field and the turbulence field in the near-wake region. The flow field can than be solved with a finite difference scheme. Derivation and implementation of the model is extensively elaborated in Chapter 6, which also describes how the model is discretized on a grid.

The model is re-used in the Larsen model discussed in section 2.3.3 and recalibrated for this purpose by Madsen et al. [37] and Keck et al. [28]. Their calibration is focussed on the formulation of the Eddy Viscosity Concept and the filter function which is split in an atmospheric turbulence part and the mean velocity difference across the wake. It is explained in detail in section 6.2.

2.3.3 Larsen / Dynamic Wake Meandering Model

The Larsen model is a relatively new model which was derived in 2007 and published in 2008 [34]. The aim of the model was to study the meandering phenomenon of the wake, therefore the model is named the “Dynamic Wake Meandering model” (DWM). The model includes a wake deficit model, a wake meandering model and a turbine added turbulence model. All three models are modular and can be replaced by a different model if preferred.

The Risø report [32] states that in a prototype versions of the model, the wake deficit was estimated with a CFD based actuator disc. However, to increase the calculation efficiency, it was replaced by engineering type models; A boundary layer approach and a vorticity formulation of the wake.

The vorticity formulation consists of piecewise linear vortex curves. The results of this approach were promising according to the report, however the model was disregarded, since the non-locality of the Biot-Savart law made computational requirements increase drastically for far-wake distances. The report mentioned however, that the model could serve as an input model for the boundary layer approach.

The boundary layer approach is similar to the Eddy Viscosity model. The report suggests that this is the best suitable approach and later publications on the Larsen model have confirmed this [27]. The final version of the wake deficit model was a combination of a streamtube momentum based near-wake model and the far-wake Eddy Viscosity concept. It is explained in more detail in section 6.2.

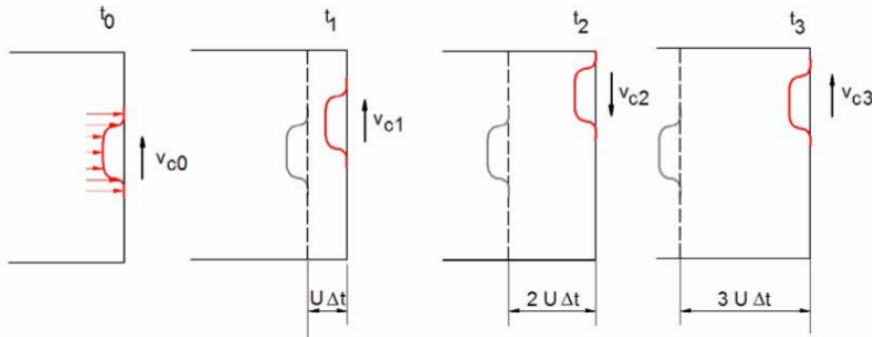


Figure 2.3: Illustration of wake meandering. Note that here, v_c represents v_r with small and medium eddies included[32].

The wake meandering model of the DWM is based on the assumption that the wake acts as a passive tracer of large-scale turbulence structures. The dynamic behaviour is modelled with the following set of differential equations:

$$\frac{dy(t, t_0)}{dt} = v_r(t_0) \quad (2.1)$$

$$\frac{dz(t, t_0)}{dt} = w_r(t_0) \quad (2.2)$$

Here, v_r and w_r represent the large-scale turbulent velocities at the rotor disc. The motion in v -direction is displayed in figure 2.3. The set of equations assumes the turbulence spatial

to be homogeneous, thus only large-scale lateral- and vertical velocities over the rotor are considered. To achieve this, a low pass filter is applied to only capture the large scale eddies.

Literature on the turbulence models of the Larsen model are quite extensive. Turbine added turbulence models range from analytical models, such as the J-Model (basic) and O-model (more detailed), through Numerical CFD Models towards stochastic models (Proper Orthogonal Decomposition and spectral approaches) [32]. The reader is advised to check the references of this paper for more information on these turbulence models. Currently, newer turbulence models for the Larsen model are still being developed, with recent work published in 2013 by Keck et al. [27].

The Larsen model is an interesting model in the scope of this literature research. The history of the model suggests that a combination with a more accurate near wake description (compared to the assumed Gaussian profile in the Eddy Viscosity approach) could improve the model as was suggested by Larsen.

2.3.4 WAKEFARM

ECN's Wakefarm model was derived from the UPMWAKE model from the Universidad Polytechnica de Madrid (UPM) and first published by Crespo et al. [12]. The original code was based on seven partial differential equations, being conservation of mass, conservation of momentum (in three directions), energy, turbulent kinetic energy and the dissipation rate of the turbulent kinetic energy. It is then assumed that there is no velocity in transverse direction ($2D$) and the adiabatic temperature gradient is constant. This simplifies the model to only three equations: conservation of momentum (axial), conservation of kinetic energy and the turbulence dissipation rate.

The model was transferred to ECN in the 1990's and there the model evolved into the better-known Wakefarm code [49]. The main difference between the UPMWAKE and the Wakefarm code lies in the near-wake modeling. Later, the Wakefarm code has been integrated into the Farmflow [50] wind farm design code. A standalone software program with the implementation of the Wakefarm code has also been released under the name Fluxfarm [8] and Farmflow [50].

ECN uses the original 7 equations from the UPMWAKE code and includes the original $k - \epsilon$ turbulence model. Furthermore, some improvements have been made regarding the original code which are discussed in this section. A sketch explaining the basic working principle of the model can be seen in figure 2.4.

The near-wake was originally modelled with an empirical initial velocity profile. In the new model, the starting condition for the wake model is formed by a velocity profile, which is calculated in the rotor plane based on induced velocities obtained from the momentum equation [50]. A Gaussian profile was also considered, but disregarded due to the necessity of tuning parameters, while the former approach is analytic.

The wake expansion is based on the pressure gradient, which is calculated from a separate free vortex wake model. This model assumes axi-symmetry and models the rotor as an actuator disc. To save computational resources, a database is created with the values of the pressure gradient, which only depends on the axial induction factor.

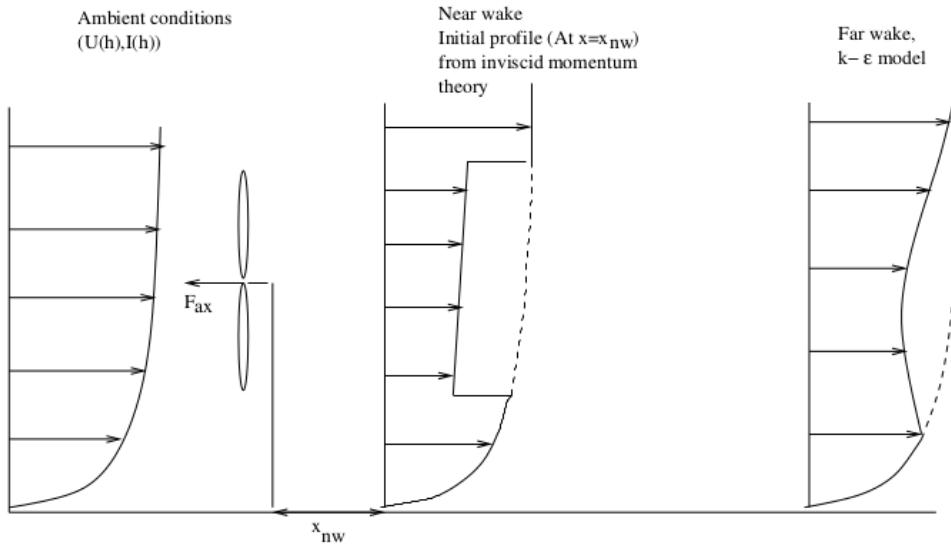


Figure 2.4: Wake Modelling in the Wakefarm model. Picture from [50]

The Wakefarm code supports multiple wake situations. As a first step the wake of the upwind turbine is calculated. The wake parameters (wind velocity, turbulence intensity, pressure etc.) are basically transferred into the rotor plane of the second turbine. This forms the starting condition of the wake of the second turbine.

It is understandable that the reader has lost track of the various names of the model in this section, very much like the author had in researching this model. It is therefore perhaps beneficial to give an overview of the original and new names.

- UPMCODE is the original name from the University of Madrid. (1988)
- Wakefarm is the name ECN gave the model after it was received from Madrid and adapted. (1990's)
- Fluxfarm is a (possible commercial) Energy Yield software package from ECN, with an altered Wakefarm code. (2006)
- Farmflow is ECN's wind farm design code, which incorporates the Wakefarm model. (2007)

2.3.5 Frandsen / Storpark Analytical Model

The Storpark Analytical Model (SAM) developed by Frandsen et al. [16] is a relative new approach to wake modelling. It was first published at the European Wind Energy Conference of 2006. The goal of the model was to cover small and large scale features of the flow, thus making it applicable to (infinitely) large wind farms. The model encompasses three regimes in the wake as can be seen in figure 2.5. The first regime is where multiple wake-flow is exposed to the turbines. Here the expansion of the flow and the wake deficit is described analytically. The second regime is where neighbouring rows merge, hence the

wake can only expand vertically. The third regime is where the wind farm is in balance with the boundary layer. Since some parts of the model are analytical and others are empirical engineered, the model is also referred to as the Semi-Analytical Model.

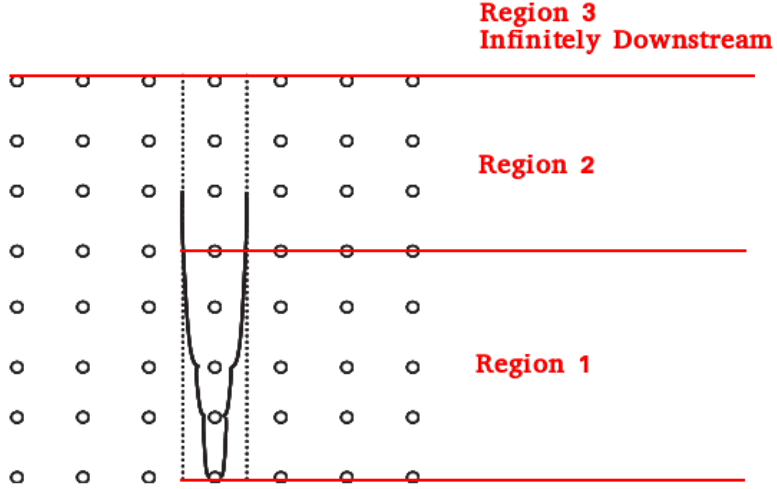


Figure 2.5: The three regions of the Frandsen Model

Region 1: Multiple Wake, Single Row

The first regime consists of two parts: The description of single turbine wake parameters and the effect of multiple turbines in row on the wake area and the velocity in the wake. As described in Frandsen et al. [16], an approach was used by applying the momentum equation to a control volume. In the near-wake, self-similarity is assumed, which as the article points out is questionable. However, since the interest of the model is in the wake of a large infinite wind farm, the assumption is justified. A simple hat is assumed to be the shape of the wake profile. The thrust can than be described by:

$$T = \frac{1}{2} \rho A_0 U_0^2 C_T \quad (2.3)$$

Here, A_0 represents the swept area of the rotor and U_0 represents the undisturbed wind speed. An approximation of this equation is used for small wake flow speed deficits: $T \approx \rho A U_0 (U_0 - U)$. This turns equation 2.3 into:

$$\frac{U}{U_0} \approx 1 - \frac{1}{2} C_T \frac{A_0}{A} \approx 1 - a \frac{A_0}{A} \quad (2.4)$$

The wake expansion is modelled with:

$$D(x) = (\beta^{\frac{k}{2}} + \alpha s)^{\frac{1}{k}} D_0 \quad (2.5)$$

Where $s = x/D_0$ and β is a function C_T only. For undefined reasons, k is set to 3. α must be determined experimentally, which makes the this part of the model partly empirical. In a later article by Rathmann et al. [45], it is stated that measurements have shown that the wake diameter far downwind tends towards zero when extrapolated back to its originating turbine. Also, a value of $\alpha = 0.7$ seemed to represent the measurements

well. A modified form of equation 2.5 was provided taking into account the measurements adjustment and a value of $k = 2$:

$$D(x) = D_0 \max(\beta, \alpha s)^{\frac{1}{2}} \quad (2.6)$$

The wind speed deficit for every n_{th} turbine in a row is estimated from equation 2.4. The wind speed in the wake is assumed constant. This results in a recursive equation:

$$c_{n+1} = 1 - \left(\frac{A_n}{A_{n+1}} (1 - c_n + \frac{1}{2} \frac{A_R}{A_{n+1}} C_T c_n) \right) \quad (2.7)$$

Here, c represents the relative wake speed deficit ($c_{n+1} = U_{n+1}/U_0$).

The wake cross-sectional area is estimated the same way as the single wake area, described in equation 2.5. Care has to be taken to exclude the area that is occupied by the ground.

Region 2: Multiple Wake, Merged

The second regime is where the wake expansion of neighbouring rows collide and the wake can only extend upwards. The height of the wake's cross-section is described by:

$$h = \frac{c_{mw}}{1 - c_{mw}} c_t (x - x_0) + h_0 \quad (2.8)$$

Where, $c_t = \frac{\pi C_T}{8s_r s_f}$, s_f is a dimensionless distance to the neighbouring rows and c_{mw} is the relative flow speed in the wake. x_0 and h_0 are integration constants to be determined from region 1.

The growth of the internal boundary layer is compared against a model from Elliott [14], as can be seen in figure 2.6. From the figure it is clear that the model does not fit well with the original Elliott model. However it is suggested that the Elliott model should be multiplied by 0.3 to fit experimental results. This is a questionable estimate, since it tends towards fiddling with data until it fits the desired curve.

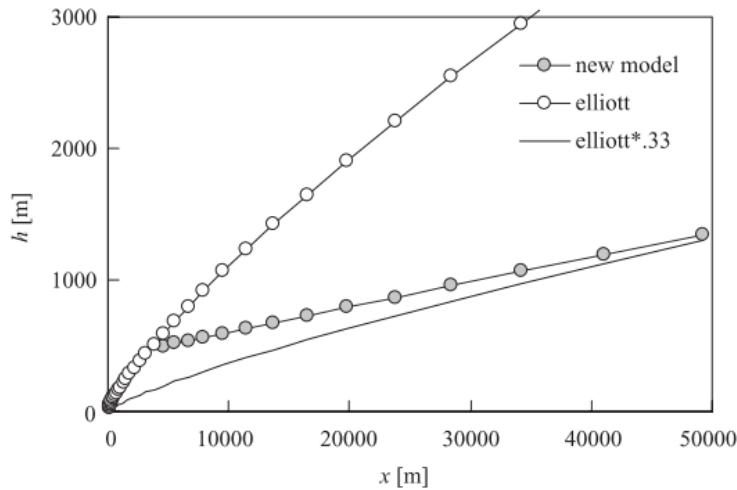


Figure 2.6: Growth of internal boundary layer as function of distance [16]

Region 3: Wind Farm in Balance with Boundary Layer

The third regime is at a far distance from the rotor, where the flow is assumed to be in equilibrium with the boundary layer. The original paper by Frandsen et al. [16] is short on this regime, since it was most likely still under development. A later paper from Rathmann et al. [46] explains the used method and compares the results with experimental data.

As can be seen in figure 2.7, a geostrophic drag-law is used:

$$G \approx \frac{\mu_*}{\kappa} \left(\ln \left(\frac{G}{f z_0} \right) - A_* \right) \quad (2.9)$$

Here, f is the latitude dependent Coriolis parameter and A_* is a modified geostrophic drag-law constant with a value of approximately 4. z_0 is the surface roughness parameter and κ the so-called Von Kármán constant. Equation 2.9 can be used in conjunction with equation 2.10 to determine the wind velocity at the desired height.

$$U(h) = \frac{G}{1 + \left(\ln \frac{G}{h f} - A_* \right) i} \quad (2.10)$$

The parameter i can be viewed as a type of turbulent intensity, dependent on the surface roughness, height and the thrust coefficient of the turbine.

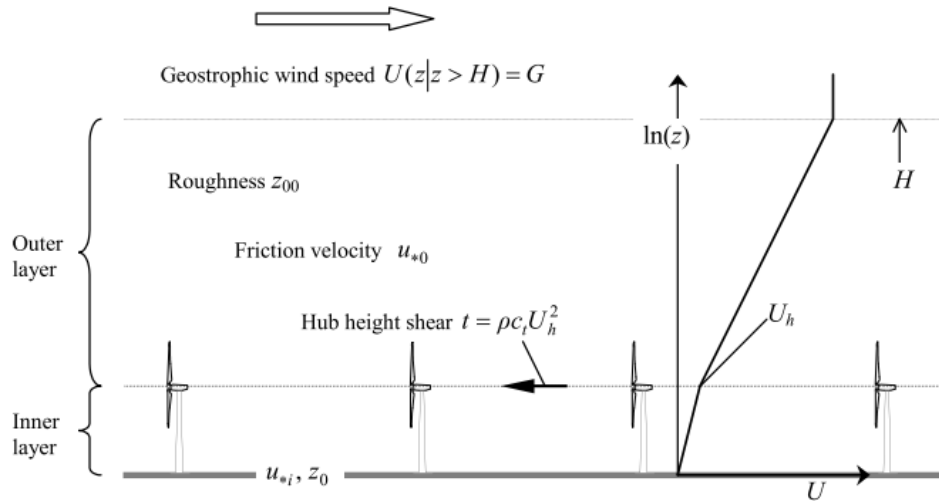


Figure 2.7: Wind profile of an infinite large wind farm. Picture from [46]

The Frandsen model was later improved by Rathmann et al. [45], to make the model compatible for numerical calculations. He used mosaic tiles in his computation method to eliminate the necessity of a perfect rectangular grid. This makes the model easier to implement in wind resource software like WAsP. It is not an interesting model in the scope of this research, since the focus is more on large wind farms. The near-wake modelling is not relevant, because it has only a small significance on the output of the model. The development of the model has unfortunately stagnated, since the lead researcher, Sten Frandsen, has passed away.

2.3.6 Atmospheric Dispersion Modelling System (ADMS)

The ADMS model was built under the TOPFARM (Next Generation Design Tool For Optimization Of Wind Farm Topology And Operation) Project. This project is funded by the EU and strives to deliver a design tool for wind farm developers [33]. This tool is focussed on the economical optimization of wind farm layouts. The basic modules of the TOPFARM project include wind farm flow field modelling, aero-elastic modelling, cost modelling and the optimization of these disciplines.

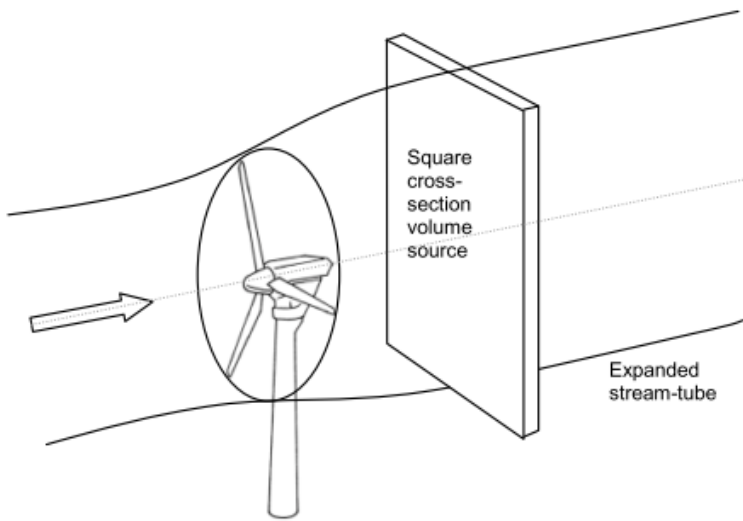


Figure 2.8: Schematic of an expanding stream-tube for use within ADMS [53]

The ADMS model is responsible for wake loss calculations. It was developed by the Cambridge Environmental Research Consultants (CERC) in 2011. The ADMS model is actually a pollution model used in the chemical industry which calculates the spread of chimney gases. This model was adapted by CERC to be able to use it in the TOPFARM project. They use a streamtube model combined with an actuator disc and Blade Element Momentum approach (figure 2.8). The model offers two options to calculate the induction factor [53]:

The first option is with the Blade Element Momentum approach. This derivation is quite straightforward and can be looked up in detail in Stidworthy et al. [53] or Manwell et al. [38]. CERC then applies two correction factors: Prandtl's tip loss factor and a correction factor for high values of a . The latter is necessary, since the actuator disc theory is only valid if $a < 0.5$. This results in:

$$a = \begin{cases} \frac{1}{K+1} & a \leq a_c \\ \frac{1}{2}[2 + K(1 - 2a_c) - \sqrt{(K(1 - 2a_c) + 2)^2 + 4(Ka_c^2 - 1)}] & a > a_c \end{cases} \quad (2.11)$$

K can be determined with:

$$K = \frac{4F \sin^2 \varphi}{\sigma C_{norm}} \quad (2.12)$$

a_c is the value for which the equation for a changes and is approximated at 0.2. F is the Prandtl's Tip Loss factor, φ is the inflow angle of the blade and σ represents the blade solidity. C_{norm} is the normal force coefficient and is determined with the inflow angle and the lift and drag coefficients of the blade.

The second option to calculate the induction factor is by using the turbine's thrust coefficient. Again, high values of a are corrected and the induction factor can be established with:

$$a = \begin{cases} \frac{1}{2}(1 - \sqrt{1 - C_T}) C_T \leq 0.64 \\ \frac{C_T - 4a_c^2}{4(1 - 2a_c)} C_T > 0.64 \end{cases} \quad (2.13)$$

Both options have their advantages. The BEM method requires a lot of geometrical parameters of the used turbine. The Thrust Coefficient option is perhaps more accurate, but the so-called C_T -curves are often classified to the turbine manufacturers. The model in general is pretty straightforward so far. It does not contain any atmospheric mixing or turbulence additions at all. The original ADMS software however, does support three contributing factors to the model.

The first is a plume meandering model. However, since it is calibrated to chimney plumes, which are of a much bigger scale compared to wind turbines, it is regrettfully regarded.

The second contribution is of entrainment of ambient air into the wake. This effect is incorporated in ADMS and can be applied to the wind turbine wake by delaying the point at which the wake starts to mix with the outer flow. This can also be done immediately, for instance in the case where the turbine is in the wake field of another wind turbine.

A third contribution of the ADMS model is shear-induced turbulence. The turbulence is estimated with empirical relations for turbines not in the wake of other turbines. For turbines inside the wake, a maximum value is assumed.

Considering the initial simplistic actuator disc approach, the model performs adequate. This can be seen in the thorough validation that came with the initial report [53]. The ADMS model is a semi-commercial model. The dispersion model is available under a commercial paid license, but was freely available for the TOPFARM project. Since CERC is a commercial research institute, it is not possible to obtain a free license.

2.4 A Note on Computational Fluid Dynamics

A recent development in wind turbine wake modelling is the use of Computational Fluid Dynamics (CFD). This is a numerical way to compute various properties (e.g. vorticity, pressure, temperature) of the flow field in the turbine wake. CFD focuses mainly on ways to solve the Navier-Stokes equation to describe the flow. There are various methods to achieve this, each with different solving schemes and discretization methods. For use with wind turbines, turbulence should be incorporated in the discretized model. The most commonly used for turbine wake modelling are the Reynolds-Averaged Navier Stokes (RANS) model and the Large Eddy Simulation (LES).

Incorporating the turbulence directly from the Navies-Stokes equations is called Direct Numerical Simulation (DNS). In DNS, the Navier Stokes equations are solved without a

turbulence model. Instead, the N-S equations themselves are used to calculate the whole range of spatial and temporal turbulence. This requires a great amount of computational power, which increases with Re^3 . A recent example for the use of DNS was carried out by the University of Texas on a supercomputer by IBM, which consists of 786.000 processing cores [35]. Thus, this method is unsuitable for wind turbine wake modelling.

2.4.1 Reynolds-Averaged Navier Stokes

According to the work of Sanderse [48], RANS methods are still quite complicated to solve due to the elliptic nature of the pressure Poisson equation. Three methods are used for this, to which RANS codes can be categorized. The simplified parabolization, linearization and full original elliptic modelling approach.

Compared to parabolic methods, linearized models are significant faster. This is due to the linearisation of the Navier-Stokes equations, lookup tables for velocity profiles and a spectral method in which the governing equations are Fourier transformed. The model is less accurate compared to the parabolic methods, but shows decent results in the far wake with short computation time.

2.4.2 Large Eddy Simulation

Large Eddy Simulations (LES) serve as an alternative towards the RANS methods. In LES the small scale eddies are filtered out which reduces the computation time. This results in a simulation that is more accurate in terms of wake turbulence modelling compared to RANS, with an increased computation time from hours to days [48]. However, the extra computation time is negligible when compared to DNS. Troldborg et al. [55] has showed that LES, combined with an actuator line technique shows a detailed and accurate image of the near- and far-wake field.

In general, CFD models provide high accuracy of the wake, but require enormous computation power compared to engineering models. It is therefore mainly used in complex terrain and serves as a research tool rather than a design tool. However, with the current trend of microprocessing power and the increasing optimization of the algorithms of modelling code, one could conclude that it is a matter of time before CFD models are used as a design tool for optimizing wind farm layouts. Currently, this is not the case.

2.5 Conclusions from the Literature Study

The analysis on far-wake models have resulted in the conclusion that the near-wake is often a simplistic representation compared to the methodology used in the far-wake. It seems that the attention of wake model development has shifted greatly towards far-wake phenomena, e.g. wake added turbulence and wake interaction. This has lead to the hypothesis, that an increase in near-wake prediction accuracy, could lead to an increase in far-wake prediction accuracy.

The best way to test this hypothesis is to simulate the near-wake with a more extended model and implement this in a far-wake model. The Vortex Ring Model seems to be

the best candidate for various reasons. It is a simple, yet physics based model, which does not require empirical data, keeping the model completely analytical. It was also already proven by Baldacchino [4] that the model is capable of simulating the near-wake with favourable results. Experience with the model at the Delft University of Technology where this research is carried out, is also a beneficial factor.

The Jensen and Larsen far-wake models are chosen as candidates for coupling with the VRM. The Jensen model is chosen for its simplicity as a first case and proof of concept. The Larsen model is a modular model with an easy to replace near-wake simulation which makes it a good second candidate. The model is regularly improved and updated with new calibration methods and the model is widely accepted in the wind industry and regarded as a “bankable” wake model.

The concept of combining different models is irregular, but not unheard of in the field. Turbine wake added turbulence models are regularly interchanged or combined with non-wake added turbulence models like the Jensen or Ainslie models. This has even led to software packages where wake models and turbulence models can be freely combined (see Appendix B.2). Larsen experimented with different near-wake models and an interesting point is the recommendation from Larsen et al. [32], where he states that “*... there is an obvious potential for the two approaches (vorticity formulation and boundary layer equation resp.) to complement each other by computing the near field wake behaviour with the vorticity model, and subsequently use the resulting near field wake deficit as input to the 2D boundary layer model for simulation of the far field wake behaviour.*” This has a high similarity with the approach in this thesis, which gives a hopeful prospect to a good result.

Chapter 3

The Vortex Ring Model

The near-wake of the proposed model is simulated with the use of perfect inviscid vortex rings. The resulting series of rings can be used to analytically describe the resulting velocity field. The methodology of a vortex ring describing a velocity field is elaborated in section 3.1 in detail. Section 3.2 describes how multiple vortex rings are shed from a uniformly loaded actuator disc into a uniform velocity field, to simulate the wake of a wind turbine. Progression of the wake in a numerical implementation is discussed in sections 3.3 and 3.4 respectively, where the translation and expansion of the vortex rings is discussed. Section 3.5 closes this chapter with some final remarks on the numerical implementation.

3.1 Analytical Expression of the Velocity Field

A vortex ring or series of vortex rings can be used to calculate an axi-symmetric 3D velocity field. Yoon and Heister [60] used the Biot-Savart law to derive a set of equations describing the field. The derivation is too extensive to elaborate here and the reader is advised to consult [60] if interested. The notation introduced by Micallef et al. [41] is used in this thesis. If a vortex ring at position $(0, 0, z_i)$ is considered as displayed in figure 3.1, then the axial (u_z) an radial (u_r) velocities at an arbitrary point $P(r, \theta, z)$ can be described with equations 3.1 and 3.2. These set of equations are valid on every point in the field, except on the vortex ring itself (where $R_i = r$ and $z = z_i$), which results in a singularity.

$$u_z = \frac{\Gamma_i}{2\pi\sqrt{[(z - z_i)^2 + (r + R_i)^2]}} \cdot \left[K(m) + \frac{R_i^2 - r^2 - (z - z_i)^2}{(z - z_i)^2 + (R_i - r)^2} E(m) \right] \quad (3.1)$$

$$u_r = \frac{\Gamma_i(z - z_i)}{2\pi r\sqrt{[(z - z_i)^2 + (r + R_i)^2]}} \cdot \left[K(m) - \frac{R_i^2 + r^2 + (z - z_i)^2}{(z - z_i)^2 + (R_i - r)^2} E(m) \right] \quad (3.2)$$

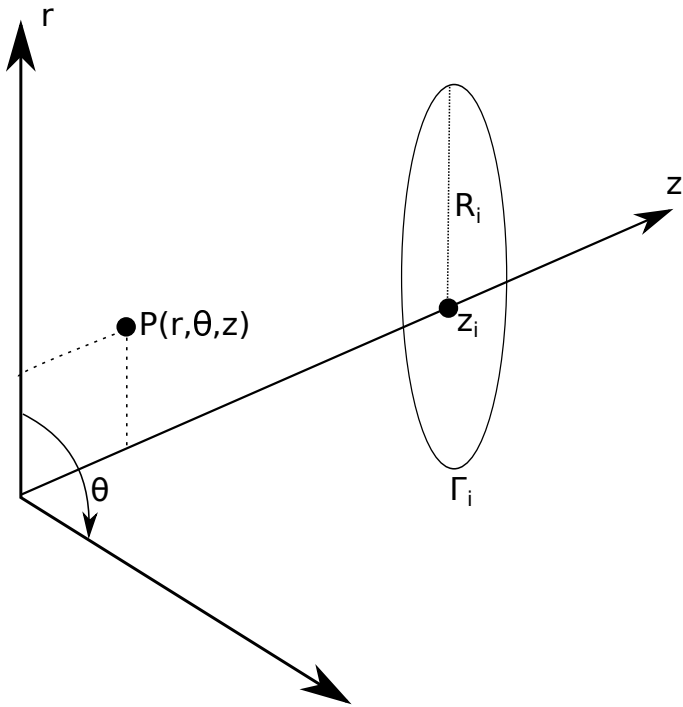


Figure 3.1: Coordinate system used with a vortex ring and an arbitrary point in space

In these equations, $K(m)$ and $E(m)$ represent complete elliptic integrals of the first (K) and second (E) kind, where m is determined with equation 3.3.

$$m = \frac{4rR_i}{(z - z_i)^2 + (r + R_i)^2} \quad (3.3)$$

The elliptic integrals used are described by Abramowitz et al. [1] and are displayed in equation 3.4 and 3.5.

$$K(m) = \int_0^1 \frac{1}{\sqrt{(1-t^2)(1-mt^2)}} dt \quad (3.4)$$

$$E(m) = \int_0^1 \frac{\sqrt{1-mt^2}}{\sqrt{1-t^2}} dt \quad (3.5)$$

With the use of equations 3.1 and 3.2, the induced velocities at any point in the field can be calculated. The resulting axi-symmetric velocity field can be visualised in 2D. An example of the resulting induced velocity field of a single vortex ring of unit strength is shown in figure 3.2. The highest induced velocities are concentrated around the edge of the ring, where the vorticity is concentrated.

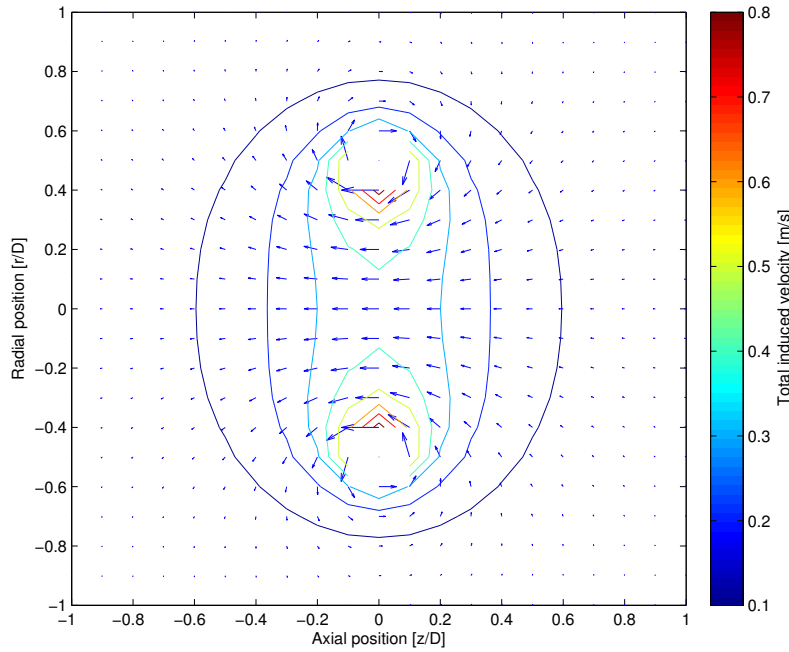


Figure 3.2: Velocity field induced by a perfect inviscid vortex ring of unit strength and radius visualized by coloured contours representing total velocities and quivers visualizing strength and direction

3.2 Vortex Ring Strength and Rotor Shedding

In order to model the near-wake field of a wind turbine with the use of vortex rings, the strength of these rings need to be derived. The turbine rotor in the model is replaced by a uniformly loaded actuator disc, which sheds discrete vortex rings in the free-stream as displayed in figure 3.3. Using the Euler format of the momentum and continuity equations in an incompressible and inviscid flow, van Kuik [56] derived a relation between the shedding of vorticity from the disc and the pressure jump at the edge of the actuator.

$$\frac{\partial \Gamma_{edge}}{\partial t} = \frac{\Delta p}{\rho} \quad (3.6)$$

Following the approach by Yu et al. [61], equation 3.6 is used to determine the strength of discrete vortex rings shed by the actuator disc. Rewriting equation 3.6 for a series of discrete vortex rings with strength Γ_i results in:

$$\Gamma_i = \frac{\Delta p \Delta t}{\rho} \quad (3.7)$$

The pressure difference Δp across the disc can be determined by dividing the total thrust

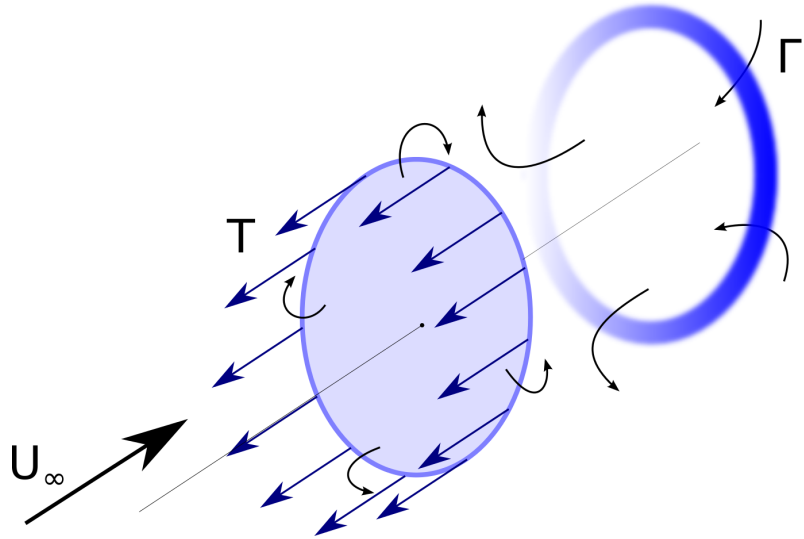


Figure 3.3: Schematic illustration of an actuator disc shedding a vortex ring

acting on the actuator by the area of the disc:

$$\Delta p = \frac{T}{A} \quad (3.8)$$

The thrust T can be written with the definition of the thrust coefficient C_T . Substituting this in equation 3.8 gives:

$$\Delta p = \frac{\frac{1}{2}\rho C_T U_\infty^2 A}{A} = \frac{1}{2}\rho C_T U_\infty^2 \quad (3.9)$$

Substituting equation 3.9 into equation 3.7 gives the final expression for the vortex ring strength Γ in equation 3.10.

$$\Gamma_i = \frac{1}{2}U_\infty^2 C_T \Delta t \quad (3.10)$$

Here, U_∞ is the undisturbed wind speed and C_T is the thrust coefficient of the rotor. Δt represents the period between the shedding of two vortex rings. If a relatively small value for Δt is taken, the wake of the turbine is described by a large number of vortex rings in the wake, which behaves more as a cylindrical sheet of vorticity, rather than distinct sources of vorticity. Two approaches for Δt are used. In the first approach, Δt is linked to the revolution of a blade in an approach to simulate a realistic tip vortex pitch with the use of equation 3.11. Here, ω represents the rotational speed of the rotor and N the number of blades. This approach is used in conjunction with a constrained ring radii by following a wake expansion model as discussed in section 3.4.

$$\Delta t = \frac{2\pi}{\omega N} \quad (3.11)$$

The second approach follows a free-wake expansion model. It was found that the period Δt , determined from equation 3.11 resulted in strong vortex interaction, which was found unstable. Therefore, in the free-wake expansion approach, a much smaller Δt is used which still includes vortex interaction, but guarantees the stability of the simulation.

3.3 Vortex Ring Translational Velocity

The position of a vortex ring in the free wake, is determined from the axial velocity of the ring. An initial uniform velocity field is assumed. The translational velocity is then derived by superimposing the undisturbed wind speed, the self-induced velocity and the mutually induced velocity from other vortex rings.

3.3.1 Self-Induced Velocity

The self-induced velocity of a vortex ring is usually determined with the well-known Kelvin formula as derived by Fraenkel [15] and displayed in equation 3.12.

$$u_s = \frac{\Gamma}{4\pi R} \left[\ln\left(\frac{8R}{r_c}\right) - \frac{1}{4} \right] \quad (3.12)$$

Here, the variable r_c represents the core size of the vortex ring. Baldacchino [4] derived a simpler equation which approaches the Kelvin formula, but is independent of the vortex ring's core size r_c . The self-induced velocity is derived by evaluating the induced velocity at the centre of the vortex ring. Since the rings are assumed perfectly circular, the radial velocity at the centre of the ring is zero. The axial velocity at the centre determines the self-induced velocity and can easily be evaluated with equation 3.1. At the centre of the ring, $z = z_i$ and $r = 0$ and equation 3.1 reduces to:

$$u_z = \frac{\Gamma_i}{2\pi\sqrt{[(0)^2 + (0 + R_i)^2]}} \cdot \left[K(m) + \frac{R_i^2 - 0^2 - (0)^2}{(0^2 + (R_i - 0)^2)} E(m) \right] = \frac{\Gamma_i}{2\pi R_i} \cdot [K(m) + E(m)] \quad (3.13)$$

Since $m = 0$, $K(m)$ and $E(m)$ both reduce to $\pi/2$. This gives the final solution for the self-induced velocity of a single perfectly circular and infinitely thin vortex ring as:

$$u_s = \frac{\Gamma}{2R} \quad (3.14)$$

Figure 3.4 shows a comparison as performed by Baldacchino [4] of the analytical expression and the Kelvin formula. It is clear that difference becomes negligible if a infinitely thin vortex core is assumed.

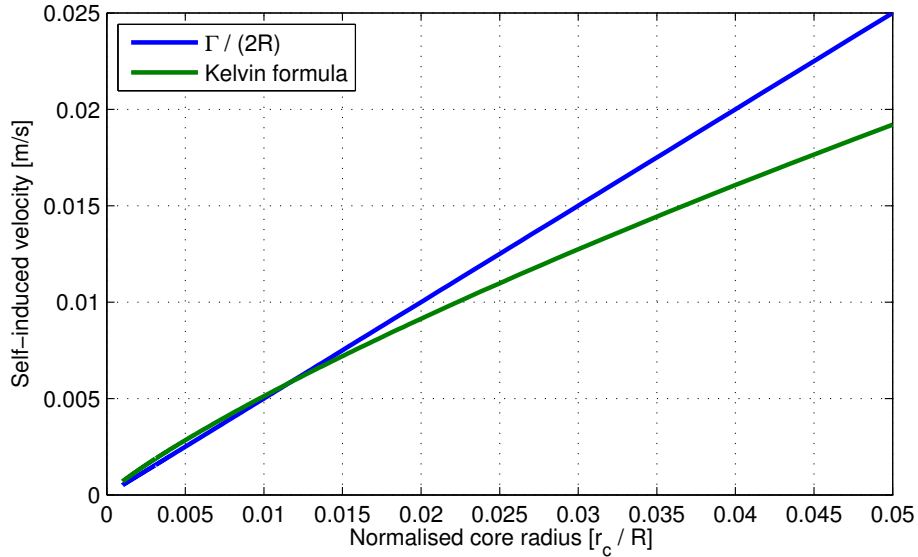


Figure 3.4: Comparison by Baldacchino [4] of the self-induced velocity as determined with the Kelvin formula and the analytical formulation

3.3.2 Mutually-Induced Velocity

In a series of vortex rings, induced velocities act on other rings as well, which adds a translational velocity to those rings in a certain direction. This mutually induced velocity of a vortex ring is determined by the total induced axial velocity on an arbitrary point on the vortex ring by all other rings in the series.

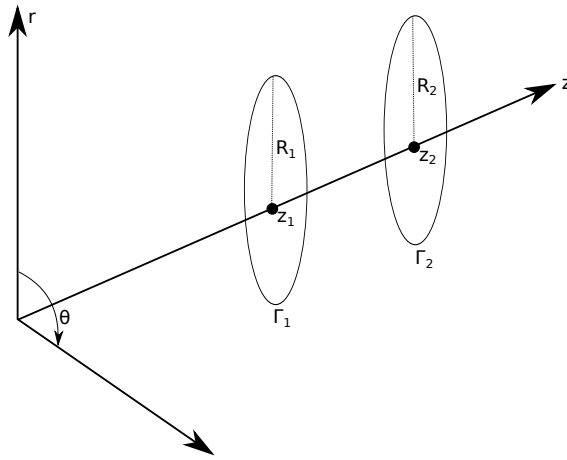


Figure 3.5: Schematic overview of mutually induced velocities from a pair of vortex rings

Consider the pair of vortex rings as schematically displayed in figure 3.5. Since the vortex rings are considered as perfect circular rings, the translational velocity of vortex ring 2, induced by vortex ring 1, can be described by calculating the induced velocities at an arbitrary point on the ring of vortex ring 2. The induced velocity in axial direction is exactly the same across the ring as long as the rings remain co-axial. The induced velocity

in axial direction of vortex ring 1 on vortex ring 2 becomes:

$$u_{m,1} = \frac{\Gamma_1}{2\pi\sqrt{[(z_2 - z_1)^2 + (R_2 + R_1)^2]}} \cdot \left[K(m) + \frac{R_1^2 - R_2^2 - (z_2 - z_1)^2}{(z_2 - z_1)^2 + (R_1 - R_2)^2} E(m) \right] \quad (3.15)$$

This is done for every other vortex ring in the wake field. The total mutual induced velocity is the sum of all individual contributions and is described in equation 3.16.

$$u_m = \sum_{i=1}^n u_{m,i} \quad (3.16)$$

In the numerical implementation of the model, the total translational velocity can be computed by the superposition of the undisturbed wind speed (U_∞), the self-induced velocity (3.14) and the sum of mutually induced velocities (3.16) at a single timestep as described in equation 3.17. The principle of superposition holds only for calculations done within a single time frame, thus stepping away from an analytical towards a numerical wake simulation.

$$u_i = U_\infty + u_s + u_m = U_\infty + \frac{\Gamma_i}{2R_i} + \sum_{j=1}^n u_{m,j} \quad (3.17)$$

In the numerical model, the axial position of the vortex ring is determined by using the translational velocity in a second order update scheme as described in equation 3.18.

$$z_i^t = z_i^{(t-1)} + u_i^t \Delta t + \frac{1}{2} \frac{u_i^t - u_i^{(t-1)}}{\Delta t} \Delta t^2 \quad (3.18)$$

3.4 Wake Expansion Model

Two different expansion models have been implemented in the model. First, a constrained model is discussed in section 3.4.1, where the ring radius is computed from axial induced velocities at the rotor. Secondly, a free-wake model, where the ring radius is determined by the induced radial velocities from other rings is discussed in section 3.4.2. A comparison of both models with wind tunnel data is presented in Chapter 4.

3.4.1 Constrained Wake Expansion

A constrained expansion of the wake was derived by Wilson [59] from the actuator disc theory. Wilson derived a relation between wake expansion, axial induction at the disc and the location in the wake, which resulted in equation 3.19:

$$R_{wake} = R \frac{1}{\sqrt{1 - \frac{E\xi}{\sqrt{1+\xi^2}}}} \quad (3.19)$$

Where R is the original rotor radius, ξ is the non-dimensionalised position in the wake (z/R) and E is related to the average axial induction factor a with:

$$E = \frac{a}{1-a} \quad (3.20)$$

The average axial induction factor a can be derived from the relation with thrust coefficient from the actuator disc theory:

$$C_T = 4a(1-a) \quad (3.21)$$

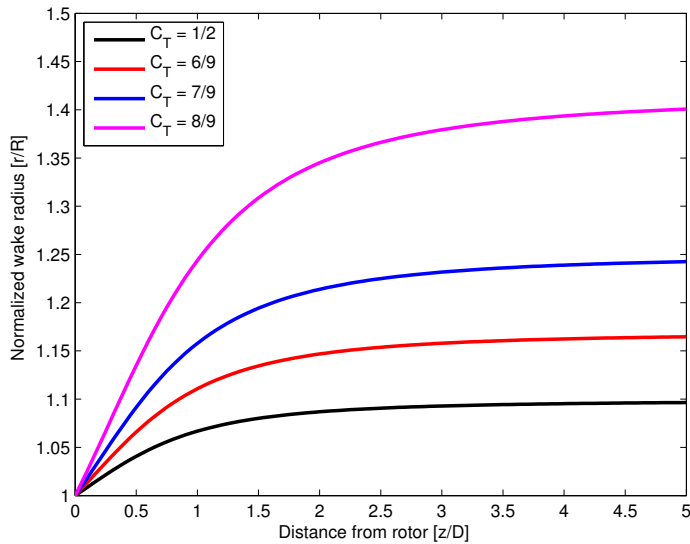


Figure 3.6: Wilson wake expansion for various values of C_T

Figure 3.6 shows the expansion along the wake for various values of C_T . The advantage of the constrained method is that an approach of a tip vortex pitch is feasible by determining the timestep with equation 3.11. The disadvantage of the model is that constrained vortex interaction is physically incorrect. However, the numerical implementation is much more stable, resulting in a faster convergence of the wake velocities which is in favour of computational time.

3.4.2 Wake Expansion by Vortex Interaction

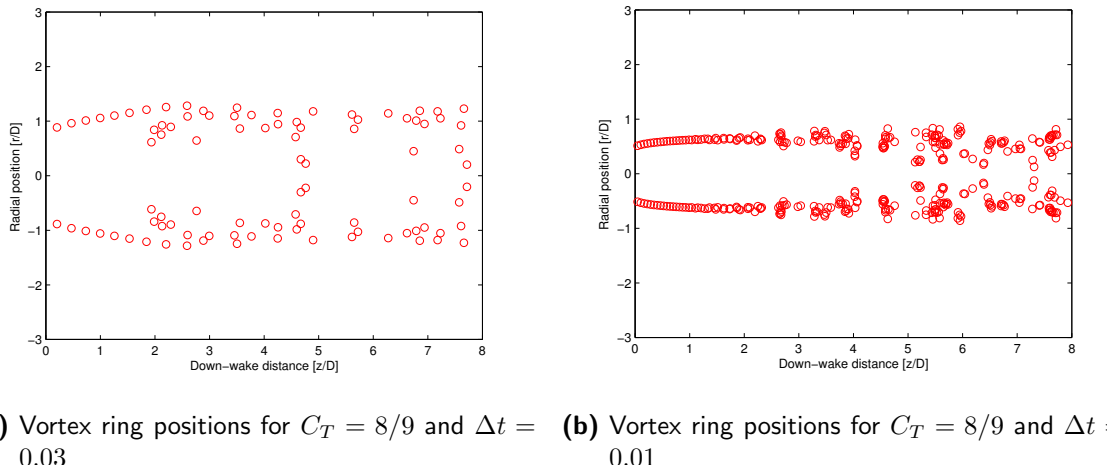
A second method to simulate wake expansion is to incorporate the induced velocities to radial growth. This is achieved by choosing a single point on the radius of a ring and determine the induced radial velocities from the series of rings on that point. It is then assumed that the rate of ring radius expansion or contraction is proportional to the induced radial velocity at the arbitrary point on the ring.

This approach is similar to the determination of the mutually induced translational velocity of the ring as discussed in section 3.3.2. A second order update scheme is used in

the simulation, so the radius of an arbitrary ring in the free wake is determined with:

$$R^t = R^{(t-1)} + \left[\sum_{i=1}^n u_{r,i} \right]^t \Delta t + \frac{1}{2} \frac{\left[\sum_{i=1}^n u_{r,i} \right]^t - \left[\sum_{i=1}^n u_{r,i} \right]^{(t-1)}}{\Delta t} \Delta t^2 \quad (3.22)$$

Here, n refers to the total number of rings in the wake and $u_{r,i}$ presents the induced radial velocity on the arbitrary ring by ring i . The superscripts t and $t - 1$ denote the current time and previous timestep in the simulation. The timestep Δt is a crucial factor for the stability of the model in this approach and a smaller value than was considered in equation 3.11 is required.



(a) Vortex ring positions for $C_T = 8/9$ and $\Delta t = 0.03$ (b) Vortex ring positions for $C_T = 8/9$ and $\Delta t = 0.01$

Figure 3.7: Position of the vortex rings along the wake for a large (left) and small timestep (right) visualized by small circles

The effect of the timestep is displayed in figure 3.7. A large timestep leads to stronger vortex rings, which are more sparsely spaced. Another phenomenon observed is that as the rings contract, the self induced velocity increases (see equation 3.14) and the rings start to travel upstream. Figure 3.7b shows the same simulation with a much smaller timestep. Vortex ring pairing is observed around $2D$, which evolve into larger groups after $2D$. After $5D$, strong interaction is observed. A possible physical explanation is that this position coincides with the point where the stable wake starts to break down. It is also possible that time-stepping is too large for this region and numerical errors are introduced in the simulation. Either way, at this point the flow can no longer be considered inviscid and the model becomes invalid. However, the model is only used to simulate wake velocities in the near-wake ($< 2D$), where the wake is considered stable. With the smaller timestep, the model is numerically stable and the phenomenon of upstream travelling vortex rings is no longer observed. The timestep should be chosen such that the near-wake is stable and computation time is still manageable.

Figure 3.8 shows a comparison of the constrained expansion method and the free-wake expansion method with various values for the thrust coefficient. Relative to the free-wake expansion model, the Wilson model seems to underpredict the expansion immediate after the rotor and overpredict the expansion further down-stream. For most values of C_T , the

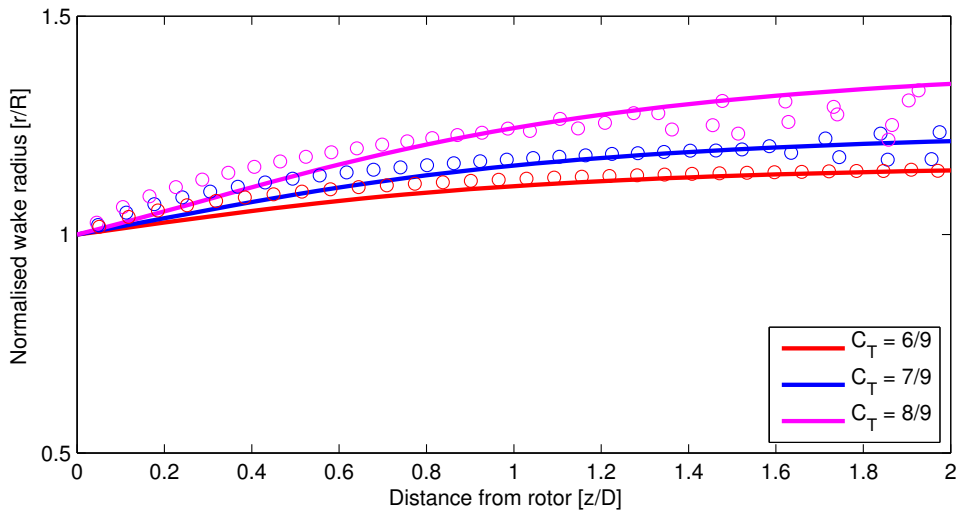


Figure 3.8: Comparison of the Wilson wake expansion method and the free wake induced expansion visualised by constant sized circles

difference is small. For higher C_T values, the Wilson method seems to have a slightly bigger expansion at the end with respect to the free-wake expansion model. A physical explanation might be that the Wilson model predicts the edge of the wake boundary and the vortex rings are located inside the wake shear layer.

3.5 Discussion on the Numerical Implementation of the VRM

The numerical implementation of the VRM has resulted in two versions. First, a constrained expansion model, where the period between vortex ring shedding is pitched to the rotational frequency of the rotor, simulating blade tip vortices. Second, a free-wake model where the vortex rings are free to interact and expand/contract. From a numerical standpoint, the constrained model is favoured, since the larger timestep allows for a fast simulation of the near-wake. Both models are compared against wind tunnel measurements in the next chapter, to gain more insight in which method is more accurate.

Chapter 4

Verification and Validation of the Vortex Ring Model

This chapter presents results from a verification and validation study of the near-wake vortex ring model. A verification study is performed by calculating the induced velocity at the rotor from the model and compare those with an analytical solution. This is shown in section 4.1, together with a sensitivity study to the relation of the central wake velocities and the length of the simulated vortex ring wake with the Wilson wake expansion model. Section 4.2 shows the result of a validation study with the use of wind tunnel measurements from a small-scale wind turbine model and a porous mesh which represents an actuator disc. Finally, section 4.3 discusses why the induced expansion method is used for coupling with the Jensen and Larsen far-wake models.

4.1 Verification of the Near-Wake VRM

The theory and physical attributes of the near-wake vortex model have been discussed in Chapter 3. These fundamental equations are implemented in a numerical computer program to simulate the wake. To verify that the numerical results are according to theory, an investigation was designed, to compare the resulting induced velocities of the model with analytical results. In the following simulations the parameters of the wind tunnel validation case are used, but the results are non-dimensionalised accordingly.

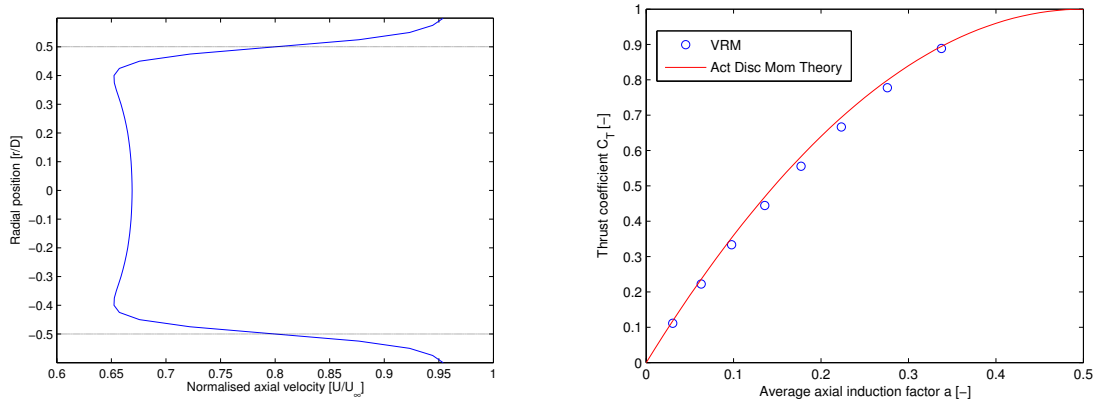
4.1.1 Verification with the Axial Induced Velocity

The induced velocities from the vortex rings in the near wake, can be used to determine the velocities at the position of the rotor. In this study, the constrained wake expansion is used, but the free-wake model results in similar results. An example of the velocity profile at the actuator can be seen in figure 4.1a, where the thrust coefficient was set to $C_T = 8/9$. The figure shows that the velocity at the actuator fluctuates between roughly

0.65 and 0.67. This is correct, since the velocity at the actuator from the actuator disk momentum theory would result in 0.67. The relation between the axial induction factor a and the thrust coefficient C_T from actuator disc theory is displayed in equation 4.1.

$$-4a^2 + 4a = C_T \quad (4.1)$$

This quadratic relation can easily be analytically solved, where solutions higher than 0.5 are disregarded as non-physical according to the actuator disc theory. The *average* induction at the actuator in the numerical VRM is calculated by averaging the *local* induced velocities from $r = -0.5D$ to $r = +0.5D$ at $z = 0$. This way the induction at the disc from the numerical vortex ring model can be compared with the analytical solutions from the actuator disc theory.



(a) Velocities at the actuator disc loaded with $C_T = 8/9$ at $z = 0$ from the undisturbed wind speed and the induction of the vortex rings

(b) Averaged induced axial velocity from the vortex ring model for various values of C_T compared with the actuator disc momentum theory

Figure 4.1: Results from a verification study where the induced velocities at the position of the actuator disc are studied

Figure 4.1b shows the result of this procedure for various values of C_T . The numerical simulations seem to stay close to the analytical results and only a small deviation is observed. From this it can be concluded, that the simulation of vortex ring strength and translation, as well as the determination of the induced flow field is correctly implemented.

4.1.2 Wake Length Sensitivity Study for the Constrained Wilson Expansion

The Wilson expansion model implies that the vortex ring radius is constrained. This prevents vortex ring interaction. In longer simulations, the wake extends indefinitely and the centreline velocity seem to converge to a certain value. An effect was observed, that a longer (time domain) simulation resulted in a longer (space domain) wake and in lower centreline velocities in the near-wake region. This is investigated to determine if a stable convergence is ultimately achieved.

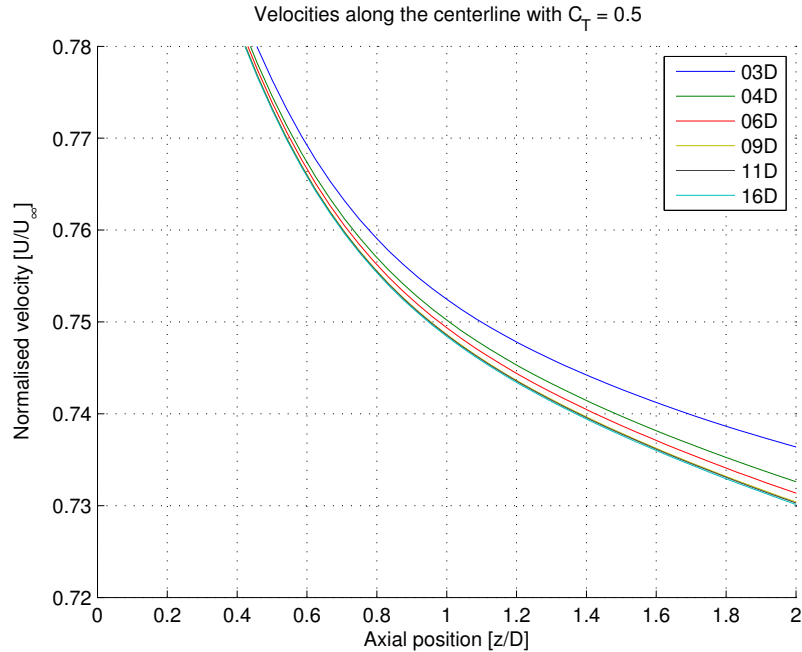


Figure 4.2: Graph showing the influence of simulated wake length on the velocities on the centreline for $C_T = 1/2$

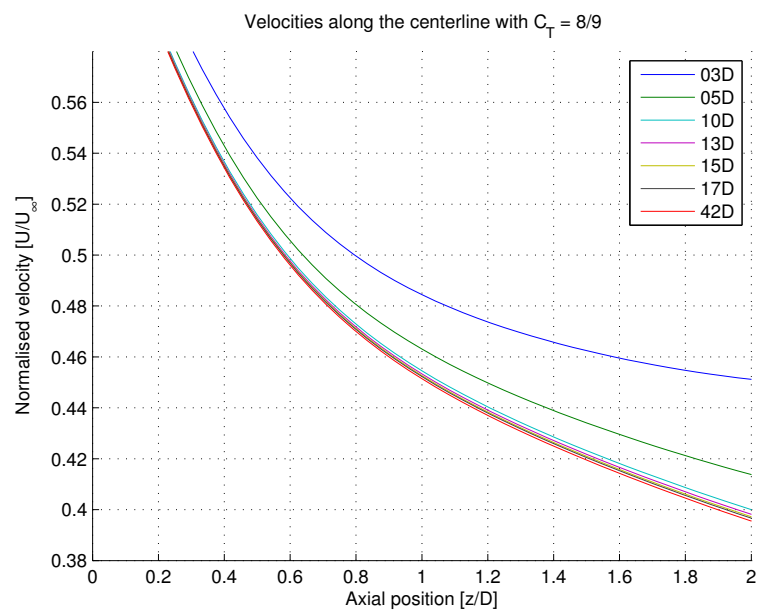


Figure 4.3: Graph showing the influence of simulated wake length on the velocities on the centreline for $C_T = 8/9$

Figure 4.2 and 4.3 show the effect of wake length on centreline velocity for fixed values of C_T . The wake is shown in the near-wake region ($0 - 2D$), since this is where the velocities are of interest. Outside the near-wake are, the far-wake model will predict the wake velocities. From these figures it can be concluded that the solution converges to a definite value. With the Wilson constrained expansion method, a simulated wake length of $10D$ is sufficient for a converging solution in the near-wake with high thrust coefficients.

4.1.3 Vortex Ring Interaction

The effect of wake length on the centreline velocities previously discussed in section 4.1.2 does not apply to the wake expansion due to vortex interaction. In this case, the rings contract in the far wake and the centreline velocities start to fluctuate. The amount of interaction is dependent on thrust coefficient and simulation time. If the simulation is run for a relatively long time period, interaction becomes dominant and the wake breaks down.

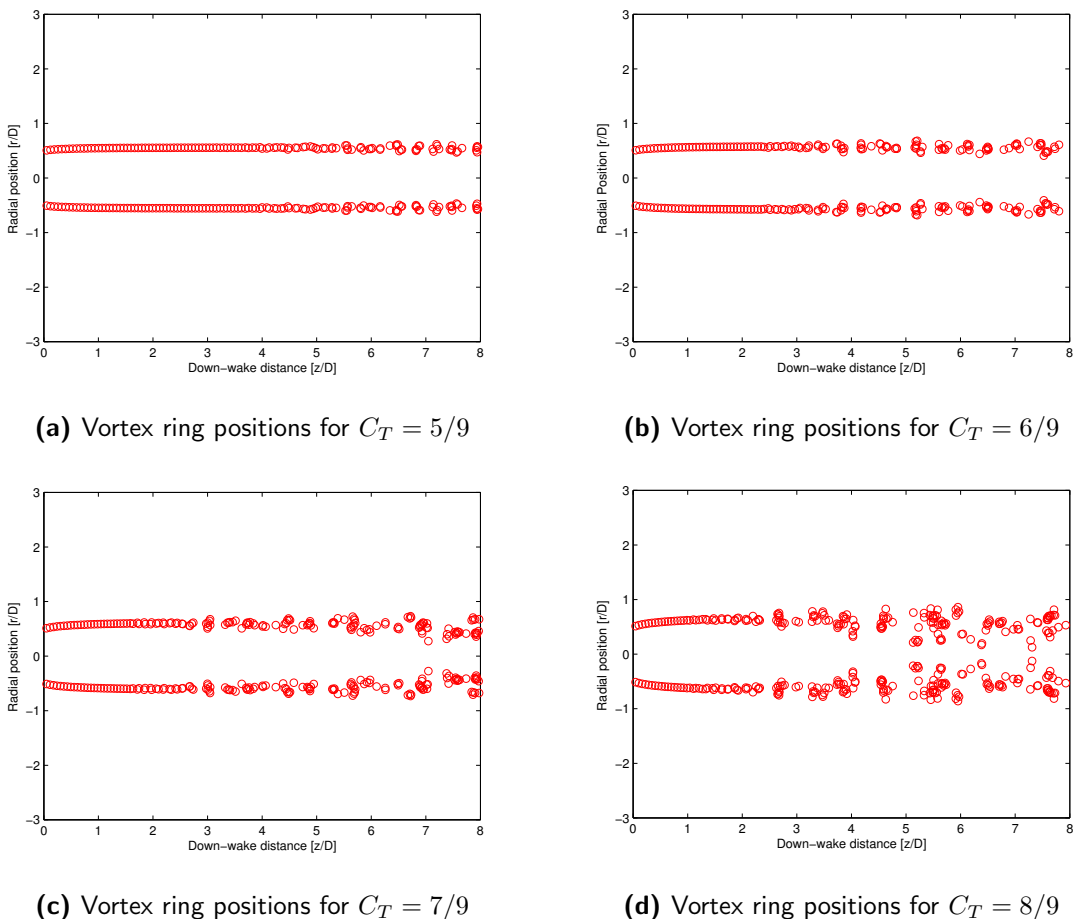


Figure 4.4: Position of vortex rings plotted showing the vortex ring interaction. Lower C_T values result in a more stable wake, with interaction starting at a further distance compared to higher values for C_T .

Figure 4.4 shows the vortex rings for various values of the thrust coefficient after a fixed period of time. The development of wake interaction due to higher thrust values is clear and heavy interaction is observed in figure 4.4d after $4D$. After this point, the wake can no longer be regarded as inviscid and the validity of the model should be doubted from this position in the wake.

4.2 Validation with Wind Tunnel Measurements

The derived Vortex Ring Model is compared against experimental wind tunnel data. For this, data from a wind tunnel experiment by Lignarolo et al. [36] is used. The research goal of the experiment was to compare the wake field of the theoretical actuator disc to a bladed rotor. To achieve this, a two-bladed horizontal axis wind turbine was used at an optimal thrust ratio of $\lambda = 6$ and a rotor diameter of $0.6m$. The actuator was represented by an equally sized circular mesh with a porosity of 32%, which resulted in an equal thrust coefficient of $C_T = 0.93$. Both the wind turbine and the actuator were placed at a similar position in the TU Delft Open Jet Facility (OJF) wind tunnel which created a uniform velocity of $U_\infty = 4.7m/s$ with approximately 0.5% turbulence. More details on the experiment are displayed in table 4.1. The velocity field was measured with a stereoscopic PIV setup on a traversing system to capture a 2D sheet of the wakefield.

Table 4.1: Parameters of the Wind Tunnel Experiment. Values extracted from Lignarolo et al. [36]

Parameter		Wind Turbine	Actuator
Diameter	D	0.6 m	0.6 m
Free-stream velocity	U_∞	4.7 m/s	4.7 m/s
Rotational frequency	ω	109.3 rad/s	-
Reynolds number (root)	Re_{cr}	32,000	-
Reynolds number (tip)	Re_{ct}	96,000	-
Reynolds number (diameter)	Re_D	188,000	188,000
Thrust coefficient	C_T	0.93	0.93
Tip speed ratio	λ	6.97	-
Turbulence Intensity	TI	0.5%	0.5%

The experiment is simulated with the VRM and compared to the measurement data. All parameters from the experiments were put in the model, except the turbulence, since the VRM is limited to laminar inflow. The wake expansion model was kept variable to compare the constrained Wilson wake expansion and the induced free-wake expansion to the results from the experiment.

Figure 4.5 and 4.6 show velocity profiles at various distances down-wake of the rotor disc. Each graph shows the actuator and rotor measurements from the wind tunnel and the simulation results, in which a distinction is made between time-averaged (TA) and instantaneous (I) results. The time-averaged results show velocities averaged over two time periods $2\Delta t$, with a sample rate of 500 samples per period. This is done to verify if the instantaneous velocity field is representative for a time independent period. A condition is set to disregard a ring when it is within $0.02D$ of the axial position where induced

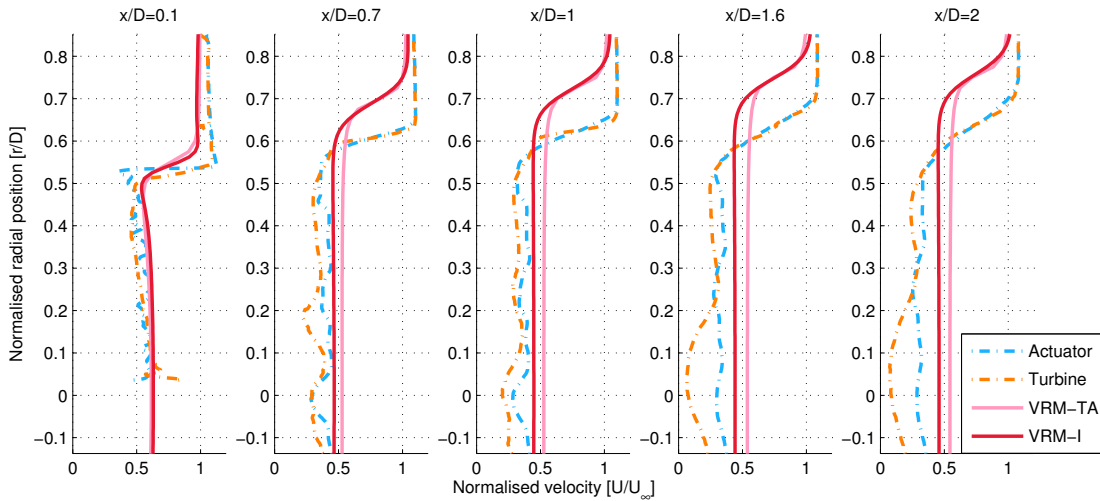


Figure 4.5: Comparison of the near-wake VRM (**Wilson constrained expansion method**) with wind tunnel measurements showing velocity profiles of the porous disc, two-bladed turbine, time-averaged VRM and instantaneous VRM

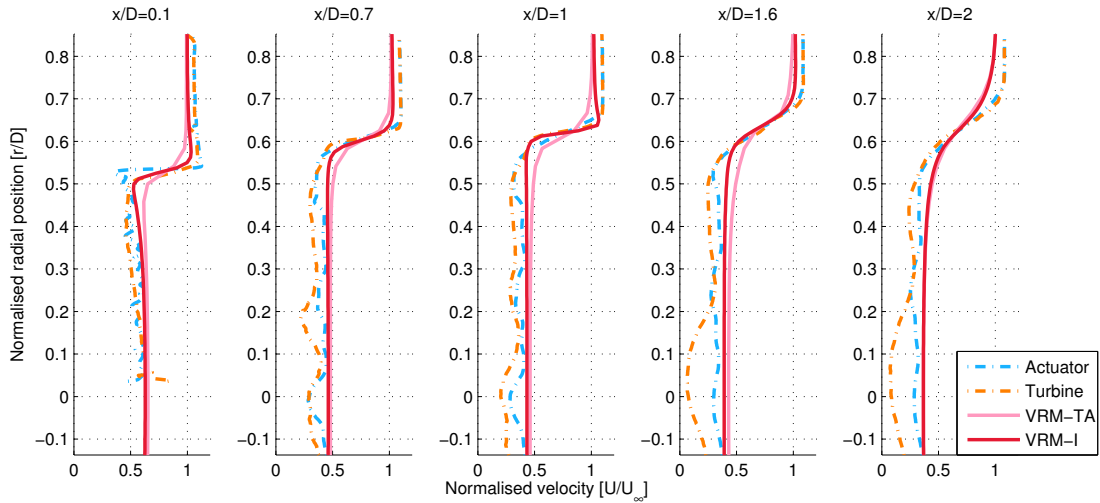


Figure 4.6: Comparison of the near-wake VRM (**Induced free-wake expansion method**) with wind tunnel measurements showing velocity profiles of the porous disc, two-bladed turbine, time-averaged VRM and instantaneous VRM

velocities are determined to avoid the ring singularities. The instantaneous results were taken at the end of the simulation, where the vortex rings have reached a minimum distance of $20D$ and the exact axial position was taken between the closest two vortex rings.

From the figures can be concluded, that the wake expansion derived from the induced wake expansion model (figure 4.6) is more in agreement with the wind tunnel data as compared to the constrained Wilson wake expansion (figure 4.5), which overpredicts the expansion of the wake. The results of the instantaneous velocity field in figure 4.5, provides a more accurate description of the wake shear layer, as compared to the time-averaged results.

With the induced wake expansion method (figure 4.6), the results of the instantaneous velocity field is in accordance with the time-averaged values. The instantaneous velocity field simulation has a much shorter computational period which is a significant advantage over the time-averaged method. The Wilson expansion method (figure 4.5) shows a difference in velocity deficit on almost all axial positions between the time-averaged and the instantaneous results. This is most likely due to the set condition to disregard rings close to the axial position where the induced velocities are calculated during the time-averaged simulation. This effect is more visible in the Wilson expansion method, due to the stronger vortex rings.

Theoretically, the VRM should show a closer relation to the actuator disc when compared to the rotor, since the vortex rings are shed from an actuator disc and wake rotation is not modelled in the VRM, which is indeed observed.

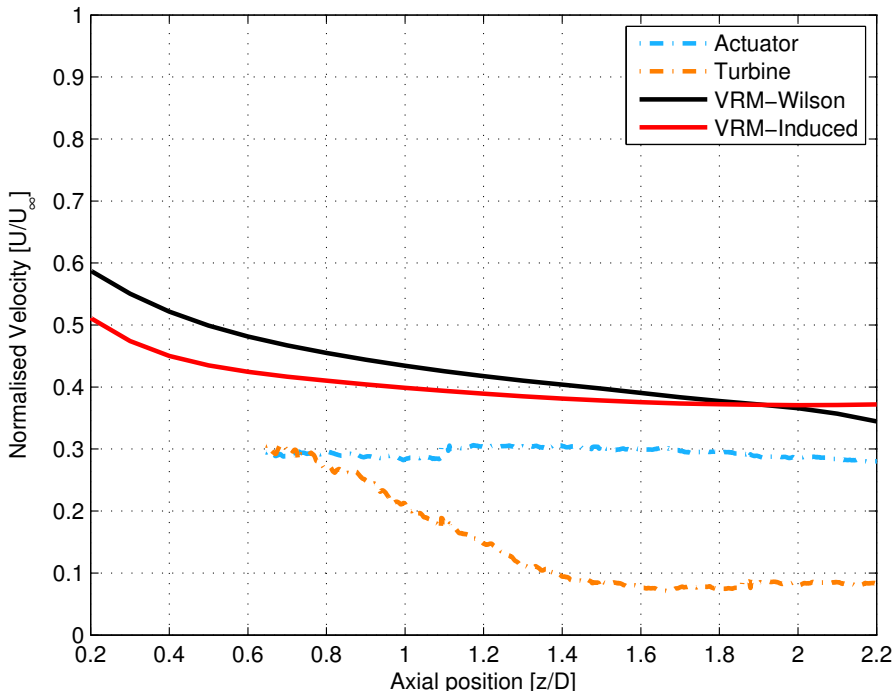


Figure 4.7: Comparison of centreline velocities between the wind tunnel data and the model

The results of the 2-bladed turbine show a relatively higher velocity deficit around $r = 0$, which is more clearly visible in figure 4.7, where the velocities along the centreline are plotted. This is most likely due to the blockage effect of the hub, which is only present on the 2-bladed rotor and not on the porous disc. It is also observed that the centreline velocities of the Wilson wake expansion simulation are slightly lower compared to the induced expansion model. This seems to make sense, since the principle of continuity determines that a more expanded wake should result in lower velocities. Both simulation results have slightly higher velocities at the centreline compared to the experiments. It should be noted though, that the velocities in the wake of the experiments have some fluctuation as is observed in figure 4.5.

Figure 4.8 displays time-averaged velocity fields of the experiments, overlaid by the positions of the vortex rings from the time-averaged and instantaneous simulations. If examined closely, it is observed that the rings of the simulation including the Wilson wake expansion, are positioned outside of the wake shear layer, whereas the rings of the induced expansion simulation are more positioned inside of the shear layer. The display of strong vortex ring interaction seems to correspond with the destabilisation and growth of the wake shear layer, where the near-wake transitions to the turbulent far-wake. Further investigation would however be required to understand the relation between the mutual instabilities predicted by the dynamic (inviscid) vortex model and wake breakdown observations.

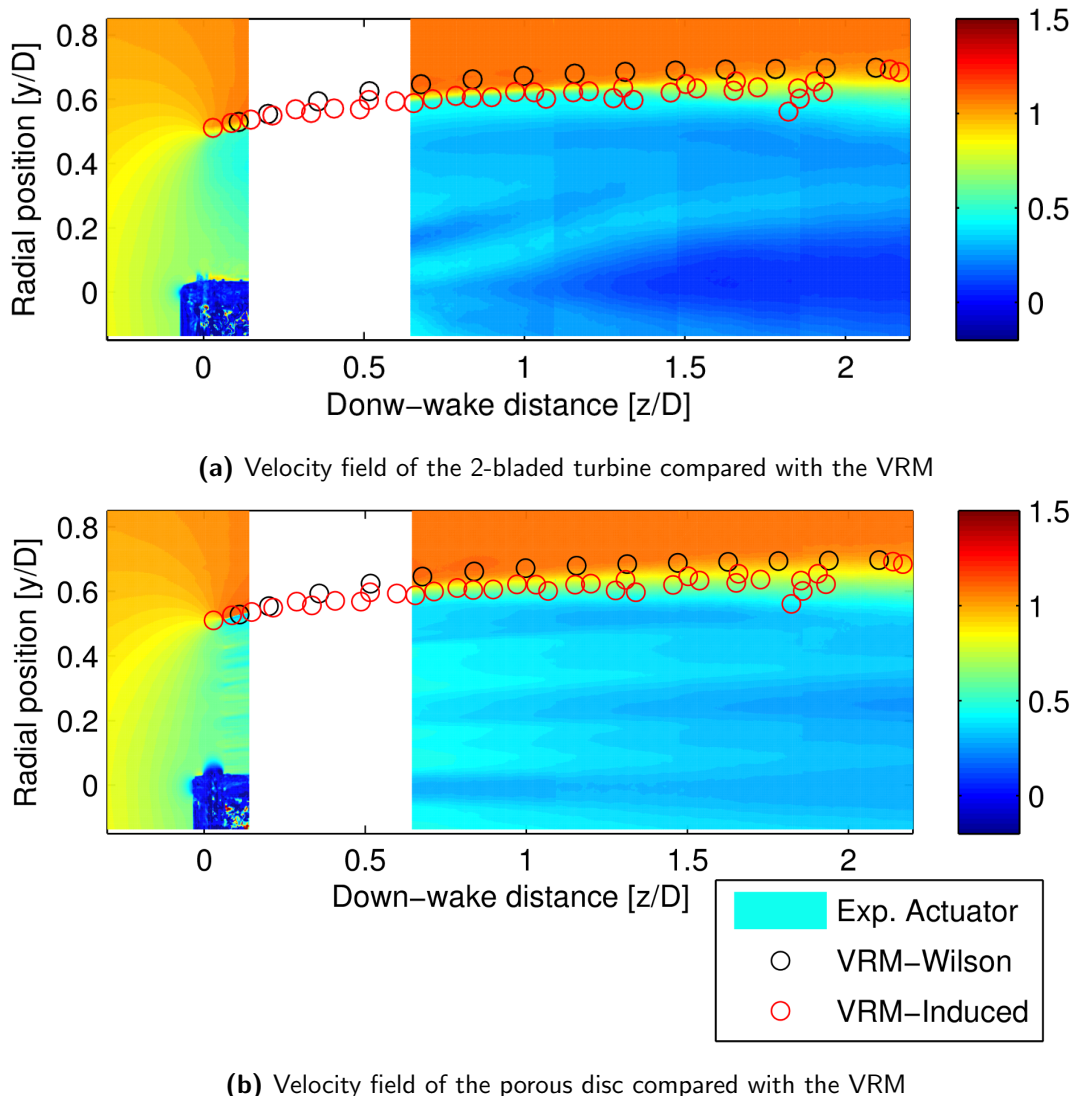


Figure 4.8: Non-dimensionalised velocity fields from the experimental results of the 2-bladed turbine and porous disc. Overlaid are the positions of the vortex rings of both expansion models after the simulation

4.3 Remarks on the VRM Validation Study

The constrained expansion model was in favour of the induced expansion model due to the numerical stability and reduced computation time. However, the induced expansion model shows a much better agreement with the experimental data, which can't be ignored. Therefore, the induced free-wake expansion model is used for implementation in the Jensen and Larsen wake models. The penalties are a longer computational time and the loss of accordance with blade tip vortices.

Chapter 5

Coupling of the Vortex Ring Model with the Jensen Far-Wake Model

This chapter presents the research into a coupling method of the VRM with the Jensen far-wake model. First, the physical properties of the Jensen model are explained in section 5.1 for a technical understanding of the model. Section 5.2 shows the methodology used to couple the vortex ring and Jensen models. Results of this coupling are shown and discussed in section 5.3 and conclusions from these results are discussed in section 5.4.

5.1 Characteristics of the Jensen Far-Wake Model

The Jensen model is briefly discussed in Chapter 2, but a more thorough understanding of the model is presented in this section. Jensen [23] assumed a linear expanding wake with a ‘hat’ profile as is schematically displayed in figure 5.1.

The linear wake expansion is described with:

$$r = kz + r_0 \quad (5.1)$$

Here, r is the wake radius and r_0 the rotor radius. k represents the Wake Decay Coefficient (WDC) and represents the expansion of the wake due to atmospheric turbulence. The WDC is initially based on the terrain roughness. Recent research has established a relation between the WDC and the Turbulence Intensity (TI), a flow property which is nowadays used to describe the effect of terrain roughness on the earth’s boundary layer. A conversion table with advised values representing turbulence intensities and WDC can be seen in table 5.1. This table is used to compare the effect of turbulence between the Jensen and Larsen models.

The initial velocity deficit in the wake is derived from the actuator disc momentum theory where the velocity after the turbine is determined with the axial induction factor a :

$$U_0 = U_\infty(1 - 2a) \quad (5.2)$$

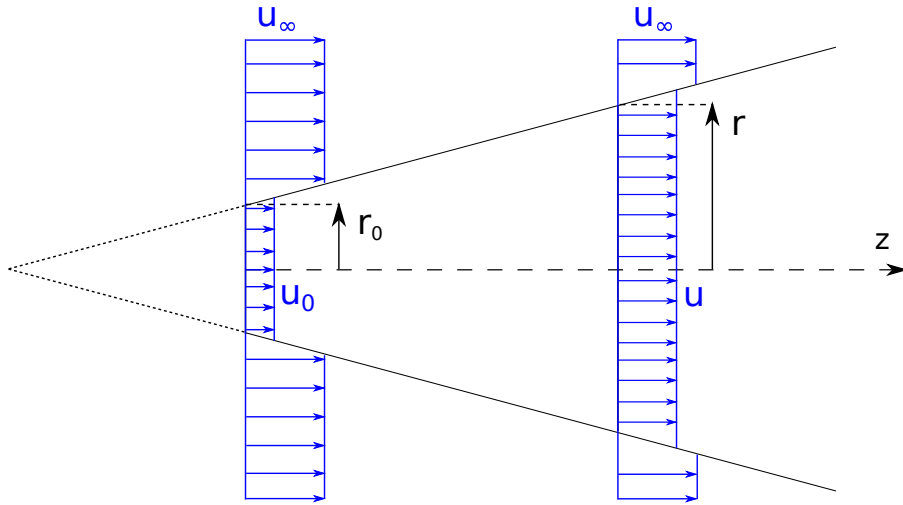


Figure 5.1: Schematic overview of the Jensen far-wake model

Table 5.1: An estimated relation between TI and k from Choi and Shan [9]

Turbulence Intensity (TI) [%]	Wake Decay Coefficient (k) [-]
8	0.040
10	0.052
13	0.063
15	0.075
16	0.083
18	0.092
21	0.100
24	0.108
29	0.117

This initial wake deficit is placed directly at the position of the rotor. The model does not implement a gradual decay in the near-wake, which is more common with the actuator disc momentum theory. The relation between the initial wake deficit and the deficit at an arbitrary down-wake position as displayed in figure 5.1 is derived from the balance of mass¹:

$$\pi r_0^2 U_0 + \pi(r^2 - r_0^2) U_\infty = \pi r^2 U \quad (5.3)$$

Substituting equations 5.2 and 5.1 into 5.3 and solving for U gives the final expression for the velocity in the wake at an arbitrary position z :

$$U = U_\infty \left[1 - 2a \left(\frac{r_0}{r_0 + kz} \right)^2 \right] \quad (5.4)$$

¹In the original publication [23], Jensen claimed to use conservation of momentum to derive the velocities in the wake. However, Bastankhah and Porté-Agel [6] correctly pointed out that it was in fact conservation of mass.

A solution to overlapping wakes was first published by Katic et al. [25]. It is assumed that the kinetic energy deficit of a mixed wake is equal to the sum of each contributing wake deficit as described in equation 5.5.

$$\left(1 - \frac{U}{U_\infty}\right)^2 = \left(1 - \frac{U_1}{U_\infty}\right)^2 + \left(1 - \frac{U_2}{U_\infty}\right)^2 + \dots + \left(1 - \frac{U_N}{U_\infty}\right)^2 \quad (5.5)$$

Here, U_1 , U_2 and U_N are the individual deficit velocities of each contributing wake. A more general formulation is presented by Choi and Shan [9] as:

$$U_i = U_0 \left[1 - \sqrt{\sum_{k=1}^{i-1} \left(1 - \frac{u_{k,i}}{U_0}\right)^2} \right] \quad (5.6)$$

Here, $u_{k,i}$ is the wind speed in the wake of turbine k , in front of turbine i . U_i is the wind speed in front of wind turbine i and U_0 is the undisturbed wind speed.

5.2 VRM and Jensen Coupling Methodology

The simplistic nature of the Jensen model, made it difficult to find a way to couple the results of a vortex ring simulation with the input parameters of the Jensen model. The Jensen model does not contain a near-wake description, so the initial deficit of the Jensen model has to be shifted towards the end of the near-wake. The simulations from Chapter 4 have shown that $2D$ is a reasonable position to transfer from near- to far-wake, but this position is arbitrary. The near-wake region ($0 - 2D$) of the Jensen model is then substituted with the calculated velocities of the vortex ring model. The remaining far-wake is calculated with the Jensen model and has to be tuned to fit the results of the near-wake development with one of the following parameters:

- The Wake Decay Coefficient k
- The axial induction factor a
- The undisturbed wind velocity U_∞

The WDC represents turbulence intensities and since the VRM is inviscid, this is left as an arbitrary input. The undisturbed wind velocity is a constant and is also found to be unsuitable to alter with respect to the near-wake model. The axial induction factor could be changed as input, while still respecting the fundamentals of the model. The induction in the near-wake can be determined with the VRM. Two options are considered to implement this coupling.

The far-wake could be implemented from at the end of the near-wake by placing a virtual rotor at this position, with the determined velocity deficit from the VRM. This would be the most simple solution, but the rapid wake recovering character of the Jensen model gives an abrupt increase in wind speed after the transition.

A second and more suitable option is to “correct” the Jensen model in the far-wake with the information acquired from the VRM, which has a more physical meaning. The velocities at the junction are determined with the VRM. The Jensen model is then altered with the input a , until a fit is obtained with the velocities from the VRM at the transition. Subsequently, only the determined velocities in the far-wake are used from the Jensen model. The process can be summarized as follows and is displayed in figure 5.2.

1. A distinction is made in near-wake and far-wake. This position is arbitrary.
2. The centreline velocity in the wake at the position of the near- far-wake transition is determined from the VRM.
3. A solver is set up to find a value for the axial induction factor input a of the Jensen model, that matches the centreline velocity in the wake from the VRM.
4. This value for a is used in the Jensen simulation with U_∞ (known) and k (arbitrary).
5. A Jensen simulation is run towards an arbitrary distance down-wake.
6. The results of the near-wake VRM simulation and far-wake Jensen simulation are combined for a complete view of the turbine’s wake field.

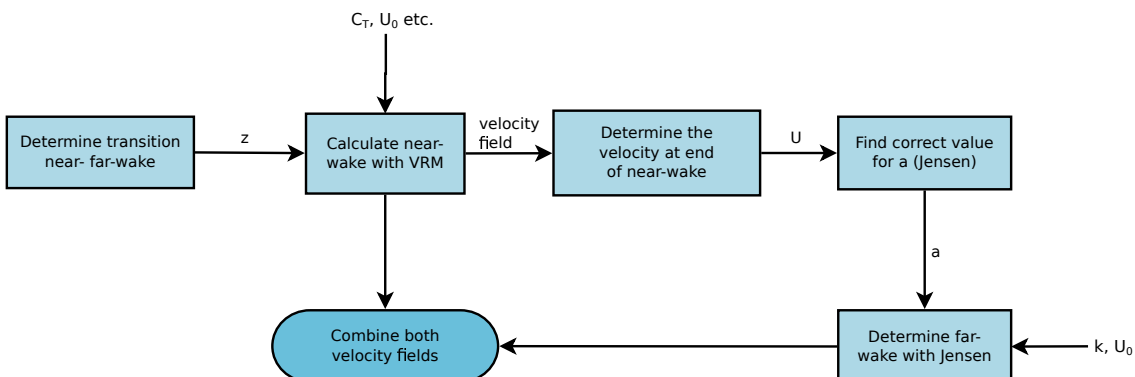


Figure 5.2: Schematic overview of the VRM-Jensen coupling

5.3 Results of the VRM-Jensen Coupling

Simulations were performed for a high thrust case (5.3.1), a low thrust case (5.3.2) and a hight thrust with high turbulence case (5.3.3). In all cases, the induced free-wake expansion model² was used for the VRM and the far-wake was simulated up to 16D. The results of the VRM-Jensen coupling and of the Jensen reference model are shown for comparison.

²Two different expansion models were developed in the VRM as discussed in section 3.4.

5.3.1 Single Wake Solutions for $C_T = 8/9$ (Low Turbulence)

Figures 5.3 and 5.4 show the resultant velocity field of both simulations. In this simulation, the wake decay coefficient was kept small at $k = 0.04$, which corresponds to a low atmospheric turbulent case ($TI = 8\%$), often referred to as offshore conditions. Although the domain is large and the resolution kept moderate for computational resource purposes, the difference in near-wake can easily be distinguished. The figures serve for a global comparison and a quick overview of the result.

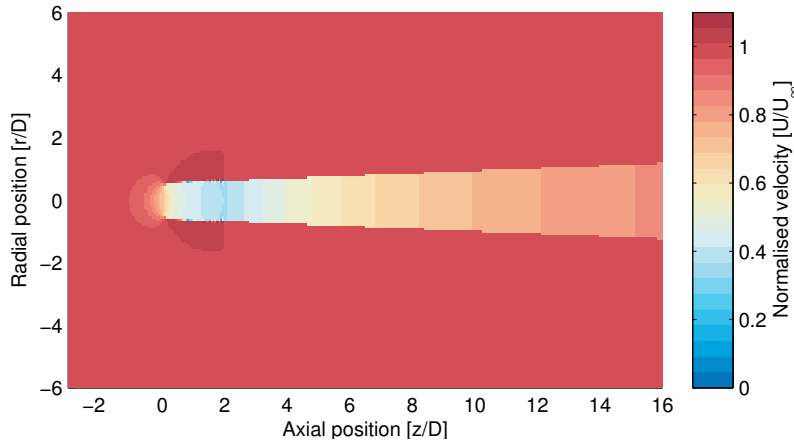


Figure 5.3: Velocity field of a turbine with $C_T = 8/9$ from a VRM-Jensen simulation

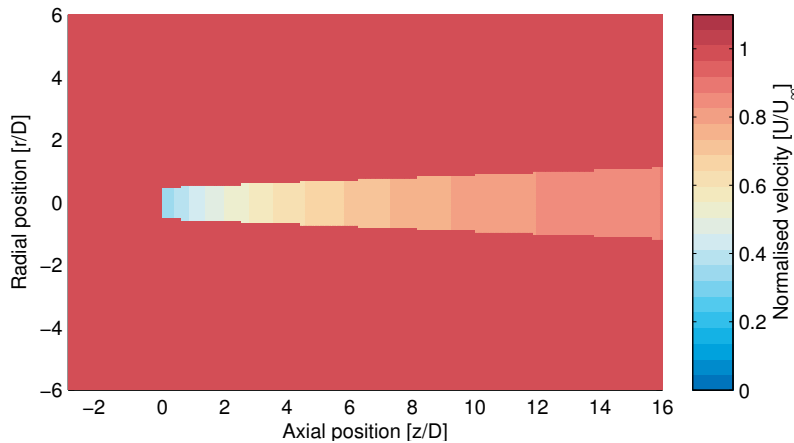


Figure 5.4: Velocity field of a turbine with $C_T = 8/9$ from a standard Jensen simulation

Figure 5.5 shows the velocity along the centreline and figure 5.6 shows the wake profiles at various down-wake positions for both simulations. Wake recovery of the VRM-Jensen coupling is delayed with respect to the reference model due to the existence of the near-wake model. The difference in velocity is however relatively small. The wake profiles are very similar, since the expansion in the far-wake is dominated by the Jensen model and is only dependent on the Wake Decay Coefficient k .

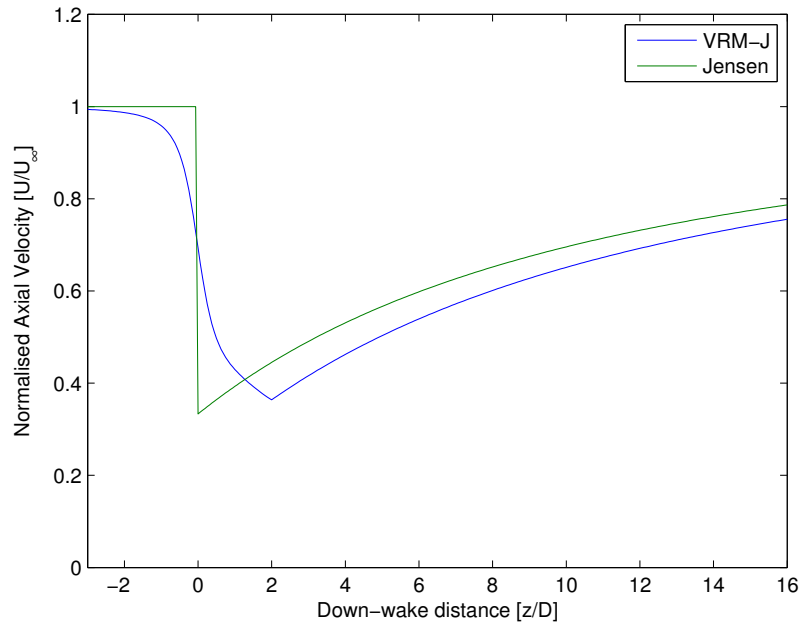


Figure 5.5: Velocities along the centerline with $C_T = 8/9$ for the VRM-Jensen coupling and the standard Jensen simulation

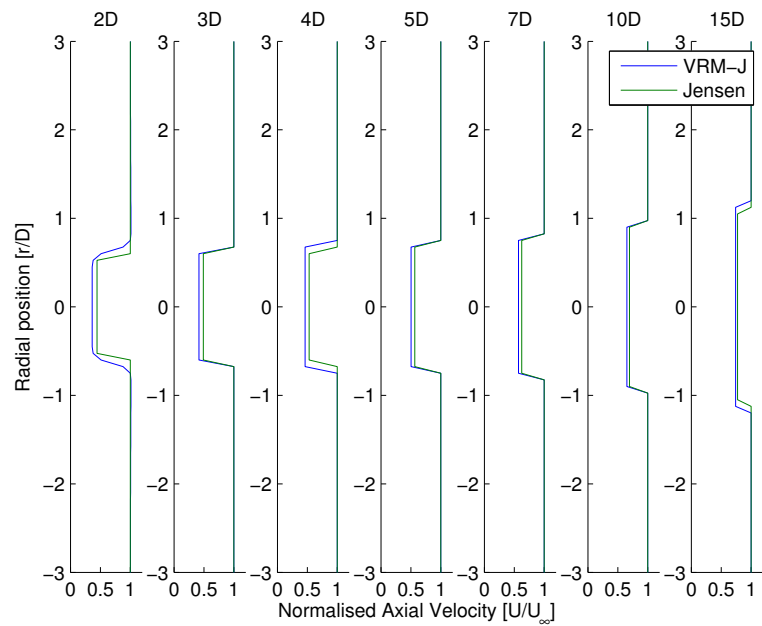


Figure 5.6: Velocities profiles for $C_T = 8/9$ for the VRM-Jensen coupling and the standard Jensen simulation

5.3.2 Single Wake Solutions for $C_T = 5/9$ (Low Turbulence)

The same simulation was performed for a low thrust scenario at the same atmospheric turbulence level. The velocity fields are displayed in figures 5.7 and 5.8 respectively. As expected, the initial velocity deficit is lower compared to the previous case due to the lower value for C_T .

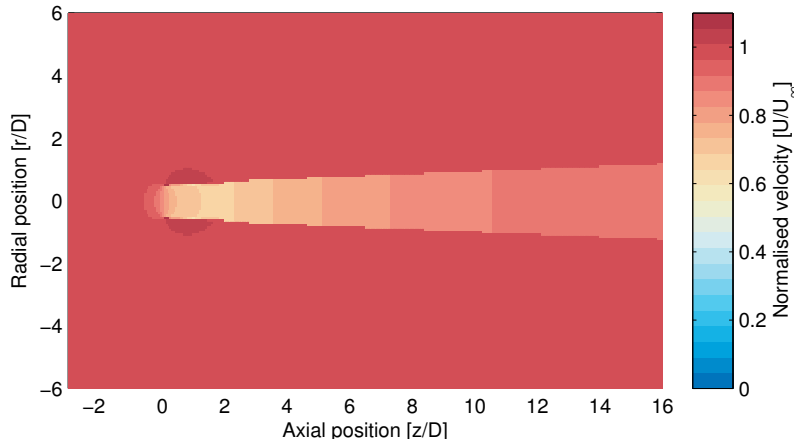


Figure 5.7: Velocity field of a turbine with $C_T = 5/9$ from a VRM-Jensen simulation

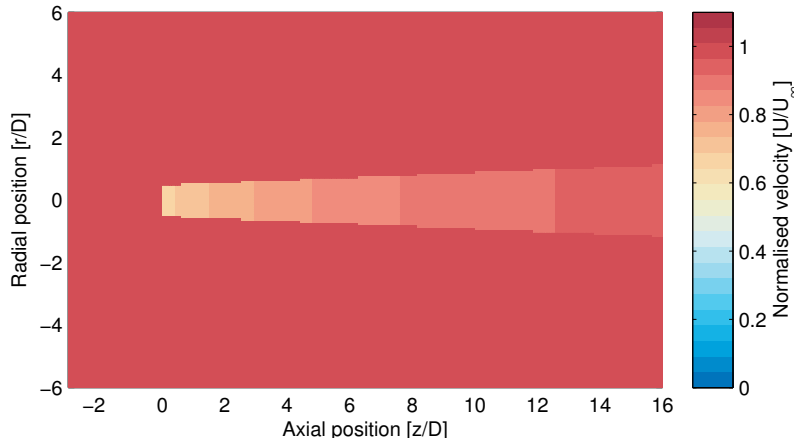


Figure 5.8: Velocity field of a turbine with $C_T = 5/9$ from a standard Jensen simulation

Figure 5.9 shows again the centreline velocities of the simulations. The combined VRM-Jensen model recovers similar with respect to the reference Jensen model. The transition between near- and far-wake is smoother compared to the high thrust case, since the gradient is lower on the Jensen part of the model. From figure 5.10 it is clear the initial expansion of both models is very similar, which results in an equal expansion throughout the wake.

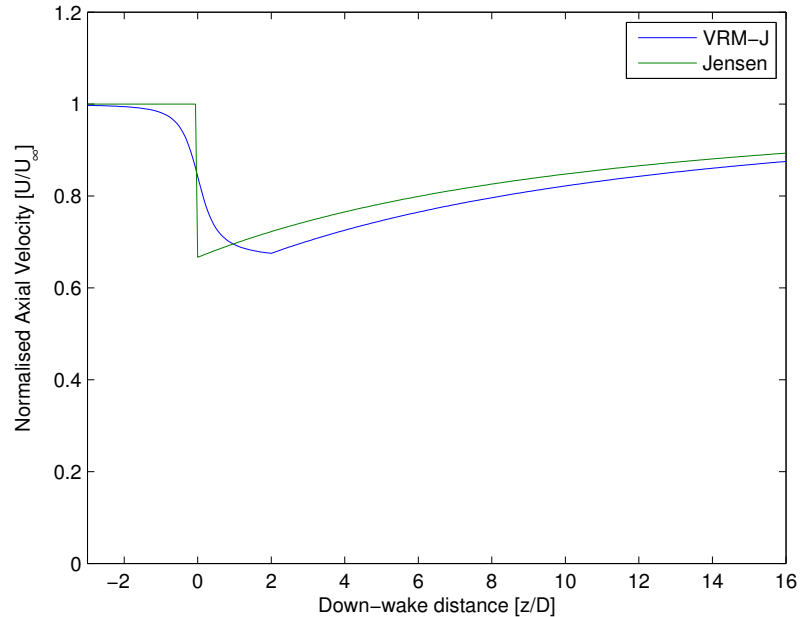


Figure 5.9: Velocities along the centerline with $C_T = 5/9$ for the VRM-Jensen coupling and the standard Jensen simulation

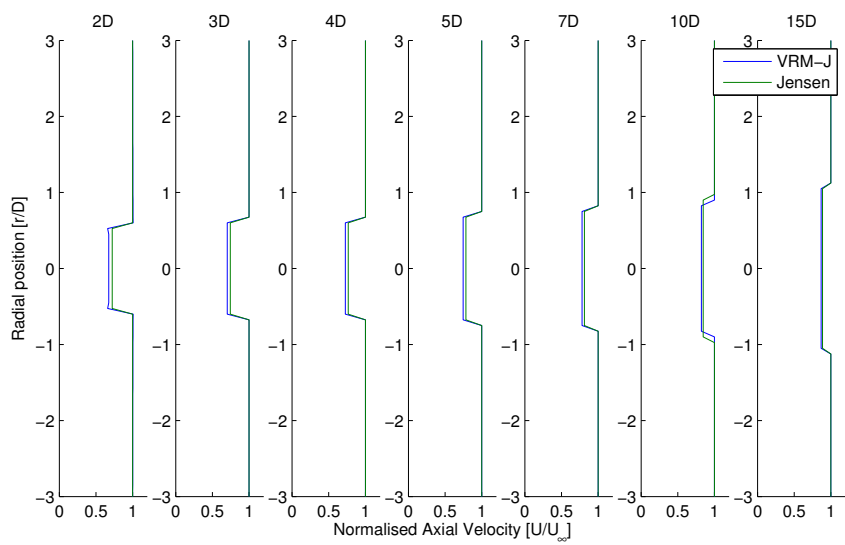


Figure 5.10: Velocities profiles for $C_T = 5/9$ for the VRM-Jensen coupling and the standard Jensen simulation

5.3.3 Single Wake Solutions for $C_T = 8/9$ (High Turbulence)

A simulation with higher turbulence was performed, to investigate the effect of the near-wake on the far-wake with respect to the atmospheric turbulence present. A value of $k = 0.1$ was used which refers to a turbulence intensity of 21%, a more onshore condition. Figures 5.11 and 5.12 show that the wake expansion and recovery are higher with respect to the low turbulence case. The centreline velocities displayed in figure 5.5 seems most interesting as it appears that the difference in velocity is significantly larger compared to the low turbulence case. The largest deviation seems to be in the range of $3D$ to $10D$. In general this is in the range of the spacing used in wind farm layout design.

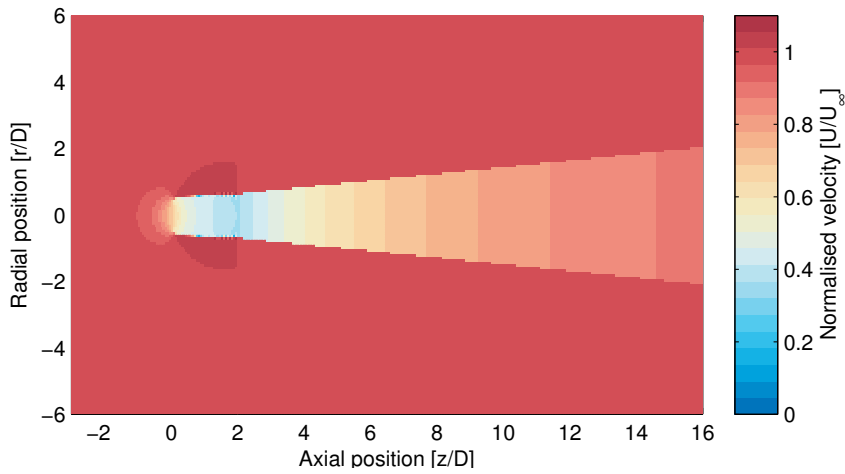


Figure 5.11: Velocity field of a turbine with $C_T = 8/9$ from a VRM-Jensen simulation with turbulence

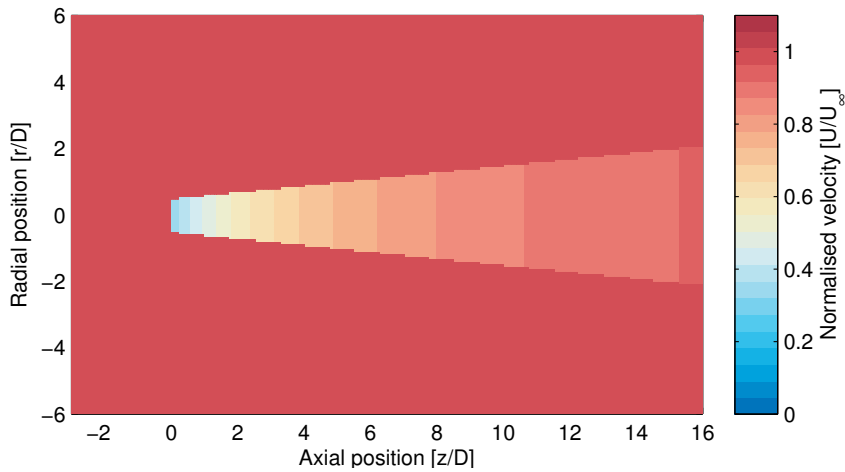


Figure 5.12: Velocity field of a turbine with $C_T = 8/9$ from a standard Jensen simulation with turbulence

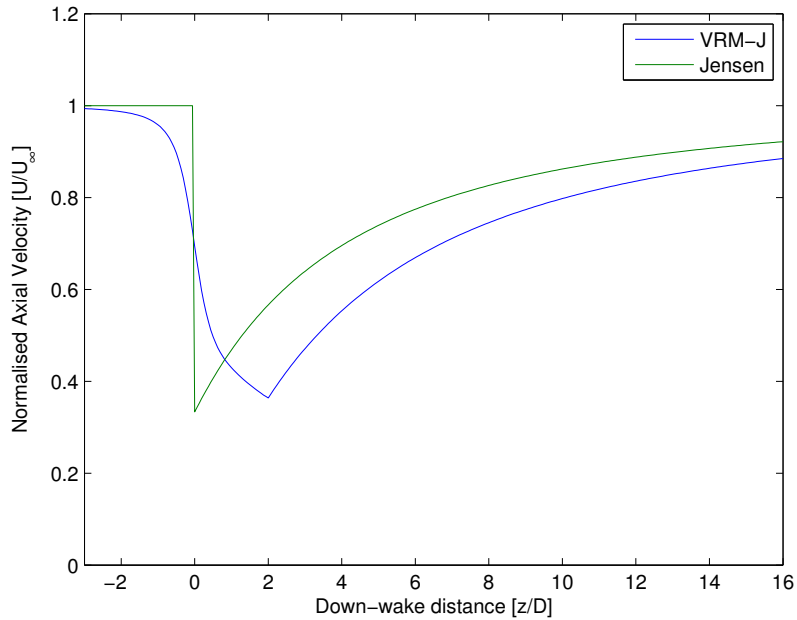


Figure 5.13: Velocities along the centerline with $C_T = 8/9$ for the VRM-Jensen coupling and the standard Jensen simulation with turbulence

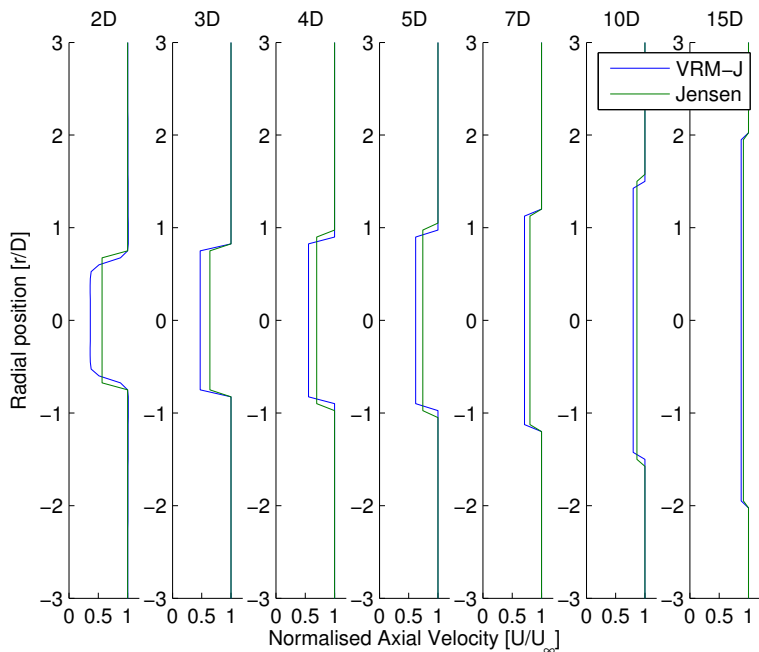


Figure 5.14: Velocities profiles for $C_T = 8/9$ for the VRM-Jensen coupling and the standard Jensen simulation with turbulence

5.4 Conclusions from the VRM-Jensen Results

In general, the Jensen model does not significantly change when coupled to the vortex ring model. A more general wake recovery is observed, but in a case with high turbulence, the instant recovering character of the Jensen model is still present and results in sharp behaviour of the centreline velocity. The arbitrary distinction between near- and far-wake which was set at $2D$ seems most fitting with a turbine operating at a low thrust coefficient which presents the smoothest transition of all cases. The largest difference between the VRM-Jensen and Jensen model is observed in the high turbulence case, where the models differ in wake recovery between $2D$ and $10D$, but ultimately converge. This could be an interesting result in wind farm layout optimization and AEP, since this is in the region of typical spacings used in offshore wind farms.

The Jensen model was chosen for its simplicity and while this is true for the far-wake part of the model, the implementation of the VRM was more difficult than expected. It is easier to replace an existing near-wake model than to implement one in a non-existing case.

Chapter 6

Coupling of the Vortex Ring Model with the Larsen Deficit Model

This chapter presents the methodology of implementing the VRM into the Eddy Viscosity based Larsen wake deficit model. An extended elaboration of the Larsen deficit model, the currently used near-wake implementations and the concept of Eddy Viscosity as derived by Ainslie [2] are discussed in section 6.1 and 6.2. Section 6.3 describes how the VRM is implemented in the model and how the continuity and momentum equations are discretized on a Cartesian grid. A qualitative comparison between the Ainslie and Larsen implementation of the concept of Eddy Viscosity is performed and discussed in section 6.4 and the numerical implementation of the Larsen model is verified with literature in section 6.5. Finally, section 6.6 presents findings of a comparison between the VRM-Larsen model and the reference streamtube-Larsen model with different thrust en atmospheric turbulence conditions.

6.1 Initial Wake Deficit of the Dynamic Wake Meandering Model

A basic outline of the Dynamic Wake Meandering (DWM) Model is presented in Chapter 2, where the various parts of the model are explained. The wake deficit part of the DWM model is only discussed globally and an extended explanation of the working principle of the wake deficit model is shown in this section.

The wake deficit model of the DWM model is schematically shown in figure 6.1. The first two boxes displayed, represent the near-wake part of the model. This part is replaced by the VRM, which will be discussed in section 6.3. The original near-wake model is used as a reference model for comparison and requires some elaboration.

First a uniform inflow is assumed in front of the rotor. This implies that the possible effect of earth's boundary layer wind shear profiles or yawed inflow conditions are neglected.



Figure 6.1: Schematic of the Wake Deficit model in the Dynamic Wake Meandering Model

These conditions are neglected in the VRM as well, so one could argue that the first step is similar for both near-wake models.

Secondly the initial wake deficit and expansion are determined. Two methods have been found in literature and both methodologies are used in comparison and must be elaborated. The first methodology was published with the original publication from Ainslie [2], which is based on empirical correction values. The second methodology was derived by Larsen et al. [32] and is based on streamtube momentum theory and continuity.

6.1.1 Ainslie's Calculation of the Initial Wake Deficit

Ainslie states that pressure gradient will no longer dominate the flow after a distance of $2D$. It is assumed that at this distance, the wake has the shape of a Gaussian distribution which can be described with equation 6.1. An example of a Gaussian shape is shown in figure 6.2.

$$1 - \frac{U}{U_\infty} = D_M e^{-3.56(\frac{r}{b})^2} \quad (6.1)$$

where,

U = axial wind velocity

U_∞ = undisturbed wind velocity

D_M = centreline velocity deficit

r = radial position

b = wake width

In this equation, the velocity deficit D_M is derived from wind tunnel rotor data at a position of $2D$. It can be described with the empirical relation in equation 6.2.

$$D_M = C_T - 0.05 - (16C_T - 0.5) \frac{A}{1000} \quad (6.2)$$

Here, A represents the ambient turbulence intensity (%) and C_T the thrust coefficient of the wind turbine. The wake width b is then calculated from the conservation of momentum:

$$b = \sqrt{3.56 \frac{C_T}{8D_M(1 - 0.5D_M)}} \quad (6.3)$$

The method used by Ainslie is compared with Larsen's streamtube momentum model in section 6.4.1. It should be noted that the near-wake description by Ainslie is highly based on empirical wind turbine data from the 1980's.

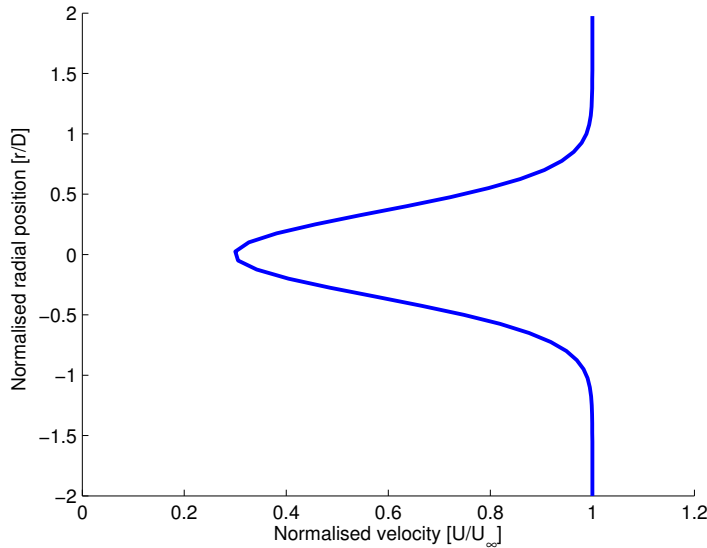


Figure 6.2: Example of a Gaussian velocity profile for $C_T = 8/9$ and $A = 10\%$

6.1.2 Streamtube Momentum / BEM Model

The near-wake model based on streamtubes was first published in the report on the DWM Model by Larsen [32], and later elaborated in 2008 [34]. While Ainslie clearly states that the initial deficit should be implemented at $2D$, Larsen states this distance more vaguely, as somewhere between $2D$ to $3D$, where the pressure is assumed to have fully recovered.

The turbine is assumed to operate at the Betz optimum. The resulting velocity at the end of the near-wake, where the pressure is assumed to have recovered can then be described as $(1 - 2a)U_\infty$.

The wake is represented by streamtubes as displayed in figure 6.3. For each streamtube, the mass flow can be determined at the location of the turbine and in the wake. Due to the laws of continuity, they should be equal.

$$\dot{m}_i = \rho\pi U_\infty(1 - a_i)(r_{t,i+1}^2 - r_{t,i}^2), i = 1, \dots, N - 1 \quad (6.4)$$

$$\dot{m}_i = \rho\pi U_\infty(1 - 2a_i)(r_{w,i+1}^2 - r_{w,i}^2), i = 1, \dots, N - 1 \quad (6.5)$$

If equations 6.4 and 6.5 are combined, an expression for the wake radius can be established:

$$r_{w,i+1} = \sqrt{\frac{1 - a_i}{1 - 2a_i}(r_{t,i+1}^2 - r_{t,i}^2) + r_{w,i}^2} \quad (6.6)$$

The expression for the velocity in the wake as function of r is provided in equation 6.7. Note that the centre radius of the streamtube is taken as an average.

$$U_w \left(\frac{r_{w,i+1} + r_{w,i}}{2} \right) = U_\infty(1 - 2a_i) \quad (6.7)$$

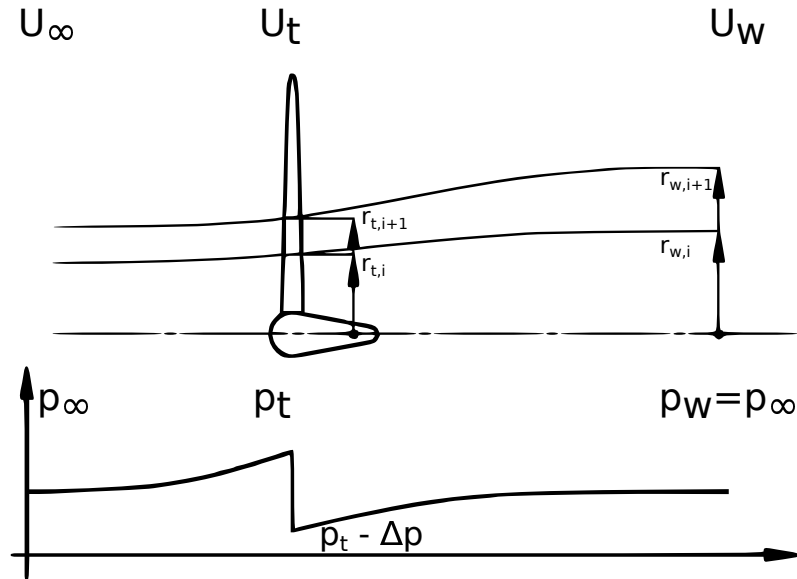


Figure 6.3: Schematic Representation of the near-wake

The discretization of the wake into steamtubes makes it compatible with a Bladed Element Momentum (BEM) approach of the rotor, where the local induction factor for every blade element can be calculated from blade properties. In the current approach, an actuator disc is used which is uniformly loaded. This implies that the induction factor is constant along the radius. This results in a hat-shaped wake profile, which is not an accurate description of the near-wake, but was intended solely as an input to the far-wake model.

6.2 Far-Wake and the Eddy Viscosity Concept

The far-wake deficit of the Larsen model is based on the concept of Eddy Viscosity derived by Ainslie [2]. The turbulent mixing process is described with rotationally symmetric Navier-Stokes equations, where the pressure is assumed to be constant. The thin shear layer approximation is applied to the far-wake flow, i.e. radial flow derivatives are considered to be much larger than axial derivatives. The resultant momentum and continuity equations that follow from these simplifications are described in equations 6.8 and 6.9 as:

$$U \frac{dU}{dz} + V \frac{dU}{dr} = -\frac{1}{r} \frac{d}{dr} (r \bar{u} \bar{v}) \quad (6.8)$$

$$\frac{V}{r} + \frac{dV}{dr} + \frac{dU}{dz} = 0 \quad (6.9)$$

where U and V describe the velocities in axial and radial direction respectively, z the axial position in the wake and r the radial position. $\bar{u} \bar{v}$ represent the temporal averaged fluctuating velocity components in axial and radial directions. Using the concept of Eddy

Viscosity, these Reynold stresses are expressed as:

$$-\bar{u}\bar{v} = \nu_T \frac{dU}{dr} \quad (6.10)$$

The term ν_T is referred to as the EV-term and consists of suitable velocity- and length scales of the turbulence. The EV-term is dependent on the ambient turbulence levels and the relative wake deficit with respect to the undisturbed wind flow. There are multiple ways to implement these quantities into an estimation, combined with empirical data and filter functions. Two methods of determining this quantity have been implemented in this research. The original method from Ainslie [2] and a newer method first derived by Larsen [34] and improved by Madsen et al. [37] and Keck et al. [27] which are discussed in the following subsections. Substituting the EV-term in the equation 6.8, results in the final momentum equation:

$$U \frac{dU}{dz} + V \frac{dU}{dr} = \frac{\nu_T}{r} \left(\frac{dU}{dr} + r \frac{d^2 u}{dr^2} \right) \quad (6.11)$$

6.2.1 Ainslie's Concept of Eddy Viscosity

Ainslie described the shear stresses in the Eddy Viscosity concept with:

$$\epsilon = l_w(x) U_w(x) + \epsilon_a \quad (6.12)$$

Here, l_w and U_w are length and velocity scales, which describe the wake shear layer. For l_w , the wake half length b is used. In the implemented model, b is fixed at $1.2R$, which represents the average expansion of the wake. The velocity scale U_w is determined as the velocity difference $U_0 - U_c$ across the wake shear layer, where U_0 represents the undisturbed wind speed and U_c the centreline velocity. Both l_w and U_w are thus only dependent on the axial position and independent of the radial coordinate. A constant k_1 is used which is a property of the shear layer, independent of ambient turbulence. Experiments with wind tunnel data were performed in [2] which concluded that a value of 0.015 was a good fit in most situations.

The variable ϵ_a represents the momentum transfer in the atmosphere and can be described in terms of normal boundary layer parameters. If a logarithmic wind profile is assumed, the value can be estimated with:

$$\epsilon_a = \frac{\kappa^2}{\ln(z_h/z_0)} \quad (6.13)$$

Where κ is the Von Kármán constant, z_h the hub height and z_0 the roughness length of the terrain.

Ainslie implemented a filter function on the Eddy Viscosity term, to correct for the lack of equilibrium between the mean velocity field and the turbulence field in the near-wake

region. Based on empirical data, he developed the following functions for the near wake (up to 5.5D):

$$\begin{aligned} x < 5.5 : F &= 0.65 + \sqrt[3]{\frac{x - 4.5}{23.32}} \\ x > 5.5 : F &= 1 \end{aligned} \quad (6.14)$$

It should be noted that there are multiple ways to interpret the filter function from Ainslie, since a cube root is used in the equation. It is assumed that only the real parts are valid and that the solution changes sign at $x = 4.5$, to give the curve the shape as it is displayed in figure 6.4.

The final result of the Eddy Viscosity formulation is displayed in equation 6.15:

$$\nu_T = F k_1 b (U_0 - U_c) + F \frac{\kappa^2}{\ln(z_h/z_0)} \quad (6.15)$$

Madsen et al. [37] derived a relation between the surface roughness length and the turbulence intensity TI:

$$TI = \frac{\alpha \kappa}{\ln(z_h/z_0)} \quad (6.16)$$

Where, $\alpha = 2.4$. The resemblance with equation 6.13 is logical, since both equations describe the same principle, but the whereabouts of the α parameter are unknown. It does, however provide a good way to describe the Eddy Viscosity in terms of turbulence (TI), rather than roughness length (z_0):

$$\nu_T = F k_1 b (U_0 - U_c) + F \frac{TI \kappa}{\alpha} \quad (6.17)$$

6.2.2 Larsen's Concept of Eddy Viscosity

The methodology used to describe the Eddy Viscosity term by Larsen in his original publication [32] was focussed on simplicity and proof of concept, rather than accuracy, since the focus on the model was on wake meandering. The model has later been improved numerous times and therefore various versions are scattered throughout literature, which is more elaborated at the end of this section. A calibrated and validated version by Madsen et al. [37] is used in this research, since his report is most elaborated in the discussion of all parameters and the report contains numerical results for a verification of the implemented model. A comparison of the results from Madsen and the implemented model are discussed in section 6.5.

Madsen continued the work by Larsen et al. [34] and described the EV-term similar to the methodology by Ainslie. The EV-term was based on the velocity and length scales of the turbulence, consisting of an ambient part (first part of equation 6.18) and a shear induced part (second part of equation 6.18):

$$\nu_T^* = \frac{\nu_T}{U_0 D} = F_1 k_{amb} TI + F_2 k_2 \frac{b}{R} \left(1 - \frac{U_c}{U_0} \right) \quad (6.18)$$

Here, U_c is the centreline axial velocity and U_0 is the undisturbed wind speed. D and R are the rotor diameter and radius and TI represents the non-dimensional turbulence intensity. b is referred to as the initial wake half width, which is a subjective reference. It is determined as the position where the velocity reaches 95% of the undisturbed wind speed U_0 , as described in Keck et al. [28]. The initial value for b is used for every axial position in Madsen, which is contrary to Keck, where the wake half width is re-evaluated at every axial position.

F_1 and F_2 are filter functions, depending on the down-stream distance z . They govern the rate of turbulence build-up in the wake, which is assumed to be a gradual process. Madsen did not explicitly state the equations used for the filter functions, but merely displayed the resulting graphs. From these, it was clear that a linear equation is used for F_1 and a polynomial was used to determine the curve of F_2 (see equation 6.19). The results are displayed in figure 6.4.

$$x < 2D : F_1 = x/2$$

$$F_2 = 0.035$$

$$x > 2D : F_1 = 1$$

$$2D < x < 10D : F_2 = P_6x^6 + P_5x^5 + P_4x^4 + P_3x^3 + P_2x^2 + P_1x + P_0$$

where,

$$P_6 = -0.000012893870797$$

$$P_5 = +0.000422682583300 \quad (6.19)$$

$$P_4 = -0.004747100430804$$

$$P_3 = +0.022327144728394$$

$$P_2 = -0.034407478155873$$

$$P_1 = +0.013036860495230$$

$$P_0 = +0.060975731301508$$

$$x > 10D : F_2 = 1$$

The empirical constants k_2 and k_{amb} , determine the gain of turbulence build-up and are based on empirical data or advanced CFD models. Madsen et al. [37] calibrated these constants with an actuator disc and actuator line based CFD model, which resulted in a value of $k_2 = 0.008$ and $k_{amb} = 0.07$, which were used in the current implementation of the model. The wake recovery of a simulated turbine is very sensitive to the values for k_{amb} and k_2 and various values for these constants have been scattered throughout literature. Keck proposed several improvements to the DWM, where the values for k_{amb} (often referred to as k_1) and k_2 have been recalibrated consistently. An overview of all differently calibrated values is displayed in table 6.1.

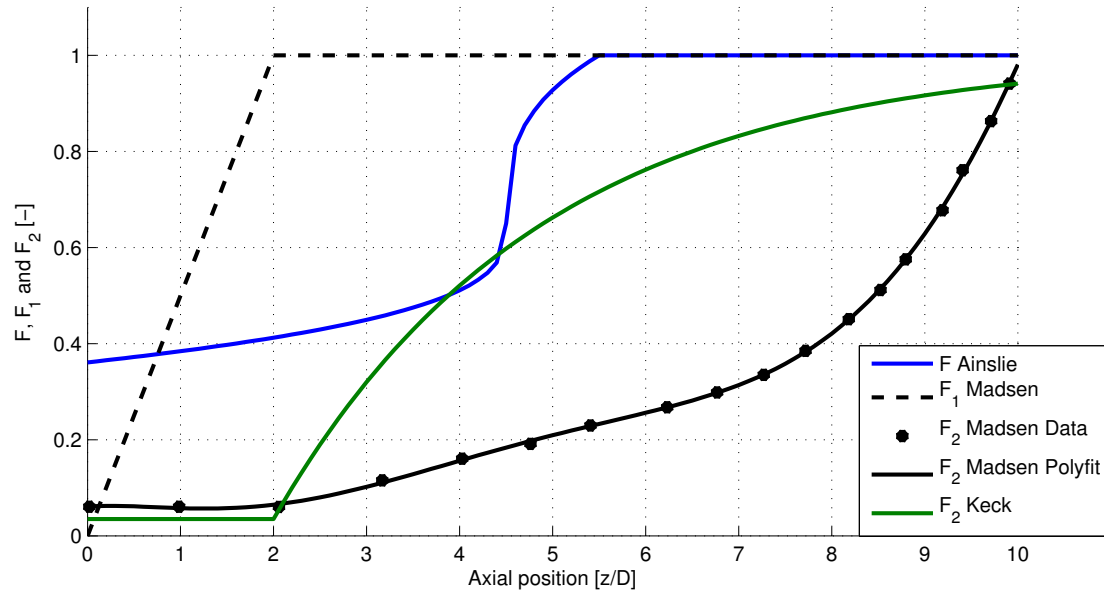


Figure 6.4: The filter functions from Ainslie and Keck for the atmospheric part of the Eddy Viscosity

Table 6.1: Referenced values for k_{amb} and k_2

Source		$k_{1/amb}$	k_2	Remarks
Ainslie [2]	1988	0.33	0.015	Notation of k_1 and k_2 is switched. For k_1 , see [37].
Larsen et al. [32]	2007	0	0.009	Only a shear layer contribution.
Larsen et al. [34]	2008	0.001	0.002	Notation of k_1 and k_2 is switched. TI most likely in [%]
Madsen et al. [37]	2010	0.07	0.008	
Keck et al. [28]	2012	0.0914	0.0216	Implementation of mixing length and different filter function F_2 .
Keck et al. [28]	2012	0.16	0.01	Referred to as “standard” DWM model
Keck et al. [27]	2013	0.587	0.0178	Recalibrated to implement atmospheric shear.

6.3 Methodology of the Vortex Ring Model and Larsen Coupling

To couple the VRM with the Larsen far-wake, the initial near-wake model of the Ainslie and Larsen models, need to be replaced. This is relatively simple compared to the earlier Jensen case, because the EV models present a good distinction between near- and far-wake. From the schematic in figure 6.1, it is clear that only the determination of the initial wake deficit needs to be substituted by the VRM.

The results of the near-wake model provide the initial conditions of the Larsen far-wake model. The velocities in the wake are further determined by solving the momentum (6.8)

and continuity (6.9) equations on a staggered grid, displayed in figure 6.5. The velocity field is assumed to be axi-symmetric. The velocities are calculated at radial positions and mirrored along the z -axis, to provide a full wake field.

The following steps are taken to provide a solution to the set of equations:

1. The momentum equation is applied to every cell on a fixed axial position j . This will result in a non-homogeneous linear system of equations. The upstream value of the Eddy Viscosity is used.
2. The same way, the continuity equation is solved for every radial position i at the fixed axial position j . The solution from step 1 is used to calculate the derivatives. The result is a second non-homogeneous linear system of equations.
3. The Eddy Viscosity term is updated for the radial positon j .

Since only upstream information is used in solving the system, the velocity field can be solved by “marching” downstream. At every instance the system of equations can be analytically solved, making the model very quick.

6.3.1 Discretizing of the Momentum and Continuity Equations

The derivatives of the momentum and continuity equations need to be discretized on a grid. The staggered grid used is shown in figure 6.5, which also displays the naming conventions used. The derivatives used in the set of equations are: $\frac{dU}{dz}$, $\frac{dU}{dr}$, $\frac{d^2U}{dr^2}$ and $\frac{dV}{dr}$.

Table 6.2: Discretized derivatives from the Momentum and Continuity equations

Derivative	Discrete form
$\frac{dU}{dz}$	$\frac{U_{(i,j)} - U_{(i,j-1)}}{dz}$
$\frac{dU}{dr}$	$\frac{U_{(i+1,j)} - U_{(i-1,j)}}{2dr}$
$\frac{d^2U}{dr^2}$	$\frac{\frac{U_{(i+1,j)} - U_{(i,j)}}{dr} - \frac{U_{(i,j)} - U_{(i-1,j)}}{dr}}{dr}$
$\frac{dV}{dr}$	$\frac{V_{(i-1,j)} - V_{(i+1,j)}}{2dr}$

The derivative in z -direction is discretized using an upwind finite difference scheme. The remaining derivatives in radial direction are discretized in a central finite difference scheme. An overview of this discretization is presented in table 6.2. The momentum equation for an arbitrary point (i, j) becomes:

$$U_{(i,j-1)} \frac{U_{(i,j)} - U_{(i,j-1)}}{dz} + \frac{U_{(i+1,j)} - U_{(i-1,j)}}{2dr} \left[V_{(i,j-1)} - \frac{\nu_t(i,j-1)}{r(i,j)} \right] - \nu_t(i,j-1) \left[\frac{\frac{U_{(i+1,j)} - U_{(i,j)}}{dr} - \frac{U_{(i,j)} - U_{(i-1,j)}}{dr}}{dr} \right] = 0 \quad (6.20)$$

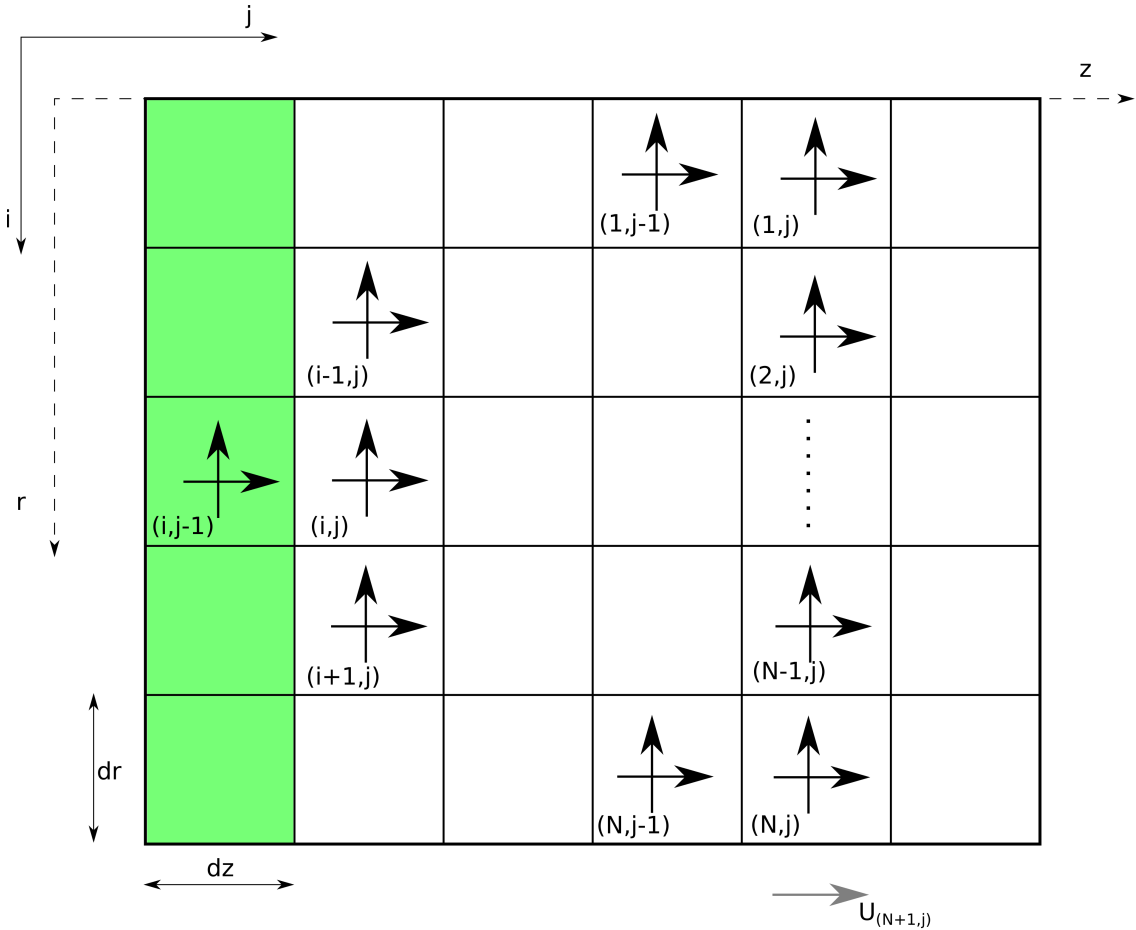


Figure 6.5: An overview of the grid with the used coordinate system and location of quantities used for discretization of the momentum and continuity equations

Equation 6.20 can be rewritten in a form that separates the unknown variables $U_{(i,j)}$, $U_{(i-1,j)}$ and $U_{(i+1,j)}$:

$$U_{(i,j)}A_1 + U_{(i-1,j)}A_2 + U_{(i+1,j)}A_3 = b \quad (6.21)$$

With,

$$\begin{aligned} A_1 &= \frac{U_{(i,j-1)}}{dz} + \frac{2\nu_{t(i,j-1)}}{dr^2} \\ A_2 &= \frac{-V_{(i,j-1)}}{2dr} + \frac{\nu_{t(i,j-1)}}{2r_{(i,j)}dr} - \frac{\nu_{t(i,j-1)}}{dr^2} \\ A_3 &= \frac{V_{(i,j-1)}}{2dr} - \frac{\nu_{t(i,j-1)}}{2r_{(i,j)}dr} - \frac{\nu_{t(i,j-1)}}{dr^2} \\ b &= \frac{U_{(i,j-1)}^2}{dz} \end{aligned}$$

For a grid with N rows, the final system has N unknowns (U in each cell) and N equations, which results in a standard $\mathbf{Ax} = \mathbf{b}$ system. In the same manner, the continuity equation

can be applied to an arbitrary point (i, j) :

$$\frac{V_{(i,j)}}{r_{(i,j)}} + \frac{V_{(i-1,j)} - V_{(i+1,j)}}{2dr} + \frac{U_{(i,j)} - U_{(i,j-1)}}{dz} = 0 \quad (6.22)$$

The newly found solution for $U_{(i,j)}$ is used. Rewriting equation 6.22 to separate the unknowns results in:

$$V_{(i,j)}B_1 + V_{(i-1,j)}B_2 + V_{(i+1,j)}B_3 = c \quad (6.23)$$

$$\begin{aligned} B_1 &= \frac{1}{r_{(i,j)}} \\ \text{with, } B_2 &= \frac{1}{2dr} \\ B_3 &= \frac{-1}{2dr} \\ c &= -\frac{U_{(i,j)} - U_{(i,j-1)}}{dz} \end{aligned}$$

6.3.2 Discretizing at the Boundaries

Special care is taken into discretizing at the boundaries of the domain. Two different boundaries can be distinguished. The first is the boundary for $i = 1$, which represents the edge at the axis of symmetry, thus the centre of the wake. The second is the boundary at $i = N$, which represents a point far from the turbine's wake. Both boundaries are treated differently.

At the boundary $i = 1$, the second derivative of U , $\frac{d^2U}{dr^2}$ is assumed to be zero, since the wake is axi-symmetric. Secondly, the first derivative of U , $\frac{dU}{dr}$, is discretized in a forward scheme rather than a central scheme. One could argue, that this derivative is also zero, but since a staggered grid is used, the location of the velocity points are not exactly on the z -axis and thus the derivative is not exactly 0. The derivative $\frac{dV}{dr}$ is determined by taking the gradient over the domain $r_i - 0.5dr$ to $r_i + dr$. Since the flow is symmetric, the radial velocity V must be zero at the centreline of the wake and the derivative can be discretized as $\frac{-V_{(i+1,j)}}{1.5dr}$. This quantity is determined at $r_i + 0.25dr$, but is transferred to r_i . This introduces a slight error, however if the resolution is kept high enough, this will be negligible. The resultant momentum and continuity equations at the boundary $i = 1$ are:

$$U_{(i,j)}A_1 + U_{(i+1,j)}A_3 = b \quad (6.24)$$

$$V_{(i,j)}B_1 + V_{(i+1,j)}B_3 = c \quad (6.25)$$

$$\begin{aligned}
A_1 &= \frac{U_{(i,j-1)}}{dz} - \frac{V_{(i,j-1)}}{dr} + \frac{\nu_{t(i,j-1)}}{r_{(i,j)} dr} \\
A_3 &= \frac{V_{(i,j-1)}}{dr} - \frac{\nu_{t(i,j-1)}}{r_{(i,j)} dr} \\
\text{with: } b &= \frac{U_{(i,j-1)}^2}{dz} \\
B_1 &= \frac{1}{r_{(i,j)}} \\
B_3 &= \frac{-1}{1.5 dr} \\
c &= -\frac{U_{(i,j)} - U_{(i,j-1)}}{dz}
\end{aligned}$$

The boundary $i = N$ is far from the turbine wake, so that it can be assumed that $\frac{d^2 U}{dr^2} = 0$, $U_{(N+1,j)} = U_0$ and $V_{(N+1,j)} = 0$. $U_{(N+1,j)}$ and $V_{(N+1,j)}$ are so-called “ghost points”, quantities outside the grid which have a fixed assumed value. By discretizing with these ghost points, the momentum and continuity equation at the boundary $i = N$, reduce to:

$$U_{(i,j)} A_1 + U_{(i-1,j)} A_2 = b \quad (6.26)$$

$$V_{(i,j)} B_1 + V_{(i-1,j)} B_2 = c \quad (6.27)$$

$$\begin{aligned}
A_1 &= \frac{U_{(i,j-1)}}{dz} \\
A_2 &= -\frac{V_{(i,j-1)}}{2dr} + \frac{\nu_{t(i,j-1)}}{r_{(i,j)} 2dr} \\
\text{with: } b &= \frac{U_{(i,j-1)}^2}{dz} - U_0 \left[\frac{V_{(i,j-1)}}{2dr} - \frac{\nu_{t(i,j-1)}}{r_{(i,j)} 2dr} \right] \\
B_1 &= \frac{1}{r_{(i,j)}} \\
B_2 &= \frac{1}{2dr} \\
c &= -\frac{U_{(i,j)} - U_{(i,j-1)}}{dz}
\end{aligned}$$

The discretization of the quantities at the boundary are summarized in table 6.3.

Table 6.3: Discretized derivatives at the boundaries

Derivative	Discrete form
For $i = 1$: (symmetry-axis, centreline)	
$\frac{dU}{dr}$	$\frac{U_{(i+1,j)} - U_{(i,j)}}{dr}$
$\frac{d^2U}{dr^2}$	0
$\frac{dV}{dr}$	$\frac{-V_{(i+1,j)}}{1.5dr}$
For $i = N$: (edge of domain)	
$\frac{dU}{dr}$	$\frac{U_0 - U_{(i-1,j)}}{2dr}$
$\frac{d^2U}{dr^2}$	0
$\frac{dV}{dr}$	$\frac{V_{(i-1,j)}}{2dr}$

6.4 A Qualitative Study of the Ainslie and Larsen Models

The Ainslie and Larsen far-wake models are both based on the concept of Eddy Viscosity, yet have a different implementation of the concept by the EV-term as discussed in section 6.2. A comparative study is performed to determine the differences in behaviour with regards to thrust and atmospheric turbulence intensity. For a fair comparison, the native near-wake models of Ainslie and Larsen are used, thus a Gaussian distribution with Ainslie and a streamtube momentum based on an actuator disc with Larsen.

6.4.1 Mutually Comparison of the Ainslie and Larsen EV Models

The Ainslie and Larsen models are compared with a variation in thrust (C_T) and atmospheric turbulence (TI). This results in the test matrix as displayed in table 6.4.

Table 6.4: Variables in the VRM - Far-wake coupling

Near-Wake	Far-Wake	C_T	TI
Gaussian	Ainslie EV	8/9	0%
Streamtube momentum	Larsen EV	5/9	21%

Figure 6.6 shows a comparison of the models for a laminar case with a maximum thrust coefficient. The difference in centreline velocities is quite high. The large initial deficit of the Ainslie model is partly related to the Gaussian shape which has a significant dip at the centre, which is shown in figure 6.6d. The Ainslie model shows a faster wake recovery, where the Larsen model starts to recover at a later stage in the wake, after roughly $8D$. The instant start of wake recovery in the Ainslie model is partly due to the larger difference of velocity across the shear layer, but the filter functions and empirical constant also have an influence. The Ainslie model shows a slower convergence with respect to the Larsen model, resulting in equal centreline velocities at around $16D$. The velocity profiles show that the wake shape also converges around this position to a similar solution for

both models. The centreline velocities are only part of the picture and should be analysed in conjunction with velocity profile graphs.

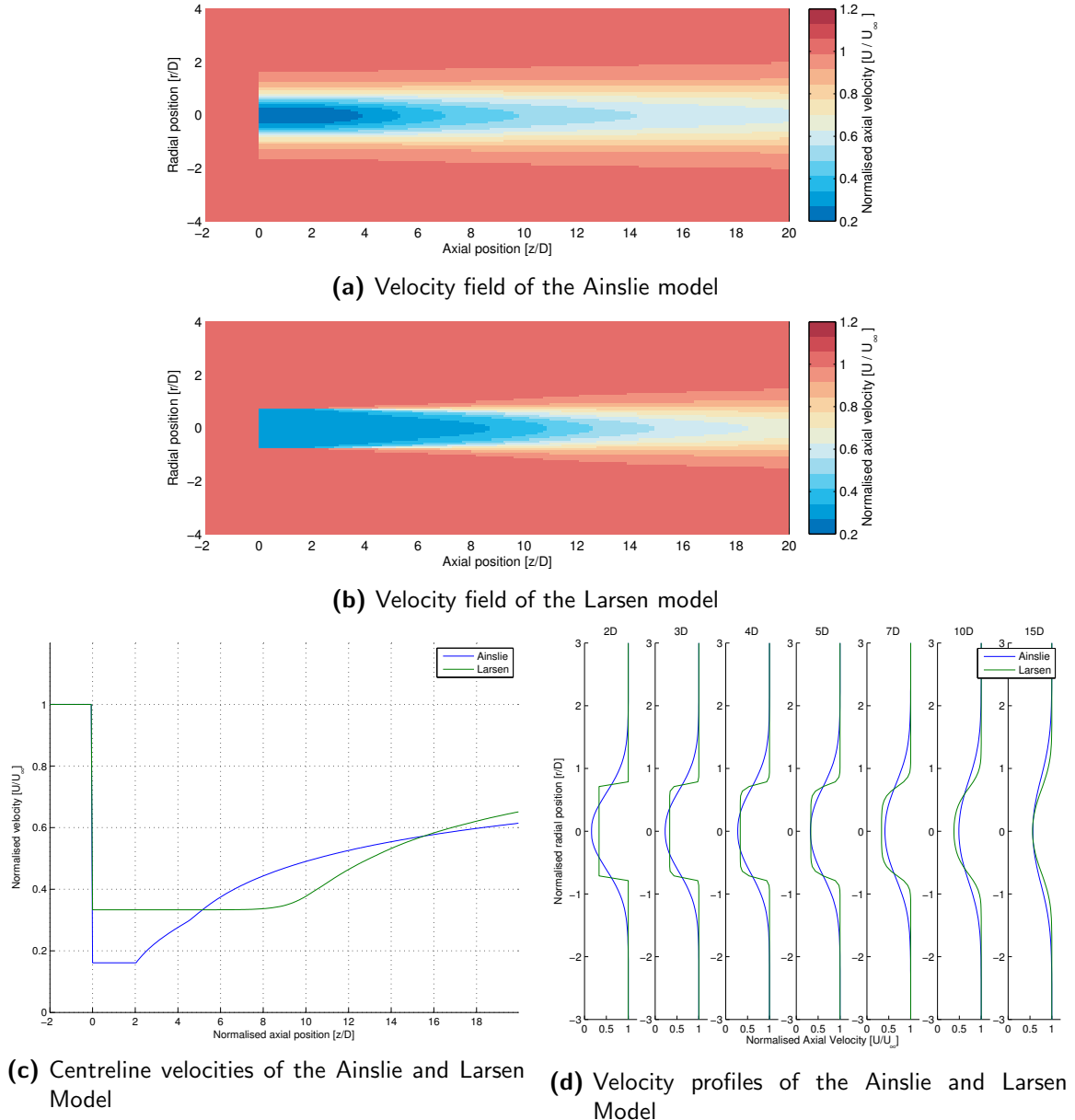


Figure 6.6: Results from an Ainslie-Larsen comparison with $C_T = 8/9$ and $TI = 0\%$

Figure 6.7 shows the centreline velocities and wake profiles of a comparison at a low thrust coefficient ($C_T = 5/9$). The initial difference in centreline velocities is again significant, but both solutions converge at around $10D$ and follow a similar recovery from there. Although the initial deficit is less compared to the higher thrust case, the wake recovery is weaker due to the smaller derivative of axial velocity over the flow boundary. This is observed in both models. This makes sense, since a lower thrust results in a lower Reynold stresses in the wake, which drives wake recovery.

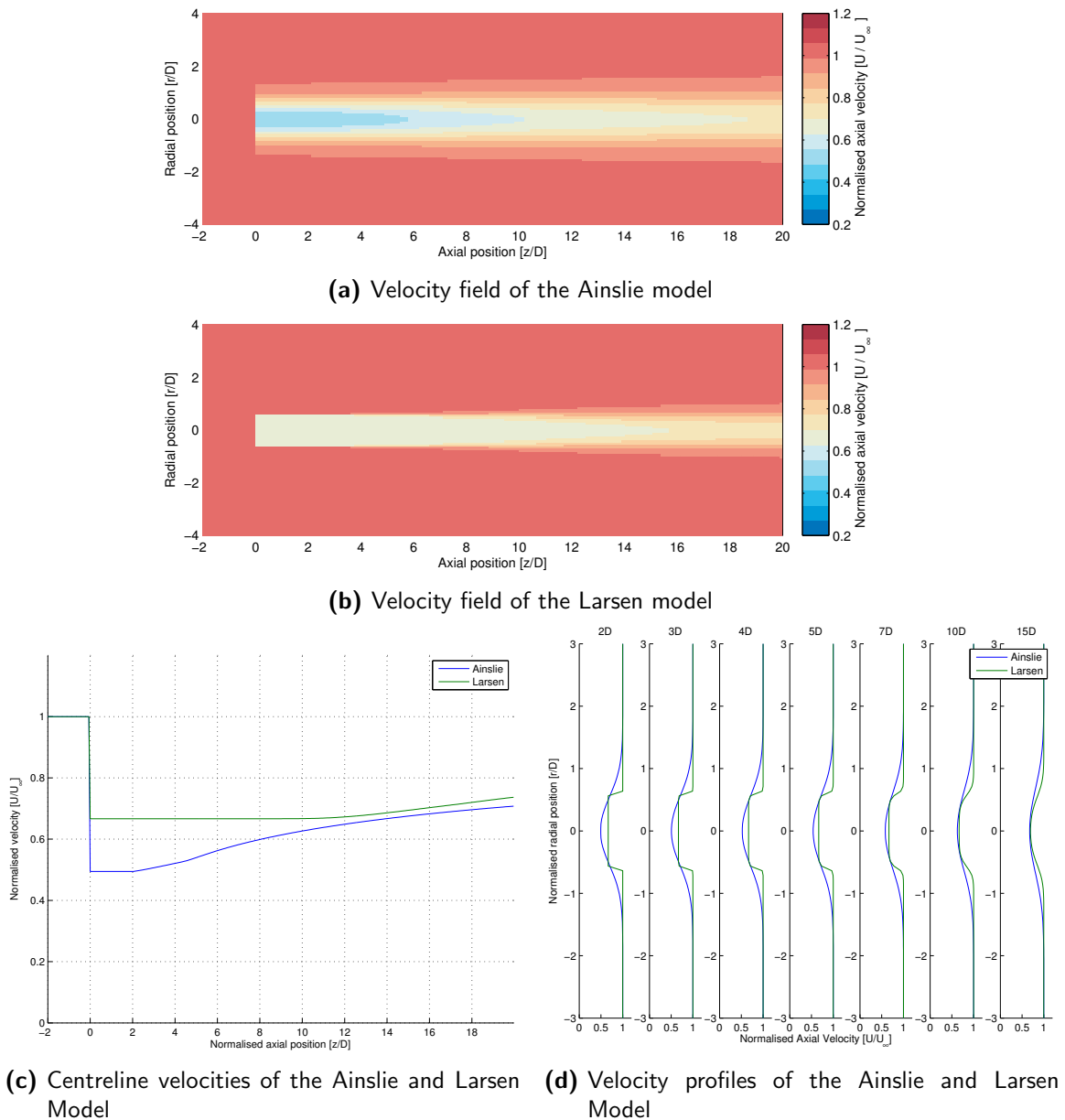
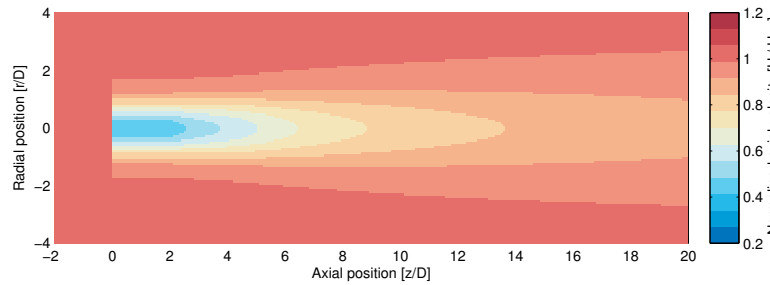


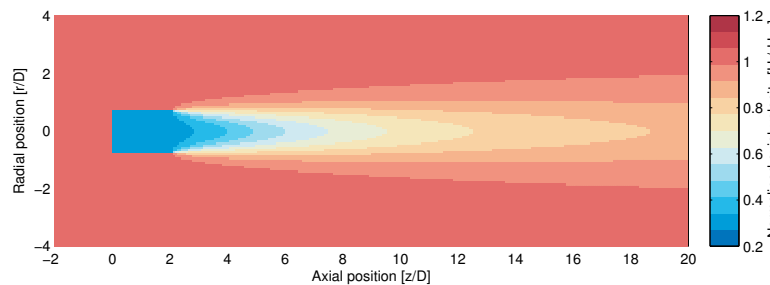
Figure 6.7: Results of a Ainslie-Larsen comparison with $C_T = 5/9$ and $TI = 0\%$

Figure 6.8 shows a comparison at a high turbulence level ($TI = 21\%$). The atmospheric turbulence seems to dominate the shear stresses, since both model shows a similar shape in the recovery of the wake centreline. The initial deficit is more similar compared to the zero turbulence case. Note that the initial near-wake model of Ainslie takes into account atmospheric turbulence, whereas the Larsen near-wake model assumes laminar flow. The Larsen model tends to be a little bit more conservative with respect to wake recovery in this case.

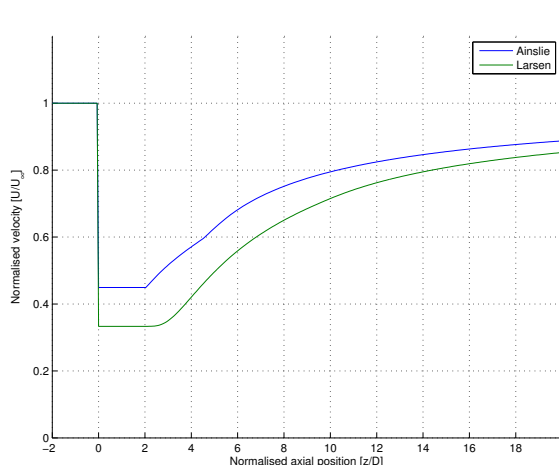
The comparison has shown that the Ainslie and Larsen models converge to relatively the same solution when low values of C_T are used. The effect of atmospheric turbulence



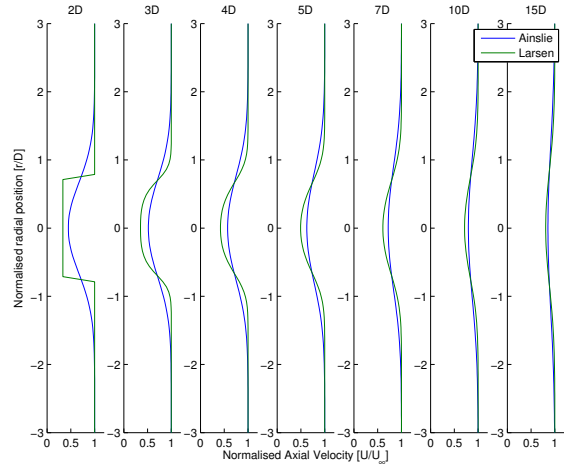
(a) Velocity field of the Ainslie model



(b) Velocity field of the Larsen model



(c) Centreline velocities of the Ainslie and Larsen Model



(d) Velocity profiles of the Ainslie and Larsen Model

Figure 6.8: Results of a Ainslie-Larsen comparison with $C_T = 8/9$ and $TI = 21\%$

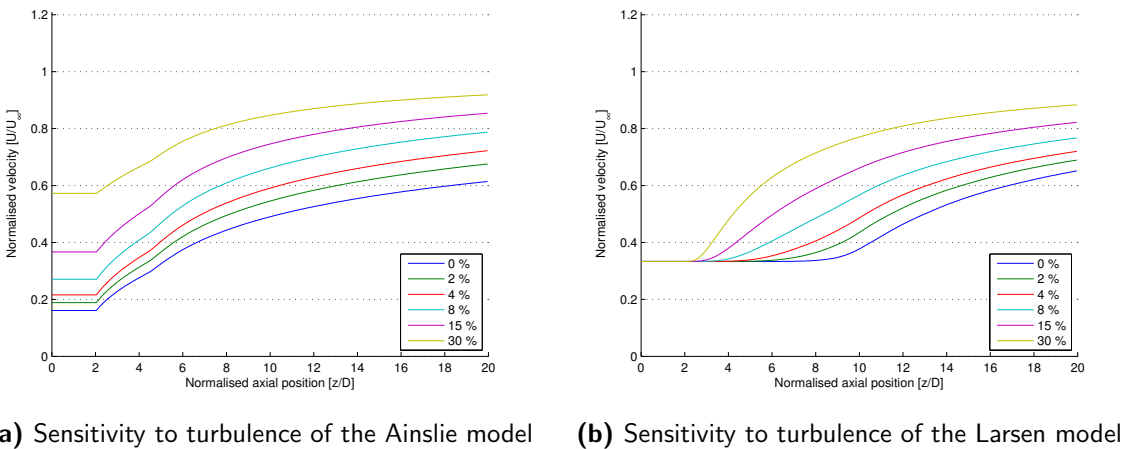
is less straightforward, but it seems to dominate the viscous stresses in the wake. High turbulence has a positive effect on wake recovery, which is to be expected and both models show a similar shape in the centreline velocities.

6.4.2 Sensitivity to Turbulence of the Ainslie and Larsen Models

The difference in centreline velocities between the Ainslie and Larsen model is further studied with respect to the atmospheric turbulence. The results are shown in figure 6.9, where centreline velocities of various value for TI are plotted. On the left, the results from

6.5 Verification of the Larsen Implementation by Comparison with Literature

the Ainslie model are shown and the right graph shows results from the Larsen model. Both graphs show a positive trend in wake recovery with respect to atmospheric turbulence, which is to be expected. A few other observations can be made. The Larsen model shows a delay in recovery in relation to atmospheric turbulence, which is not observed in the Ainslie model. This can be an effect of the different filter functions applied to the determination of the EV-term. The graphs also show that the near-wake Ainslie model is very sensitive to the atmospheric turbulence, resulting in an initial deficit difference of 0.4 in 30% turbulence intensity with respect to laminar flow. Finally, the spread of wake velocities at $20D$ of the Ainslie model is higher with respect to Larsen, thus making the Ainslie model more sensitive to turbulence with respect to Larsen.



(a) Sensitivity to turbulence of the Ainslie model (b) Sensitivity to turbulence of the Larsen model

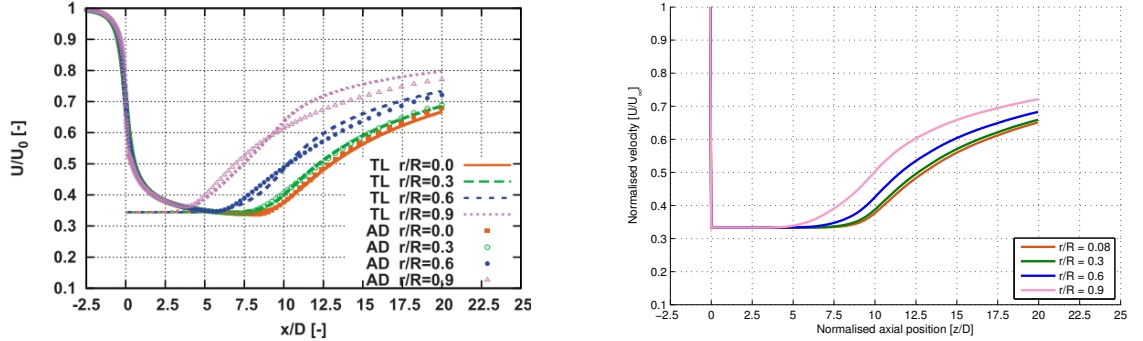
Figure 6.9: Centreline velocities for the Ainslie model (left) and the Larsen model (right) for $C_T = 8/9$ and various values for TI

6.5 Verification of the Larsen Implementation by Comparison with Literature

The Larsen EV-model was implemented exactly as described in Madsen et al. [37]. Madsen provided an extended validation of the model in his report, which includes velocity plots for laminar and turbulent inflow. These graphs can be used to verify the implemented model.

Figure 6.10a shows velocities at various radial positions along the centreline from Madsen's calibrated DWM model. Results are shown from the thin-shear layer (TL)¹ model with an actuator streamtube momentum near-wake model and results from an actuator disc placed in a CFD model (AD). Madsen used laminar inflow conditions ($TI = 0\%$). Figure 6.10b shows the same velocities from the implemented Larsen EV model with the same streamtube momentum model. The results are in reasonable to good agreement, where the implemented Larsen model is slightly more conservative in wake recovery. It should be noted, that Madsen includes wake meandering and turbine added turbulence in the model, which is not included in the implemented model. A slight difference is thus expected.

¹Madsen referred to the EV model as the thin-shear layer (TL) model.

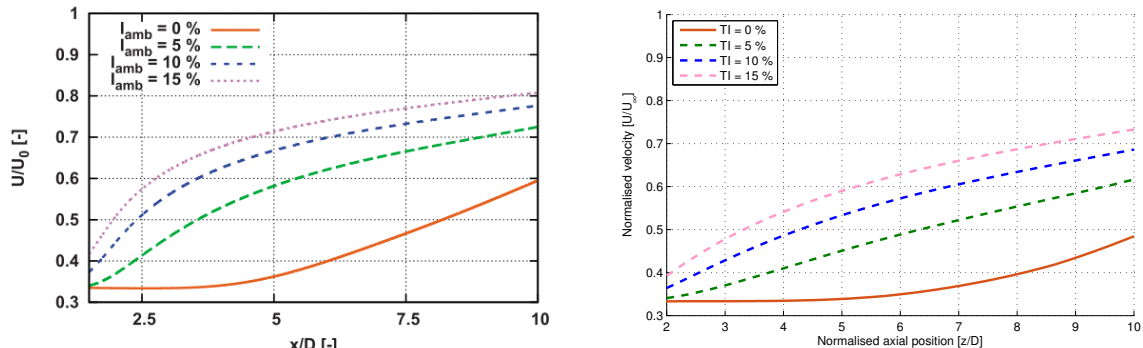


(a) Comparison of an actuator disk combined with CFD and the thin shear layer (TL) simulations by Madsen et al. [37]

(b) Results of the implemented streamtube-Larsen model

Figure 6.10: A comparison of results by Madsen et al. [37] (left) and the implemented model (right) with a uniformly loaded actuator disc of $C_T = 8/9$ in laminar flow

Figure 6.11 shows the influence of turbulence on wake recovery at a position of $r/R = 0.8$. Madsen used a BEM model to determine the near-wake and modelled a NEG Micon NM80 rotor operating at $8m/s$. The orange line, representing zero turbulence does not correspond with figure 6.10a and shows a much higher velocity at $10D$ and this difference is attributed to the change from actuator disk model to the BEM model. Figure 6.11b shows results from the implemented model with a uniformly loaded actuator operating at $C_T = 8/9$. The implemented model shows a more conservative recovery, which could be explained by the difference in near-wake modelling or a slightly different value for C_T .



(a) Results from [37], where a BEM near-wake model is used modelling the initial deficit of the NM80 wind turbine in $U_\infty = 8m/s$

(b) Results from the streamtube-Larsen model, using a uniformly loaded actuator with $C_T = 8/9$

Figure 6.11: Comparison of the influence of ambient turbulence on the development of the axial velocity deficit downstream at $r/R = 0.8$

Finally, figure 6.12 shows a comparison of wake profiles from simulation results provided in Keck et al. [28]. The left picture shows a comparison of a CFD actuator line model and the “standard DWM model” as referenced to by Keck et al. The values for k_{amb} and k_2 that Keck provided for the “standard” model (see table 6.1) are substituted in the implemented model to create figure 6.12b. The results are in good agreement, which proves that the

numerical implementation of the EV-model is providing results as expected.

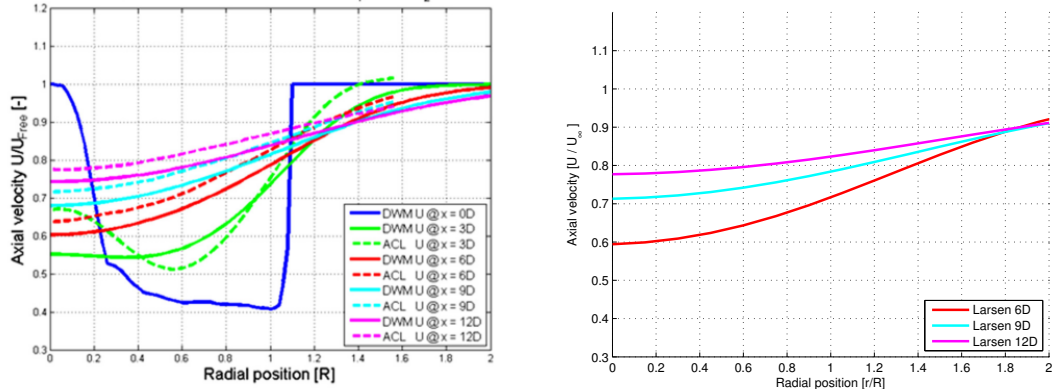


Figure 6.12: Comparison of axial velocities at various radial positions with $U_\infty = 10 \text{ m/s}$ and $TI = 6\%$. The figure left shows a comparison by Keck et al. [28] between the DWM and an actuator line CFD model. The right graph shows results from the discussed streamtube-Larsen implementation.

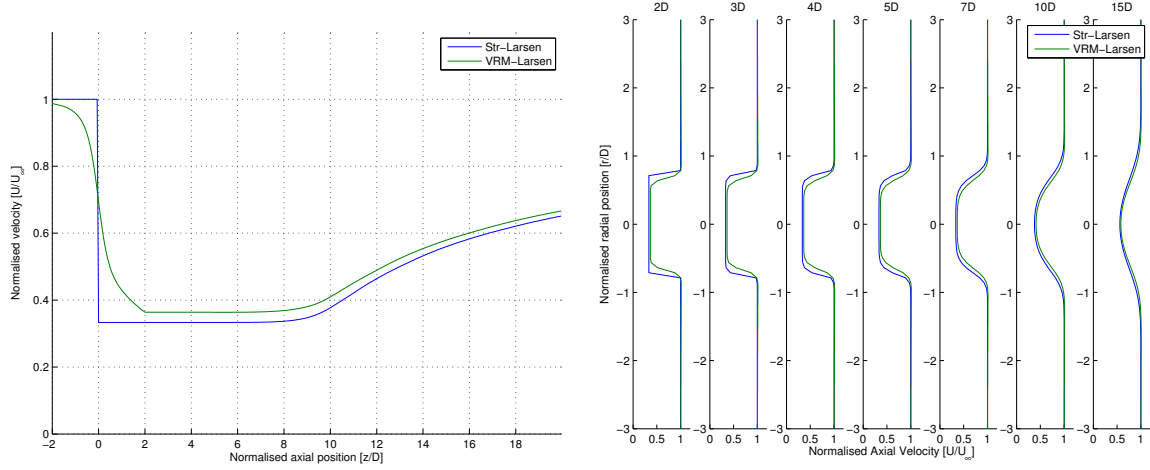
6.6 Results of a Single Wake VRM-Larsen Coupling

The VRM-Larsen coupled model is applied to a single wind turbine with variable thrust and turbulence intensities. The results are compared against the standard Larsen wake deficit model. The Ainslie near-wake model is not included in this comparison. The sensitivity towards atmospheric turbulence in the near-wake is significant, which makes it undesirable to compare it with a inviscid near-wake model. The Larsen model was designed with keeping in mind different near-wake models, while the Ainslie model was published as a stand-alone model. Finally, the Larsen far-wake model has an ongoing development, which makes a theoretical improvement more valuable. The current implementation is the calibrated and discussed version by Madsen et al. [37].

Figures 6.14 and 6.13 show centreline velocities and wake profiles for a turbine in 0% atmospheric turbulence with a thrust coefficient of $C_T = 8/9$ and $C_T = 5/9$ respectively. The same thrust coefficients are applied to a turbine in a velocity field with 25% turbulence intensity and are shown in figures 6.15 and 6.16. Velocity field plots were also created and are shown in Appendix C.

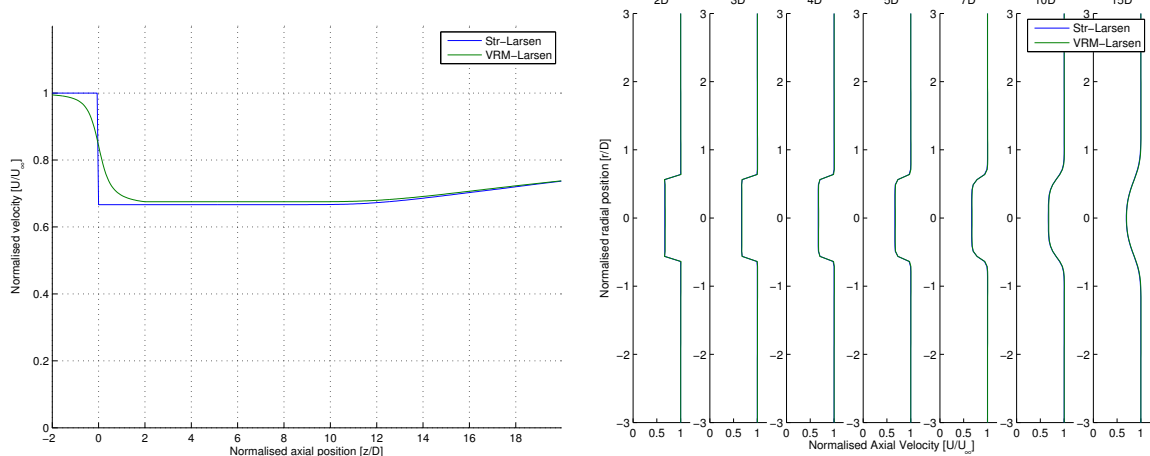
In general, the results of both simulations are close, which is a positive result. The VRM-Larsen model performs similar to the reference Larsen model, while the near-wake is based on much more physical properties and describes a complete field. This is an advantage over the reference Larsen model, which only describes a deficit after a $2D$ distance.

Focussing on the results of the laminar cases in figures 6.13 and 6.14, it can be concluded that the difference in the models is diverging with higher C_T . Figure 6.13b shows that



(a) Centreline velocities of the VRM-Larsen and Larsen models (b) Velocity profiles of the VRM-Larsen and Larsen models

Figure 6.13: Simulation results of the VRM-Larsen and BEM-Larsen wake models with $C_T = 8/9$ and $TI = 0\%$

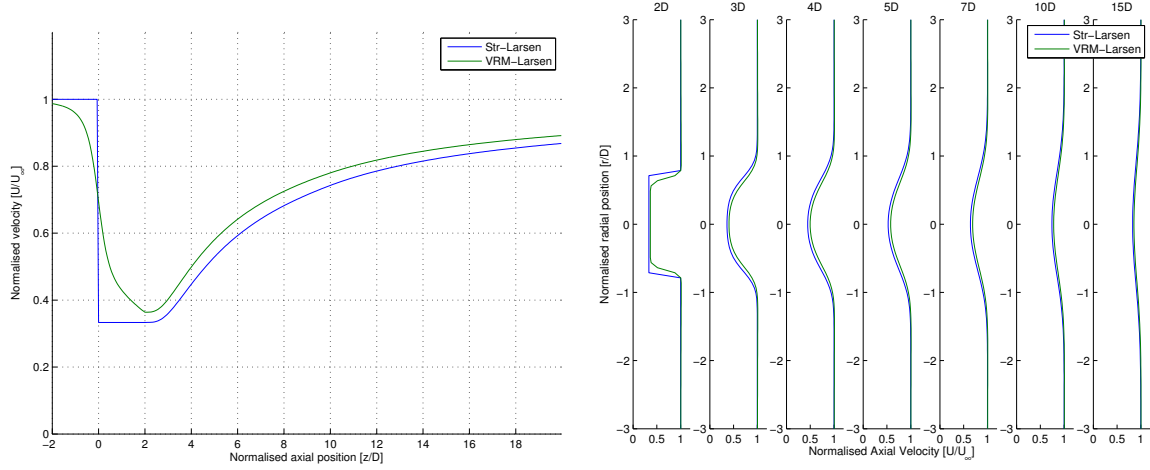


(a) Centreline velocities of the VRM-Larsen and Larsen models (b) Velocity profiles of the VRM-Larsen and Larsen models

Figure 6.14: Simulation results of the VRM-Larsen and BEM-Larsen wake models with $C_T = 5/9$ and $TI = 0\%$

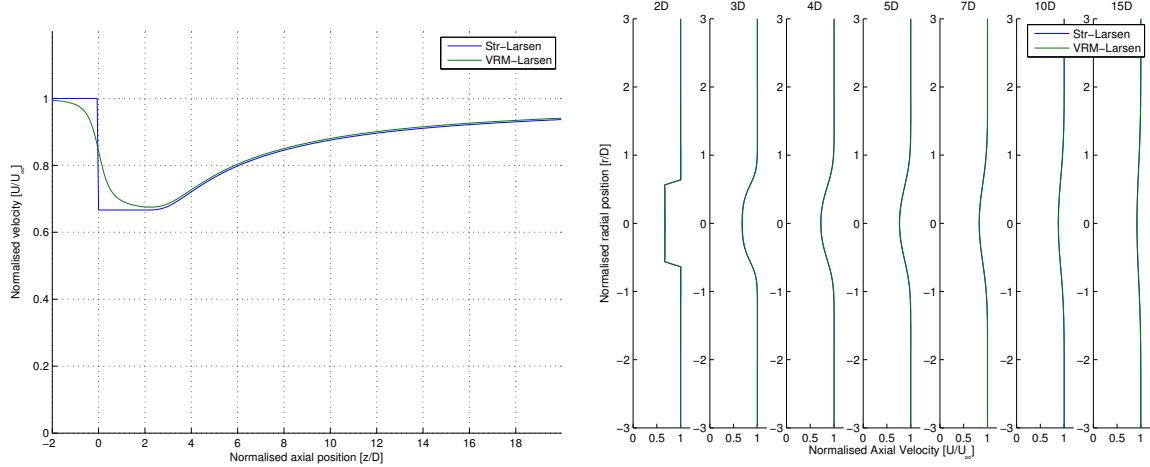
the initial wake profile has only a slight influence on the shape of the wake far down-wake. There is however a small, but significant difference in centreline velocity far down-wake.

The simulations with a high turbulence intensity displayed in figures 6.15 and 6.16 follow the previous trend. The results for a low C_T value are very similar in the near-wake, while the simulations with a relatively high C_T value have a slight but not negligible velocity difference. The profile shape is however more similar compared with the zero turbulence case. This coincides with the previous findings in section 6.4.1 and confirms that the Eddy Viscosity is the main driver for the profile shape in the far-wake.



(a) Centreline velocities of the VRM-Larsen and Larsen models (b) Velocity profiles of the VRM-Larsen and Larsen models

Figure 6.15: Simulation results of the VRM-Larsen and BEM-Larsen wake models with $C_T = 8/9$ and $TI = 25\%$



(a) Centreline velocities of the VRM-Larsen and Larsen models (b) Velocity profiles of the VRM-Larsen and Larsen models

Figure 6.16: Simulation results of the VRM-Larsen and BEM-Larsen wake models with $C_T = 5/9$ and $TI = 25\%$

6.7 Conclusions from the VRM-Larsen Results

The Ainslie and Larsen models are both based on the concept of Eddy Viscosity and show a similar shape in far-wake development. However, the Larsen model is found to be a better candidate for coupling with the VRM, since it is calibrated with traceable modern wind tunnel data and the model supports various far-wake phenomena prediction modules as part of the DWM model.

The VRM-Larsen and Streamtube-Larsen models are mutually compared. The VRM-

Larsen model predicts wake development on every axial position in the near-wake, whereas the streamtube-Larsen model is limited to an initial deficit assumed at $2D$. The VRM-Larsen shows a non-negligible diversion in far-wake development in high thrust cases from the results of the streamtube-Larsen model. A benchmarking case with a Large Eddy Simulation code is set up to further study this difference in far-wake development from which the results are shown in the following chapter.

Chapter 7

Validation of the VRM-Larsen Model with an LES CFD Model

The derived VRM-Larsen model and the original Larsen model are compared against a Large Eddy Simulation (LES) model. LES provides a good way to validate the VRM-Larsen model, since there is more control over the input parameters in LES, which makes it fair for a comparison. A description of the LES code is provided in section 7.1. Results of a single wake case are discussed in section 7.2 and the results of a two-turbine fully immersed wake case is discussed in section 7.4.

7.1 Description of the LES CFD Model

The LES code used for validation is the Energy Conserving Navier-Stokes (ECNS) code developed by the Energy research Centre of the Netherlands (ECN). An extended description of the code can be found in Mehta et al. [40], but a brief overview is presented in this section.

In the current simulation, the incompressible N-S equations are discretised on a uniform and staggered Cartesian grid with a finite-volume approach. The ECNS code minimises numerical dissipation, which in wind farm CFD modelling is known to lead to an underestimate of wake deficit. A fourth order Runge-Kutta method is used to prevent numerical dissipation through temporal integration. Subgrid scale dissipation is explicitly modelled with the use of a subgrid model. The model used in this simulation is the Smagorinsky's Eddy-Viscosity Model (SM) [51] with a Smagorinsky constant of $C_S = 0.15$.

The inflow boundary is assigned a Dirichlet boundary condition with a uniform inflow. In the current form, the model is only compatible with uniform conditions and atmospheric turbulence is not yet implemented. The other walls are considered as outflow boundaries, only to prohibit backflow.

The turbine is modelled with an actuator disc, where the total force is calculated with:

$$T = \frac{1}{2} \rho C_T A U^2 \quad (7.1)$$

Where, ρ is the air density, taken as 1.225, A the area of the disk, C_T the thrust coefficient and U the wind velocity. For the single wake case and the upstream turbine in the double turbine case, the undisturbed wind speed U_∞ is taken. For the second turbine, an area weighted average of the local velocities are taken. The calculated force is then discretised over the volumes within the location of the disk. The circular disc on the Cartesian grid leads to some fluctuations, which are discussed in section 7.3.

The code is run on the Delft University of Technology *Beowulf* cluster, which consists of different nodes with a mix of Intel® Xeon® and AMD Opteron™ processors [21].

7.2 Comparison of the VRM-Larsen Model with an LES Single Turbine Case

Section 6.6 shows that the VRM-Larsen differs most from the original Larsen model with a turbine operating at high thrust in laminar flow. This case was therefore selected for a comparison with LES. An overview of all parameters of the simulation are presented in table 7.1. The maximum length of the domain (12D in z-direction) was limited by the memory available from the computational cluster. It was found, that a longer wake field resulted in a memory problem when setting up the pressure solver. Note that by expanding the grid in one direction, the required extra grid volumes increase with a cubed relation.

Table 7.1: Parameters used in the single and double turbine LES calculations

Parameter	Single turbine case	Two-turbine case
Domain (x,y,z)	8D, 8D, 12D	8D, 8D, 17D
Grid volumes	80, 80, 120	80, 80, 170
Axial position of Actuator	4D	3D and 10D
Thrust coefficient	8/9	8/9 (both)
Uniform wind velocity	10m/s	10m/s
Air density	1.225kg/m ³	1.225kg/m ³
Molecular viscosity	18.1E - 6Ns/m ²	18.1E - 6Ns/m ²

Figure 7.1 shows axial velocities down-wake for different radials. Figure 7.1a on the left shows velocities along the centreline ($r/R = 0$) and figure 7.1b on the right shows velocities along the relative end of the rotor ($r/R = 0.8$). The VRM-Larsen model matches the LES closely in the near-wake region in both graphs. A good resemblance is also observed in the rest of the wake for the centreline velocities, while a diversion seems to grow from 6D along the $r/R = 0.8$ radial. A small dip in velocity is observed in figure 7.1b before 2D. This result is most likely due to strong vortex interaction at this position in the near-wake. Figure 7.2 shows the position of vortex rings from which the velocity field was determined. A cluster of vortex rings can be observed around 2D, which locally

7.2 Comparison of the VRM-Larsen Model with an LES Single Turbine Case

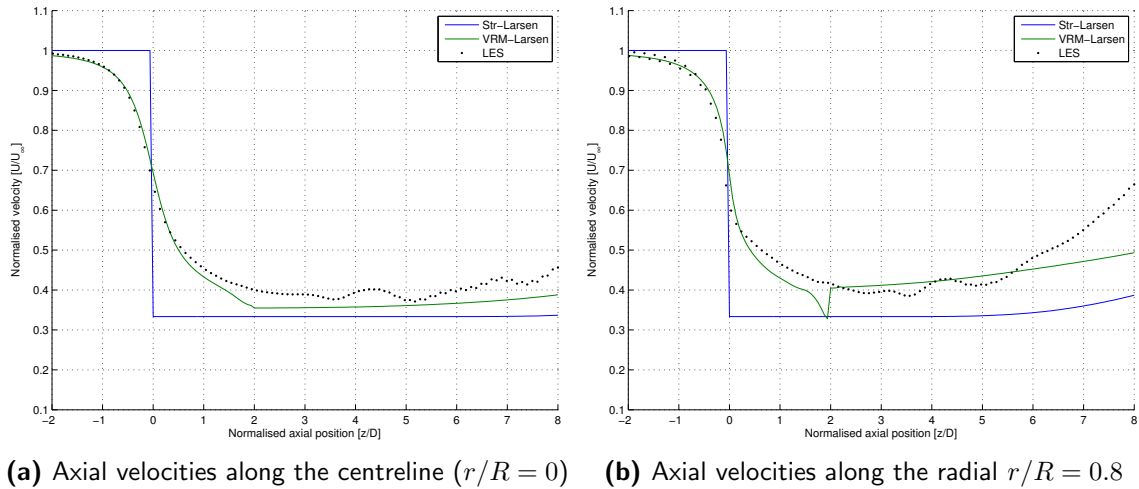


Figure 7.1: Axial velocities in the down-wake direction from the Larsen, VRM-Larsen and LES computations for a single turbine with $C_T = 8/9$ and $TI = 0\%$

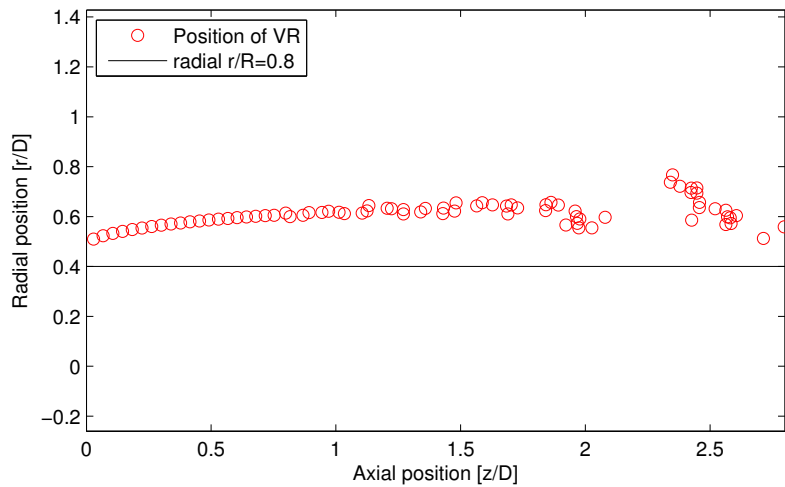


Figure 7.2: Vortex ring positions in the near-wake from the VRM-Larsen model showing a cluster of vortex rings around $2D$ causing a high local deficit along the radial $r/R = 0.8$

increases the induced velocities at the $r/R = 0.8$ radial. Time-averaging of the near-wake as discussed in 4.2, would most likely eliminate this phenomenon.

The original Larsen model based on a streamtube momentum near-wake implementation at $2D$, shows a slightly poorer fit with LES along the centreline as compared with the VRM-Larsen model, which is due to the overestimated wake deficit in the near-wake. A higher deviation from LES is observed at the radial $r/R = 0.8$, which is the result of using an initial hat profile in the near-wake. Wake recovery along the centreline is slow compared to the other models. This is also observed in figure 7.4a, which gives a clearer picture of the wake recovering process. The build-up of turbulence in the wake is slower, since the initial shear layer is very thin due to the initial hat profile.

Small fluctuations are observed in front of the rotor disc in the LES result along the $r/R = 0.8$ radial. These fluctuations are further discussed in section 7.3.

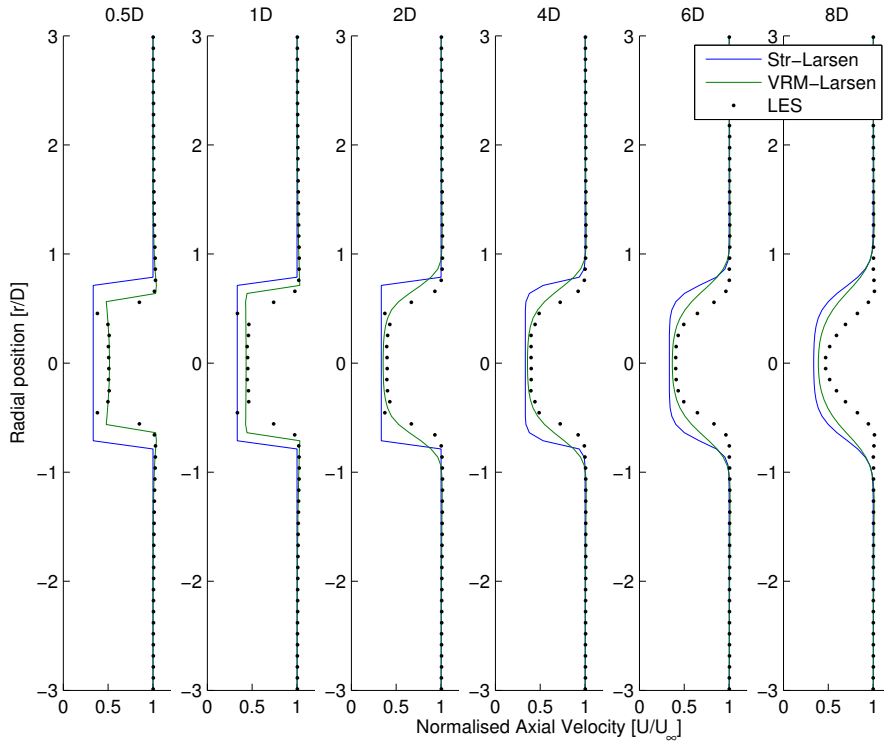


Figure 7.3: Wake profiles at various down-wake positions from the Larsen, VRM-Larsen and LES computations for a single turbine with $C_T = 8/9$ and $TI = 0\%$

Velocity profiles at various positions down-wake are displayed in figure 7.3, which shows the wake expansion from the simulations. Similar to the results in figure 7.1, the VRM-Larsen model has a closer fit to LES compared with the original Larsen model. The reference Larsen models seem to overpredict the initial wake expansion in relation to LES, while the VRM-Larsen model shows a much closer initial fit. However, both models overpredict the wake expansion further down-wake. The LES shows wake contraction at the end of the wake ($8D$). Wake contraction is expected at some point, since the wake is recovering, but seems unnatural at this position. The result from the LES simulation shows odd behaviour at the edge of the shear layer in the near-wake and predicts a very large deficit at this position. This can be seen in the first three graphs of figure 7.3.

Velocity fields of the axial velocity of all simulations are displayed in figure 7.4c. The VRM-Larsen model captures the deceleration in front of the rotor in accordance with the LES results. The reference Larsen model has a very slow build-up of the shear-layer, since there is none present in the near-wake model. Figure 7.4c clearly shows the odd behaviour at the edge of the rotor disc, resulting in fluctuations in front of the rotor disc and a relatively high velocity deficit immediately after the disc. This is due to the implementation of a round actuator disc on a Cartesian grid [47] with the immersed surface method and is explained in more detail in the next section.

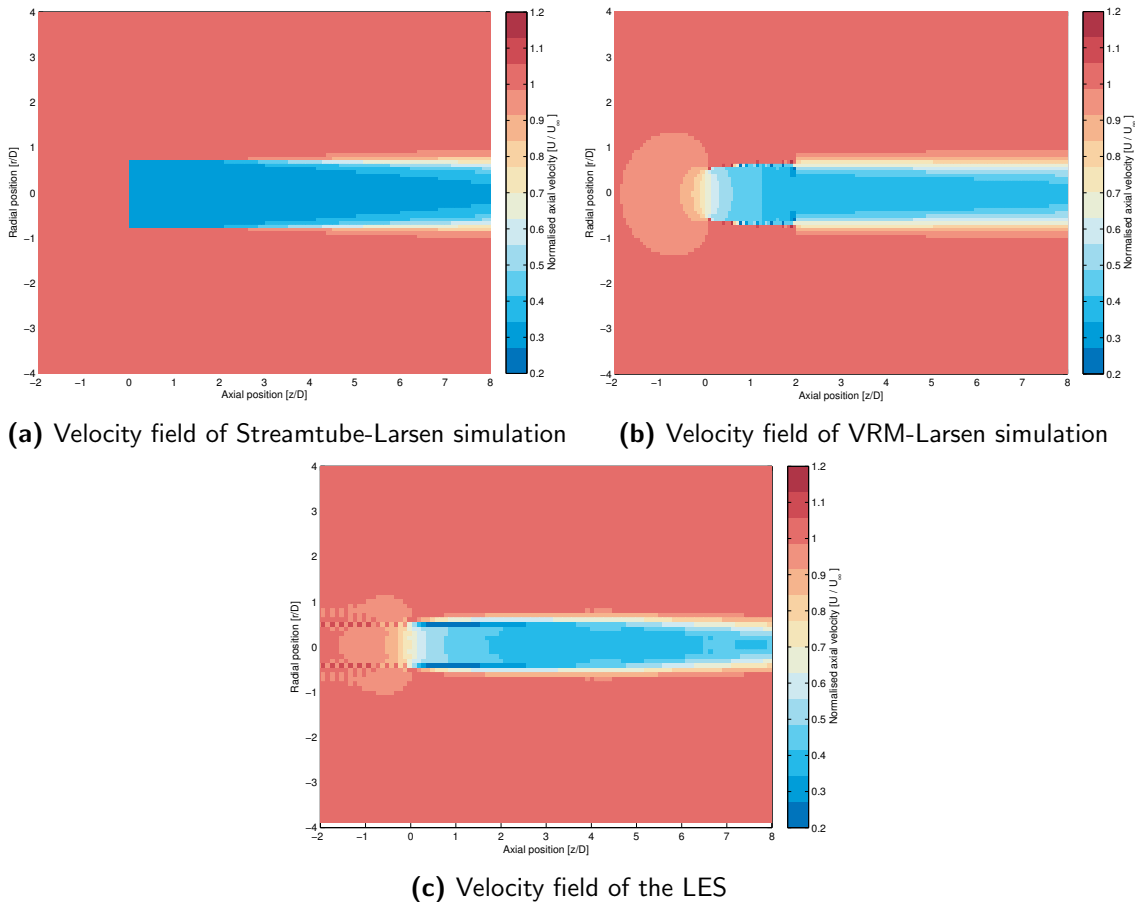


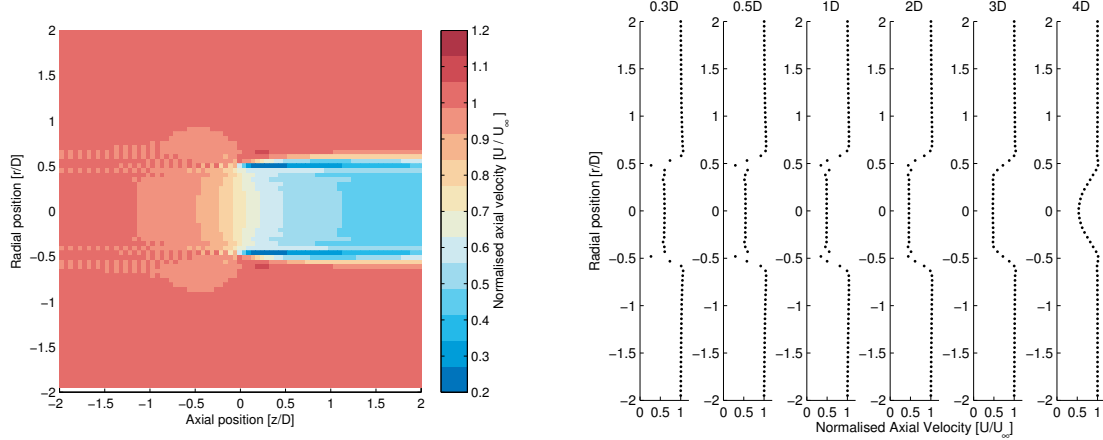
Figure 7.4: Axial velocity fields of the Streamtube-Larsen, VRM-Larsen and LES results

7.3 Increased Resolution

The LES results show some odd behaviour in front of and after the actuator disc. This edge phenomenon, which is also observed in Sanderse [47], is most likely the result of a mathematical error from implementing a circular actuator on a squared Cartesian grid. To further investigate the issue, the simulation was redone on a smaller domain but similar amount of grid points, thus effectively increasing the resolution of the grid. The results from this simulation are shown in figure 7.5. The domain was halved with respect to the simulation done in section 7.2 in every direction, effectively doubling the resolution.

The results show, that the error is still present, which is to be expected, since the grid is still Cartesian. It is also observed, that the high deficit is still present on only one array of grid volumes around the actuator. An even higher resolution would limit the effect of the error, but not eliminate it.

A method to solve this issue is to implement a Gaussian distribution of the force at the edge of the actuator. This, way, the force is gently applied over a number of volumes until it reaches the maximum force value. This is solution is not yet implemented in the ECNS code which uses the immersed surface method.



(a) Velocity field of the LES results on a grid with increased resolution (b) Velocity profiles of LES results on a grid with increased resolution

(c) Contourslices of the LES results on a grid with increased resolution showing the mathematical error on the edge of the actuator disc. X- Y- and Z-axis are in number of grid volumes

Figure 7.5: Results from the LES actuator disc model where the effective resolution of the grid is doubled

7.4 Comparison of the VRM-Larsen Model with a Two-Turbine LES Case

The LES code is also used to model the wake velocities from two turbines. In this case, the second turbine is fully immersed in the wake of the first turbine at a spacing of $7D$. Similar to the single turbine LES case, the inflow velocity field is laminar. Both turbines operate at $C_T = 8/9$, however the total thrust of the second turbine is calculated with:

$$T_2 = \frac{1}{2} \rho A C_T \bar{U}_2^2 \quad (7.2)$$

Here, \bar{U}_2 is the local disc area weighted average of the axial velocity. Thus, axial velocities taken at the position of the disc and averaged with:

$$\bar{U}_2 = \frac{\sum_{i=0}^R U(i) (\pi r(i+1)^2 - \pi r(i)^2)}{\pi R^2} \quad (7.3)$$

Equation 7.3 is used every timestep, thus calculating the thrust of the second turbine dynamically. Ultimately, this results in an effective induction factor of 0.29, measured between $3D$ upfront and $3D$ aft of the actuator disc. Other parameters of the two-turbine case are displayed in table 7.1.

7.4.1 Multiple Wake Modelling in the Streamtube-Larsen Model

In the streamtube-Larsen model, a multiple wake case is treated in the following way. From the upwind rotor, the far-wake axial wind velocity at the location of the second turbine is determined. These velocities are used as an input to the streamtube momentum model discussed in section 6.1. A uniformly loaded actuator disc is used with a constant thrust coefficient of $C_T = 8/9$. This results in a local induction factor of $a = 1/3$, which is equal for every streamtube. Outside the wake, determined with equation 6.6, the velocity field determined from the upstream far-wake simulation is used. This forms the initial input velocity profile to the downstream far-wake model.

7.4.2 Multiple Wake Modelling in the VRM-Larsen Model

In the VRM-Larsen model, the far-wake of the upwind turbine is calculated until $2D$ after the position of the downwind turbine. A disc area weighted average of the axial velocity is determined at the position of the second actuator disc with equation 7.3, similar to LES. This average velocity at the actuator disc is used to determine the strength of the released vortex rings from the down-wake turbine in equation 3.10. A fixed value for C_T is used, similar to the streamtube-Larsen model. The near-wake of the downwind turbine is then modelled with the vortex ring model.

As an initial velocity field, the results from the upwind turbine are used from $-2D$ to $2D$ relative to the position of the downwind turbine. The induced velocities from the vortex rings are then superimposed on this velocity field, as schematically displayed in figure 7.6. The result of this iteration is deceleration of the flow in front of the downwind actuator which is much more in accordance with known measurements.

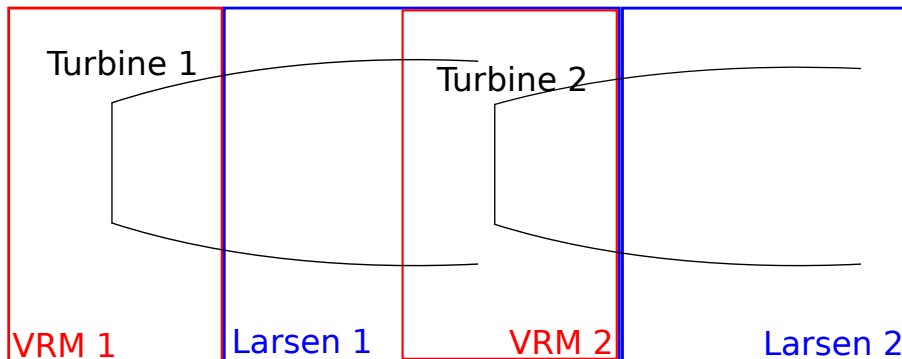


Figure 7.6: Schematic overview of a multiple wake approach in the VRM-Larsen model

7.4.3 Results of the Multiple Wake Simulations with LES

The results of the multiple wake simulation are displayed in figure 7.7, where axial velocities are plotted down-wake along a constant radial position for all simulations. Velocity fields of the simulations are displayed in Appendix D. The first actuator is located at $z = 3D$ and the second actuator at $z = 10D$.

Figure 7.7a displays velocities close to the centreline of the wake. Similar to the results of the single wake simulation, the VRM-Larsen model is in good agreement with LES in the wake of the first turbine. The VRM-Larsen model is not as consistent in the wake of the second turbine, overpredicting the initial wake deficit and the rate of recovery. The difference in initial deficit could be the result of the dynamically calculated thrust of the second turbine in the LES, whereas this thrust is constant in the VRM and streamtube near-wake models. The LES results show some fluctuation in the wake of the second turbine, which is most likely due to the increase in turbulence.

Figure 7.7b displays velocities towards the edge of the actuator disc. Here, the VRM-Larsen model differs slightly in the wake of the first turbine compared to LES, but is in very good agreement in the wake of the second turbine. The streamtube-Larsen model overpredicts the deficit of the second turbine, since the wake of the first turbine did not recover with the same respect as the VRM-Larsen model.

Finally, figure 7.7c shows the axial velocities outside of the wake shear layer. Both the VRM-Larsen and LES models capture the acceleration of the flow outside the wake. In the far-wake of the second turbine, the VRM-Larsen follows the trend of the reference Larsen model with a slight decrease in velocity, whereas the LES results are constant in this region.

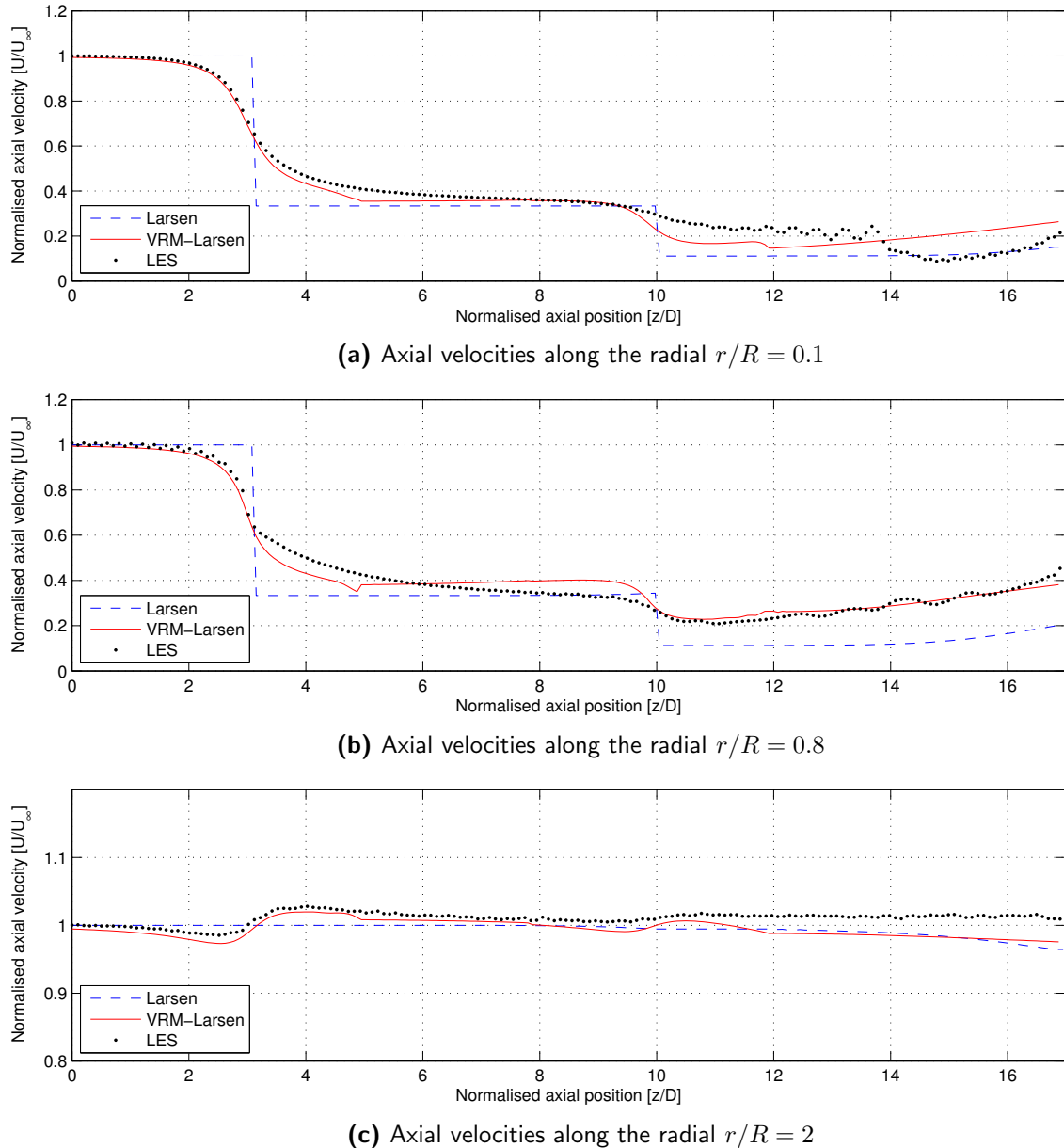


Figure 7.7: Axial velocities in the down-wake direction from the Larsen, VRM-Larsen and LES computations for two turbines with $C_T = 8/9$ and $TI = 0\%$

7.5 General Conclusions from the LES Comparison

The VRM-Larsen model is in reasonable to good agreement with the LES calculations and performs closer to LES with respect to the reference Larsen model. The VRM-Larsen model also captures the deceleration of the flow through the actuator disc, which is very close to the LES results, whereas the streamtube model only presents a fixed velocity at $2D$. An earlier transition from the near-wake VRM to the far-wake Larsen model as compared to the currently used distance of $2D$ down-wake could potentially improve the

VRM-Larsen results.

This LES comparison is a positive result for the VRM-Larsen model, where it approaches the LES calculations in a fraction of its computational time. As a reference, the VRM-Larsen model took roughly 30 minutes to calculate the deficit, whereas the LES model had run for multiple weeks in the double turbine case.

Chapter 8

Power Predictions Compared with Data from the Horns Rev Wind Farm

The two-turbine LES case discussed in section 7.4 shows that an improvement is observed in wake deficit prediction by using the VRM-Larsen model over the streamtube-Larsen model when compared to the LES multiple turbine benchmarking case. This encouraged for a study to investigate the behaviour of the model in an array of multiple turbines. Details of the wind farm and the selected case are discussed in section 8.1. The application of the Larsen models to calculate wind turbine power output is discussed in section 8.2 and the results of this simulation are compared with data found in literature in section 8.3.

8.1 The Horns Rev Wind Farm

Horns Rev is a wind farm located off the coast of Denmark, currently owned by Vattenfall (60%) and DONG Energy (40%). The wind farm consists of 80 Vestas V80 wind turbines, which gives a total capacity of 160 MW. The turbines are arranged in a square grid of 8 rows, where each row contains 10 turbines spaced at a distance of $7D$ as displayed in figure 8.1. Figure 8.2 shows a photograph of the wind farm where the wake of the wind turbine is visualized by fog.¹

Analysis on the wind farm supervisory control and data acquisition (SCADA) system, as well as the meteorological data from the wind farm met masts have been carried out by Méchali et al. [39] and Hansen et al. [18]. These published results provide a good test case for the VRM-Larsen model. The selected case is a fully immersed wake, with the mean

¹This picture (figure 8.2), credited to Christian Steiness, became instantaneously famous, since it is the only existing photograph to visually capture the wind turbine wake without artificial visualisation techniques. The display of fog in the wake is later attributed to very special atmospheric conditions, where warm humid air is up-drafted due to the rotation of the wake and mixes with the colder air above it, resulting in condensation.[19]

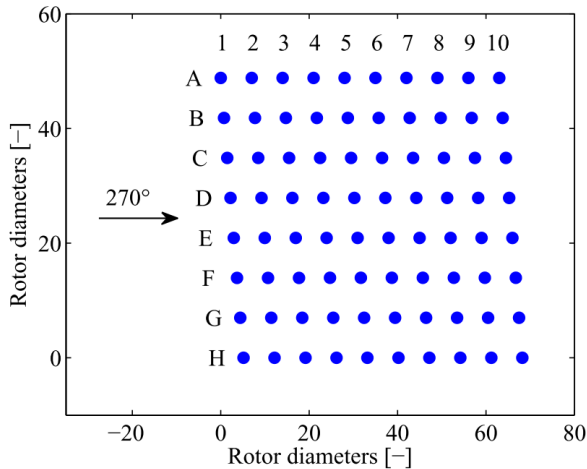


Figure 8.1: Turbine lay-out of the Horns Rev wind farm. Figure courtesy of Gaumond et al. [17]



Figure 8.2: Photograph of the Horns Rev wind farm showing wake effects visualised by local condensation. Photo by Steiness [52].

wind direction parallel to the wind turbine row. This refers to the ten turbines in row G in figure 8.1 with Westerly wind (270°) and Easterly wind (90°), both with a bin size of 5° . The SCADA data and met masts provide 10-minute average data of all relevant parameters.

8.2 Prediction of Power Output with the Larsen Models

The Streamtube-Larsen and VRM-Larsen are applied to the Horns Rev case in a similar way as the two-turbine LES case discussed in section 7.4. An overview of input parameters is displayed in table 8.1. The thrust coefficient was taken as $C_T = 0.805$, in accordance with the thrust curve found in Hansen et al. [18] and is assumed to be constant between 5 and $9m/s$. In the current case the power output of the turbines is also of interest. The power output of a turbine is determined from the definition of the power coefficient:

$$P_i = \frac{1}{2} \rho A C_P U_i^3 \quad (8.1)$$

Here, ρ is the air density and A is the rotor area. C_P is the power coefficient of the turbine. In the current simulation, an average power coefficient of $C_P = 0.41$ is taken for all turbines, taken from Jensen et al. [22]. The calculated power output of the turbines is normalised with the calculated power output of the first turbine, so the value taken for C_P is irrelevant in the end as long as all turbines operate at equal C_P . This assumption is made because in this case, $U_\infty < U_{rated}$. While the power coefficient decreases significantly above the rated wind speed, it is relatively constant between the cut-in speed and the rated wind speed. U_i represents the wind speed. For the first turbine, U_1 is taken as U_∞ . For the other turbines, U_i is determined by taking an area weighted velocity at the position of the rotor *before* the near-wake simulation of this rotor is run. This corresponds with the wind velocity at the rotor, if the rotor was not there.

Table 8.1: Parameters used in the Horns Rev wake simulation

Parameter	Value
Number of turbines	10
Spacing	$7D$
Thrust coefficient	0.805
Rotor diameter	80m
Uniform wind velocity	8m/s
Turbulence intensity	7%

8.3 Results of the Horns Rev Simulation and a Comparison with Literature

The resulting axial wake velocities from the simulation are displayed in figure 8.4. The VRM-Larsen models shows an increasing acceleration outside of the wake shear layer, which is not present in the streamtube-Larsen model. Velocities along the radial $r = 0$ of these fields are displayed in figure 8.3. In both models, the wake velocities converge to a regular repeating pattern after 3 turbines. The influence of the VRM on the wake of the upwind turbine is clear. The model captures the deceleration of the flow in front of the rotor, whereas the streamtube-Larsen model only carries information down-stream. In general, the wake velocities of the streamtube-Larsen model are lower with respect to the VRM-Larsen model due to the more conservative near-wake model, which is in accordance with the findings in section 6.6.

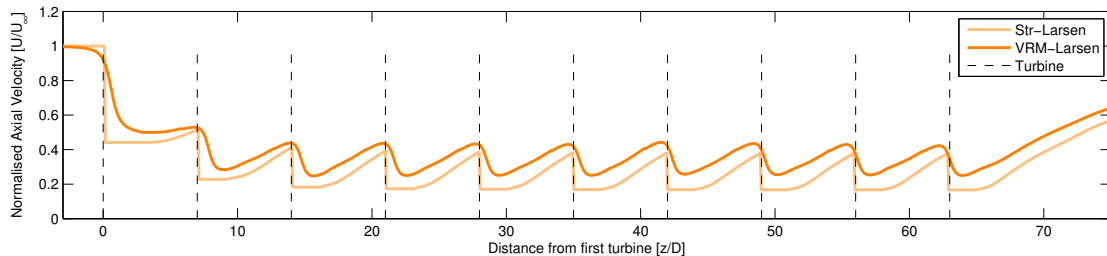
**Figure 8.3:** Axial velocities along the centreline of the Horns Rev case simulated with the streamtube-Larsen and VRM-Larsen models

Figure 8.5 shows the results of the power prediction simulations. Figure 8.5a on the left shows results compared with data from Gaumond et al. [17] and figure 8.5b displays results compared with data obtained by Méchali et al. [39]. In both graph, power output is normalised by dividing by the power production calculated for the first upwind wind turbine. A fairer comparison would be to compare absolute calculated power output, but this data is not provided in literature, most likely due to non-disclosure agreements. A number of observations can be made.

All models are underpredicting the power output of the downwind turbines when compared to the measurements, which could be explained by various reasons. The SCADA data is 10-minute averaged, which induces a high uncertainty in wind direction. Examples of fluctuating parameters are the wind speed exceeding 8m/s, wind direction diverging

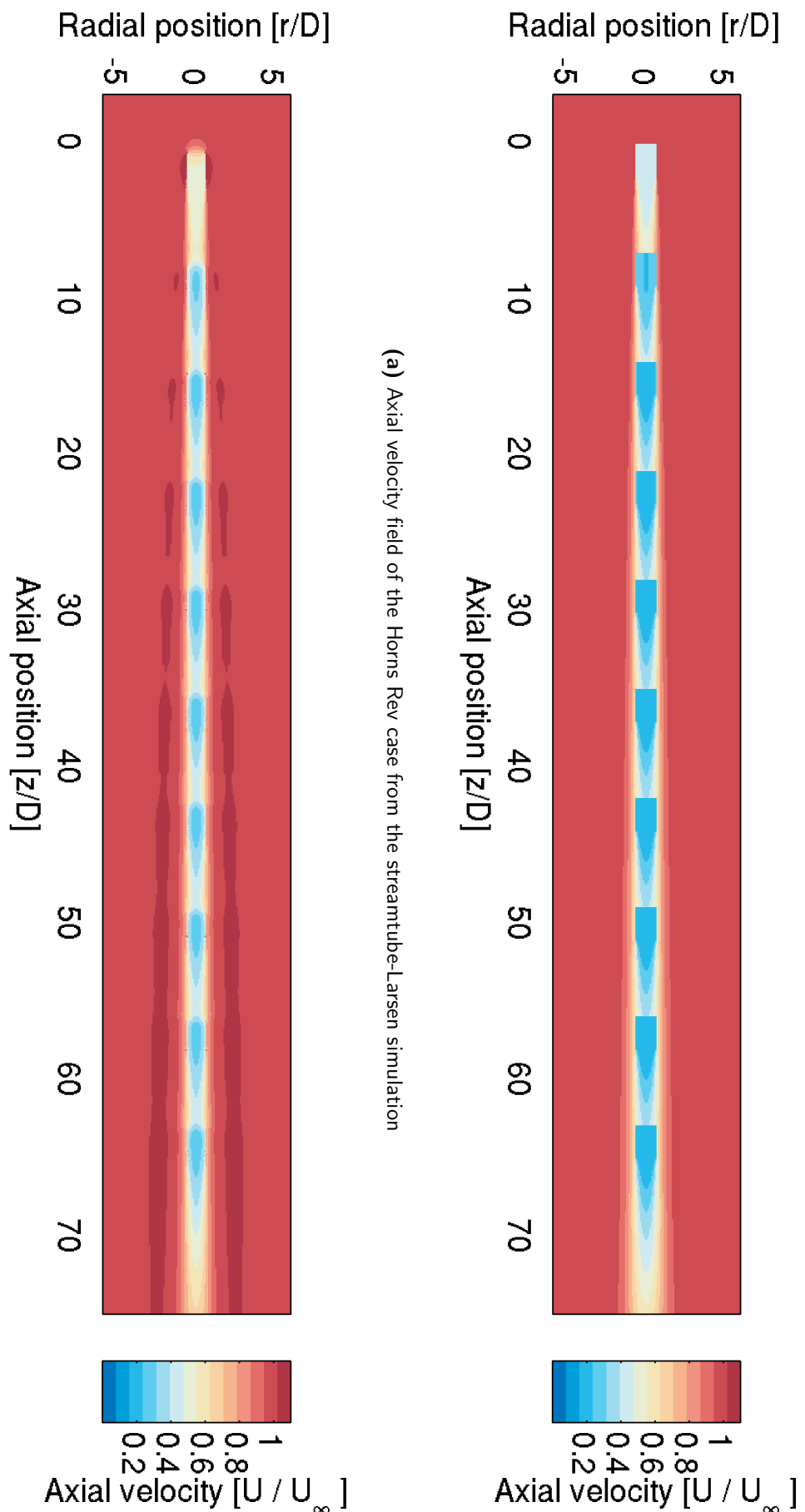
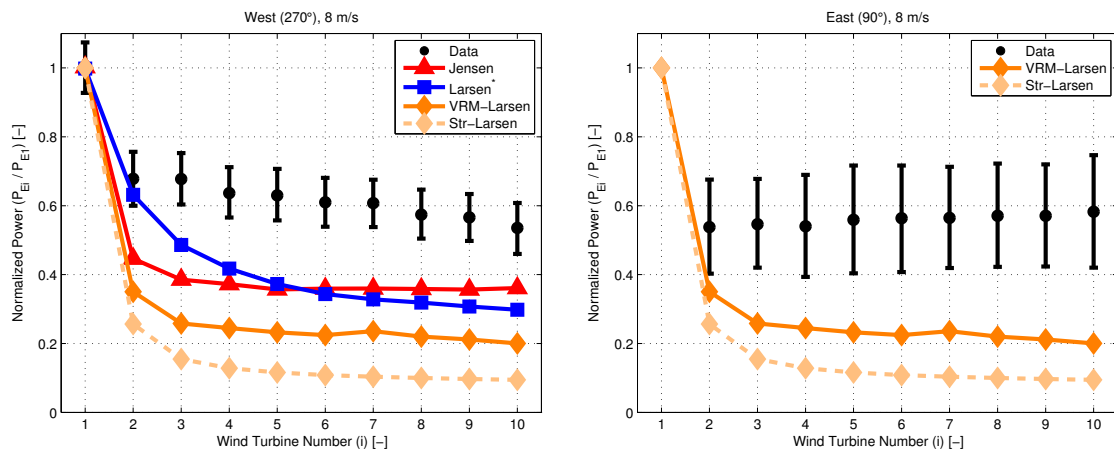


Figure 8.4: Axial velocity fields of the Horns Rev case from the streamtube-Larsen and VRM-Larsen simulations

outside of the $\pm 2.5^\circ$ bin or an increase in atmospheric turbulence. Gaumond et al. [17] states a misalignment in wind direction between the met mast and the upwind turbine as possible explanations for the difference. In addition to this, the difference between data and simulation results could partly be attributed to meandering of the wake.

There is a significant difference in measured power output between an Easterly and Westerly wind. Theoretically, there should be no difference, since both directions are parallel to the row alignment of the wind farm. Méchali et al. [39] states that the different locations of the met mast could explain this difference. The met mast used with the wind coming from the west is relatively far located from the measured row, north of the wind farm, while the Eastern met mast is much closer to the turbines (5 km).



- (a) Power predictions from the Str-Larsen and VRM-Larsen simulation compared with simulation (Jensen and Larsen*) and data results from Gaumond et al. [17]
- (b) Power predictions from the Str-Larsen and VRM-Larsen simulation compared with measurement data as published by Méchali et al. [39]

Figure 8.5: Normalised power predictions compared with measurements

Figure 8.5a also shows results from simulations performed by Gaumond et al. [17]. The results show a large difference between the Larsen model as implemented by Gaumond and the streamtube-Larsen model implemented in this research which was unexpected. The details of the Larsen model implemented by Gaumond are unfortunately untraceable², but a number of different reasons are discussed below.

Since the parameters of the wind turbines used in Horns Rev are known, it is likely that Gaumond used the BEM near-wake model in his simulations. In this model, the hub is disregarded and air is allowed to pass without interruption, resulting in a higher average velocity in the centre of the wake, which was observed in section 6.5. A slightly higher velocity in the wake results to a major power increase, since it has a cubed relation with wind speed.

The empirical constants used in Gaumonds EV-term are unknown. These constants determine the relative influence from ambient turbulence in wake recovery and the results

²In [17], details concerning the Larsen model are referred to: Larsen GC 2009, *A simple stationary semi-analytical wake model*, Risø-R-1713(EN) which is nowhere found in the Risø databases.

were found to be rather sensitive to variations in the these empirical constants. It is very likely that these constants differ from the streamtube-Larsen implementation, since Gaumond refers to a calibration performed at $9.6D$, while Madsen et al. [37] calibrated on the whole wake field from $2D$ till $10D$.

Gaumond could have averaged results from different wind directions, taking into account the bin width of 5° , which was not done in the current implemented Larsen models. It is unlikely that the difference can be completely attributed to this averaging, but it could be a contributing factor.

8.4 Conclusions from the Horns Rev Power Prediction Case

Power predictions from the VRM-Larsen and streamtube-Larsen models for a Horns Rev wind farm case are compared with literature. The case consists of a single array, where the wind turbines are fully immersed in the wake of upwind turbines. SCADA power output data is coupled with 10-minute averaged wind data from met masts to provide a benchmarking case.

All models underpredict the power output of the wind turbines. A difference is observed between the VRM-Larsen and streamtube-Larsen models and the Larsen model from literature. There are a lot of reasonable explanations for the difference, but nothing can be proven, since the details of the simulation from literature are unknown. What can be concluded is that the VRM-Larsen results in a less conservative power prediction, compared to the streamtube-Larsen model. The results of the VRM-Larsen model are slightly closer to the measured power output.

Chapter 9

Conclusion & Recommendations

This chapter provides a final discussion on the obtained results. The main conclusions of this thesis from a reflection on the research questions is presented in section 9.1. More general conclusions of this research are presented in section 9.2. Section 9.3 presents recommendations for further analysis on this research and some general recommendations on wake modelling.

9.1 Reflection on Research Questions

This section presents conclusions from a reflection on the initial research questions set in section 1.3.2.

1. A literature study was done on the current state-of-the-art of wake modelling to determine which far-wake models are most suitable for an alternative near-wake model. It is found that the near-wake in most current state-of-the-art wake models are a simple representation compared to the methodology used in the far-wake. The wake predictions of the Jensen and Larsen wake models have the potential to be improved by implementing a near-wake model based on discrete inviscid vortex rings.
2. The numerical implementation of the VRM resulted in two expansion models:
 - (a) A constrained expansion model from the actuator disc momentum theory which treats the rings as blade tip vortices.
 - (b) A free-wake expansion model where the vortex rings are allowed to expand/contract. A smaller timestep is required for numerical stability, thus losing the blade tip vortex character.

Both models are validated against wind tunnel measurements. The second model showed a better agreement with experimental results from an actuator disc represented by a porous mesh in terms of wake expansion and velocity deficit.

3. Implementing the VRM in the Jensen far-wake model was more difficult than anticipated due to the lack of near- and far-wake distinction. The VRM can be used to determine the initial wake deficit and expansion of the Jensen model. The Larsen model has a distinction between near- and far-wake and the near-wake model is easily substituted with the VRM. The resulting axial and radial velocities are used as input in the far-wake model based on the concept of Eddy Viscosity.
4. The coupled VRM-Jensen model generally results in a more gradual wake recovery as compared with the reference Jensen model, which is favourable. The coupling with the Jensen model was considered as a concept study and thus no further investigations were performed with it. The combined VRM-Larsen model results in a less conservative wake, with higher velocities in the near-wake, a thicker wake shear layer and a faster wake recovery, compared to the reference streamtube-Larsen model. The difference in centreline velocities between the Larsen models increases with incrementing thrust coefficient.

9.2 General Conclusions

A comparison of the VRM-Larsen and streamtube-Larsen models with an LES code, shows that the VRM captures the deceleration of the flow in agreement with the LES results. The far-wake results of the VRM-Larsen are in better agreement with LES as compared with the streamtube-Larsen model. This holds for a single turbine as well as two turbines placed parallel to the wind velocity. The LES model was found to be very time consuming, whereas the VRM-Larsen model maintains an engineering-type computational character.

A multiple wake case, where the model was used to calculate power deficits of the Horns Rev wind farm and compared with literature was inconclusive, since the ten-minute averaged wind velocity met mast data is not representative for the calculated case.

The Ainslie model based on a Gaussian near-wake distribution and the concept of Eddy Viscosity is very sensitive to the input of atmospheric turbulence. The implementation by Larsen is favoured over Ainslie due to a modern recalibration on the concept of Eddy Viscosity and the empirical constants used in the model. There is an inconsistency in the calibrated values used throughout literature on the Larsen deficit model which includes referenced untraceable reports.

The estimated transition of near-wake to far-wake in the Larsen model at $2D$ is accurate in low turbulence cases, but questionable in high thrust cases. The VRM model supports implementation at an arbitrary down-wake position, which is favourable over the BEM and actuator disc streamtube momentum near-wake models.

9.3 Recommendations

To speed up the simulation of the near-wake with the vortex ring model, computational parallelization of the workload is advised. The current implemented code is based on a single thread and takes roughly 15 minutes to determine the near-wake of a single turbine.

Dividing the workload over multiple cores or enabling GPU acceleration would speed up the calculations, should the model be used in a wind farm layout optimization scheme.

The VRM shows heavy vortex ring interaction down-stream. At this point, the flow can no longer be assumed inviscid. If a vorticity dissipation model could be derived, the VRM could predict wake velocities in the far wake as well. Recommended is a model which simulates energy dissipation from vortex ring interaction, thus reducing the strength of the vortex ring until it is dissipated in the free-stream.

The currently used LES model is only compatible with uniform laminar inflow, while even in offshore conditions, some atmospheric turbulence is present. When it is possible to implement a generated turbulence field as input boundary to the LES, a new comparison case is of interest, since the existence of atmospheric turbulence drives the wake recovery in the models using the concept of Eddy Viscosity. This would also make it possible to compare the results with a VRM-Jensen simulation.

A more documented case on power deficit in an array of wind turbines could be used instead of the Horns Rev case used in this research. Currently, 10-minute averaged wind velocity data is used which is prone to uncertainty in the measurements. Averaged wind velocities on a shorter time scale would be more accurate in this case. Absolute power output from the SCADA data instead of normalised to the power output of the first turbine would also make a fairer comparison.

References

- [1] M. Abramowitz, I. A. Stegun, and D. Miller. *Handbook of Mathematical Functions With Formulas, Graphs and Mathematical Tables*. United States Department of Commerce, 1st edition, 1964. ISBN 0486612724.
- [2] J. F. Ainslie. Calculating the flowfield in the wake of wind turbines. *Journal of Wind Engineering and Industrial Aerodynamics*, 27:213–224, 1988.
- [3] J. D. Anderson. *Fundamentals of aerodynamics*. McGraw-Hill, 3rd edition, 2001.
- [4] D. Baldacchino. Horizontal Axis Wind Turbine (HAWT) wake stability investigations, Delft University of Technology Master Thesis, 2012.
- [5] D. Baldacchino and G. J. W. van Bussel. Wind turbine wake stability investigations using a vortex ring modelling approach. *Journal of Physics: Conference Series*, 555: 012111, 2014. ISSN 17426596.
- [6] M. Bastankhah and F. Porté-Agel. A new analytical model for wind-turbine wakes. *Renewable Energy*, 70:116–123, 2014. ISSN 09601481.
- [7] F. Beyer, D. Matha, T. Sebastian, and M. A. Lackner. Development, Validation and Application of a Curved Vortex Filament Model for Free Vortex Wake Analysis of Floating Offshore Wind Turbines. In *Proceedings of the 50th AIAA aerospace sciences meeting including the new horizons forum and aerospace exposition*, Nashville, Tennessee, USA, 2012. AIAA.
- [8] E. T. G. Bot, G. P. Corten, and P. Schaak. A Program to Determine Energy Yield of Wind Turbines in a Wind Farm. Technical Report ECN-C-06-029, ECN Energy research Centre of the Netherlands, 2006.
- [9] J. Choi and M. Shan. Advancement of Jensen (Park) wake model. In *Proceedings of the EWEA Annual Meeting*, Vienna, 2013.
- [10] G. Corbetta, I. Pineda, and J. Moccia. The European offshore wind industry - key trends and statistics 2013. Technical Report January, EWEA, 2014.

- [11] B. Couët and O. Buneman. Simulation of Three-Dimensional with a Vortex-in-Cell. *Journal of Computational Physics*, 39:305–328, 1981.
- [12] A. Crespo, J. Hernandez, E. Fraga, and C. Andreu. Experimental validation of the UPM computer code to calculate wind turbine wakes and comparison with other models. *Journal of Wind Engineering and Industrial Aerodynamics*, 27:77–88, 1988.
- [13] E. Dellwik, L. Landberg, and N. O. Jensen. WAsP in the Forest. *Wind Energy*, 9: 211–218, 2006. ISSN 1095-4244.
- [14] W. P. Elliott. The growth of the atmospheric internal boundary layer. *Transactions, American Geophysical Union*, 39(6):1048–1054, 1958.
- [15] L. E. Fraenkel. On Steady Vortex Rings of Small Cross-section in an Ideal Fluid. *Proceedings of the Royal Society of London. Series A, Mathematical and Physical Sciences*, 316(1524):29–62, 1970.
- [16] S. Frandsen, R. Barthelmie, S. Pryor, O. Rathmann, S. Larsen, and T. Højstrup. Analytical modelling of wind speed deficit in large offshore wind farms. *Wind Energy*, 9:39–53, 2006.
- [17] M. Gaumond, P. E. Réthoré, A. Bechmann, S. Ott, G. C. Larsen, and A. Peña. Benchmarking of wind turbine wake models in large offshore wind farms. In *The Science of making Torque from Wind*, Oldenburg, 2012.
- [18] K. S. Hansen, R. J. Barthelmie, L. E. Jensen, and A. Sommer. The impact of turbulence intensity and atmospheric stability on power deficits due to wind turbine wakes at Horns Rev wind farm. *Wind Energy*, 15:183–196, 2012.
- [19] C. B. Hasager, L. Rasmussen, A. Peña, L. E. Jensen, and P. E. Réthoré. Wind farm wake: The Horns Rev photo case. *Energies*, 6:696–716, 2013. ISSN 19961073.
- [20] C. G. Helmis and K. H. Papadopoulos. An experimental study of the near-wake structure of a wind turbine operating over complex terrain. *Solar Energy*, 54(6): 413–428, 1995.
- [21] S. J. Hulshoff. Introduction to the Cluster, Blackboard Delft University of Technology, 2014.
- [22] L. E. Jensen, C. Mørch, P. B. Sørensen, and K. H. Svendsen. Wake measurements from the Horns Rev wind farm. In *European Wind Energy Conference*, London, UK, 2004.
- [23] N. O. Jensen. A Note on Wind Generator Interaction. Technical Report Risø-M-2411, DTU, Roskilde, 1983.
- [24] G. Kariniotakis, P. Pinson, N. Siebert, G. Giebel, and R. Barthelmie. The state of the art in short-term prediction of wind power - From an offshore perspective. In *French Sea tech week conference*, Brest, France, 2004.
- [25] I. Katic, J. Højstrup, and N. O. Jensen. A simple model for cluster efficiency. In *EWEC'86. Proceedings*, volume 1, pages 407–410, Rome, 1987. Raguzzi, A.

- [26] J. Katz and A. Plotkin. *Low-Speed Aerodynamics: From Wing Theory to Panel Methods*. McGraw-Hill, 1st edition, 1991.
- [27] R. E. Keck, M. Maré, M. J. Churchfield, S. Lee, G. Larsen, and H. A. Madsen. Two improvements to the dynamic wake meandering model: including the effects of atmospheric shear on wake turbulence and incorporating turbulence buildup in a row of wind turbines. *Wind Energy*, 18:111–132, 2013.
- [28] R. E. Keck, D. Veldkamp, H. A. Madsen, and G. C. Larsen. Implementation of a Mixing Length Turbulence Formulation Into the Dynamic Wake Meandering Model. *Journal of Solar Energy Engineering*, 134(2):021012, 2012. ISSN 01996231.
- [29] M. H. M. Kloosterman. Development of the Near Wake behind a Horizontal Axis Wind Turbine, Delft University of Technology Master Thesis, 2009.
- [30] O. M. Knio and R. Klein. Improved thin-tube models for slender vortex simulations. *Journal of Computational Physics*, 163:68–82, 2000. ISSN 00219991.
- [31] L. Landberg, G. Giebel, H. A. Nielsen, T. Nielsen, and H. Madsen. Short-term Prediction - An Overview. *Wind Energy*, 6:273–280, July 2003. ISSN 1095-4244.
- [32] G. C. Larsen, H. M. Aagaard, F. Bingöl, J. Mann, and S. Ott. Dynamic wake meandering modeling. Technical Report Risø-R-1607(EN), RisøNational Laboratory, Technical University of Denmark, Roskilde, 2007.
- [33] G. C. Larsen and P.-E. Réthoré. TOPFARM A Tool for Wind Farm Optimization. *Energy Procedia*, 35:317–324, 2013. ISSN 18766102.
- [34] G. C. Larsen, H. A. Madsen, J. Torben, and N. Troldborg. Wake modeling and simulation. Technical Report Risø-R-1653(EN), RisøNational Laboratory, Technical University of Denmark, Roskilde, 2008.
- [35] M. Lee, N. Malaya, and R. D. Moser. Petascale direct numerical simulation of turbulent channel flow on up to 786K cores. In *Super Computing*, pages 1–11, New York, New York, USA, 2013. ACM Press. ISBN 9781450323789.
- [36] L. E. M. Lignarolo, D. Ragni, C. J. Simão Ferreira, and G. J. W. van Bussel. Kinetic energy entrainment in wind turbine and actuator disc wakes: an experimental analysis. *Journal of Physics: Conference Series*, 524:012163, June 2014. ISSN 1742-6596.
- [37] H. A. Madsen, G. C. Larsen, T. J. Larsen, N. Troldborg, and R. Mikkelsen. Calibration and Validation of the Dynamic Wake Meandering Model for Implementation in an Aeroelastic Code. *Journal of Solar Energy Engineering*, 132(4):041014, 2010. ISSN 01996231.
- [38] J. F. Manwell, G. McGowan, and L. Rogers. *Wind Energy Explained*. Wiley, Amherst, USA, 1st edition, 2002. ISBN 0470846127.
- [39] M. Méchali, R. Barthelmie, S. Frandsen, L. Jensen, and P. E. Réthoré. Wake effects at Horns Rev and their influence on energy production. In *European Wind Energy Conference and Exhibition*, page 10, Athens, 2006. ISBN 9781622764679.

- [40] D. Mehta, A. van Zuijlen, and H. Bijl. Energy-conserving schemes for wind farm aerodynamics. *Journal of Physics: Conference Series*, 524:012157, 2014. ISSN 1742-6596.
- [41] D. Micallef, C. J. Simão Ferreira, T. Sant, and G. J. W. van Bussel. An Analytical Model of Wake Deflection Due to Shear Flow. In *The Science of making Torque from Wind*, Crete, 2010.
- [42] V. L. Okulov and G. A. M. van Kuik. The Betz-Joukowsky limit: on the contribution to rotor aerodynamics by the British, German and Russian scientific schools. *Wind Energy*, 15:335–344, 2012.
- [43] S. Øye. A Simple Vortex Model of a Wind Turbine Rotor. In *Proceedings of the Third IEA Symposium on the Aerodynamics of Wind Turbines*, Harwell, UK, 1989. Energy Technology Support Unit.
- [44] I. Pineda and J. Wilkes. Wind in power: 2014 European statistics. Technical Report February, EWEA, 2015.
- [45] O. Rathmann, R. Barthelmie, and S. Frandsen. Turbine wake model for wind resource software. In *Wind Energy Conference and Exhibition*, Athens, 2006.
- [46] O. Rathmann, S. Frandsen, and M. Nielsen. Wake decay constant for the infinite wind turbine array: Application of asymptotic speed deficit concept to existing engineering wake model. In *EWEC 2010 Proceedings online*, Warsaw, 2010.
- [47] B. Sanderse. *Energy-conserving discretization methods for the incompressible Navier-Stokes equations*. PhD thesis, Eindhoven University of Technology, 2013.
- [48] B. Sanderse, S. P. Pijl, and B. Koren. Review of computational fluid dynamics for wind turbine wake aerodynamics. *Wind Energy*, 14:799–819, 2011.
- [49] J. G. Schepers. Analysis of 4.5 years EWTW wake measurements. Technical report, ECN Energy research Centre of the Netherlands, Petten, 2009.
- [50] J. G. Schepers. *Engineering Models in Wind Energy Aerodynamics: Development, implementation and analysis using dedicated aerodynamic measurements*. PhD thesis, Delft University of Technology, 2012.
- [51] J. Smagorinsky. General circulation experiments with the primitive equations I. The basic experiment. *Monthly Weather Review*, 91:99–164, 1963. ISSN 0036-8075.
- [52] C. Steiness. Photograph of fog formation on the Horns Rev I offshore wind farm, Vattenfall, 2008.
- [53] A. Stidworthy, D. Carruthers, and J. Hunt. CERC activities under the TOPFARM project: Wind turbine wake modelling using ADMS. Technical Report FM766, Cambridge Environmental Research Consultants, Cambridge, 2011.
- [54] M. J. Stock. Summary of Vortex method Literature (A living document rife with opinion), Unpublished, 2007.

- [55] N. Troldborg, J. N. Sorensen, and R. Mikkelsen. Numerical simulations of wake characteristics of a wind turbine in uniform inflow. *Wind Energy*, 13:86–99, 2010.
- [56] G. A. M. van Kuik. The edge singularity of an actuator disc with a constant normal load. In *22nd AIAA/ASME Wind Energy Symposium*, Reno, 2003. ISBN 1563475944.
- [57] S. E. Widnall. The stability of a helical vortex filament. *Journal of Fluid Mechanics*, 54(04):641–663, 1972. ISSN 0022-1120.
- [58] J. Wilkes and J. Moccia. The european offshore wind industry key trends and statistics 2010. Technical Report January, EWEA, 2011.
- [59] R. E. Wilson. Wind turbine flow field model. *Journal of Solar Energy Engineering*, 108:344–345, 1986.
- [60] S. S. Yoon and S. D. Heister. Analytical formulas for the velocity field induced by an infinitely thin vortex ring. *International Journal of Numerical Methods in Fluids*, 44:665–672, 2004.
- [61] W. Yu, C. J. Simão Ferreira, G. A. M. van Kuik, and D. Baldacchino. Vortex ring model analysis of an actuator disc with dynamic and non-uniform load. *Paper in preparation*, 2014.

Appendix A

Prandtl's Lifting Line Method

In this method a finite wing is replaced by a vortex filament as can be seen in figure A.1. The Biot-Savart law states that the downwash of a wing can be modelled as the result of a vortex filament with strength Γ and position vector r with:

$$d\bar{V} = \frac{\Gamma}{4\pi} \frac{d\bar{l} \times \bar{r}}{|r|^3} \quad (\text{A.1})$$

Since the Helmholtz theorem states that a bound vortex cannot end in the fluid, free vortices emerge from the wing tips, which extend infinitely downstream. This results in a so-called Horseshoe vortex. This concept, which is known as 'Prandtl's Classical Lifting-Line Theory', is illustrated in figure A.1.

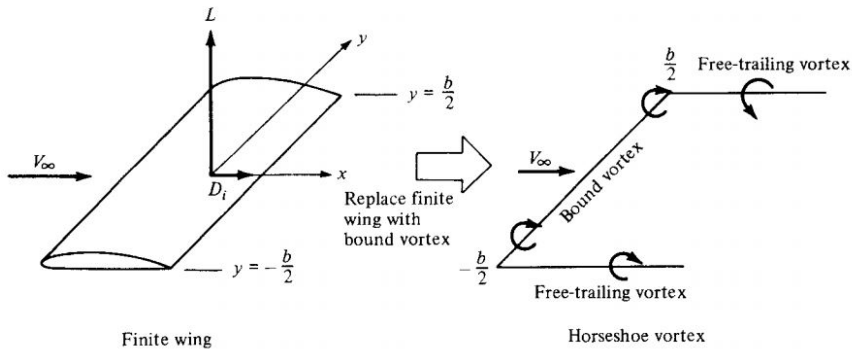


Figure A.1: Horseshoe Vortex as a result of a finite wing

To model the lift distribution of a finite wing, multiple horseshoe vortices of different strength are superimposed. The result is an approximation of the actual lift distribution, where the accuracy depends on the amount and order of discretization elements. The bound vortex is referred to as the lifting line, as seen in figure A.2.

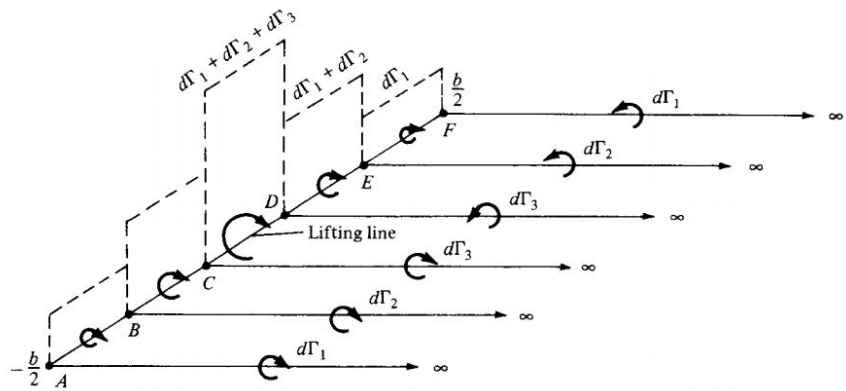


Figure A.2: Superposition of Horseshoe vortices resulting in the lifting line

The final lift distribution is obtained with the Kutta-Joukowski theorem, which relates the bound vortex strength to Lift:

$$L'(y) = \rho_\infty V_\infty \Gamma(y) \quad (\text{A.2})$$

Appendix B

Overview of Commercial Wake Modelling Software

This Appendix presents an overview of the current wake modelling software packages used in the industry. The origin of the software and the wake models that are implemented are described. The models are mainly used for wind farm development. All software packages offer a wide range of modelling techniques, not only containing wake modelling, but also wind resource, cost modelling, noise prediction and shadow flicker estimation.

B.1 WAsP

A widely used software package for wind farm development in the industry is WAsP. This program is developed by the University of Denmark (DTU). The first version of this program was released in 1987. Wake Modelling was mainly based on the Jensen model, but Eddy Viscosity was also implemented in later versions. The current version is WAsP 11.1 and includes a linearised CFD model for wind resource assessment in complex terrain (see figure B.1). Something which was already being developed from the 1990's[13] and is finally implemented. The CFD computation is fully automatic, which conserves the user-friendliness of the program.

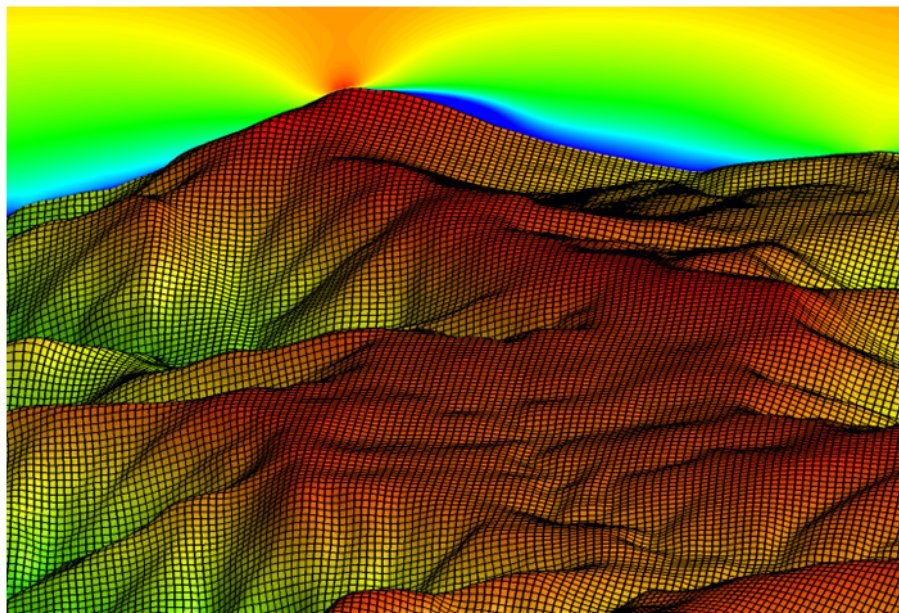


Figure B.1: Example of CFD Mesh creation in the new WAsP 11 program. Picture from wasp.dk

B.2 WindPro

WindPro is a software tool developed by EMD, a Danish company. It is a modular based design tool, which means the basic form can be extended which certain packages (e.g. Environmental Impact, Shadow, Decibel, Animation package). The advantage is that the customer does not have to pay for design features he/she doesn't want. The downside is that the basic module is very limited, so that the customer is pushed towards buying more modules. Figure B.2 shows an overview of the available modules. The current version of the software is 2.9.

Even though the software is very extensive, there is no wake model directly implemented. The MODEL module is basically an extension towards WAsP, which does all the calculations. It is unclear if a license to the WAsP program is included of if it is already implemented.

For instance, the basic version is priced at €1000. This is however without any additional modules that come standard with many other programs. If the Meteo, Park and Model package are added, the total package adds up to €4250. This with the assumption that a standalone license of WAsP is not required. A price comparison can be found in table B.2.

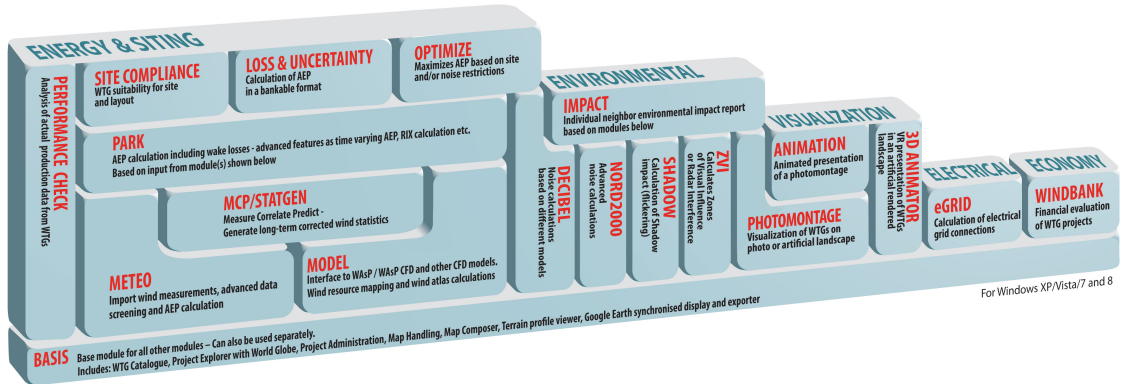


Figure B.2: Overview of the available modules for WindPro. Picture from emd.dk

B.3 WindFarmer

WindFarmer is a software tool which is developed by English consultants Garrad Hassan. GH is also known for the turbine design software tool Bladed. WindFarmer is also a modular program, however, compared to WindPro, the base module is already quite extensive. The current version's (5.2) base wake module consists of the Ainslie (EV) model and a RANS CFD model. This can be extended with a Turbulence Intensity module, which affects wake wind speeds and turbine power.

The Ainslie model in combination with the Turbulence Intensity module is suitable for a wide range of wind farm applications and will provide accurate and bankable wind power data. The CFD wake module is suitable for complex terrain scenarios. If necessary, WindFarmer can export and import data to WAsP, if the WAsP CFD model is required. However, this is not included in standard version.

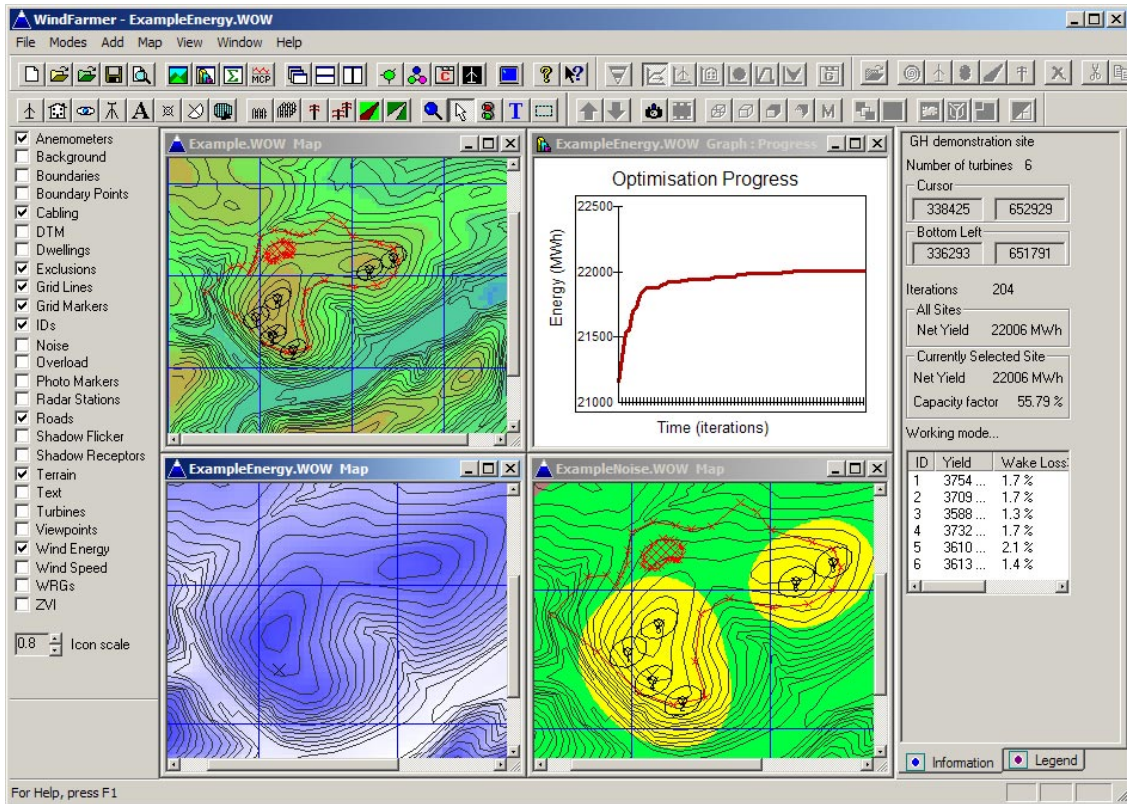


Figure B.3: Screenshot of the basic WindFarmer module. From the Windows 98 layout, it is assumed to be an older version. Picture from www.gl-garradhassen.com

B.4 WindFarm

Another software suite which is worth mentioning, is WindFarm from ReSoft. While the ReSoft website is slightly outdated, the current version (4.2.1.8) is supported by Windows 8. The software package is split into three suites; Designer & Utilities, Energy Yield & Optimisation and Visualisation.

The Energy Yield package provides the wake modelling software. The Wake Model supports Jensen and an Axi-symmetric models which is presumably the Ainslie model. It is possible to run WindFarm alongside WAsP if more extensive wake modelling is required, but this is not included in the default version and a separate WAsP license is required. Figure B.4 shows the wake model options in WindFarm. As earlier stated, the “axissymmetric” model is probably the Ainslie model (considering this model is used in the other software packages) but could also be a Larsen model, considering the “Include Wake Meandering” options listed. The figure also specifies Turbulence models which can be included.

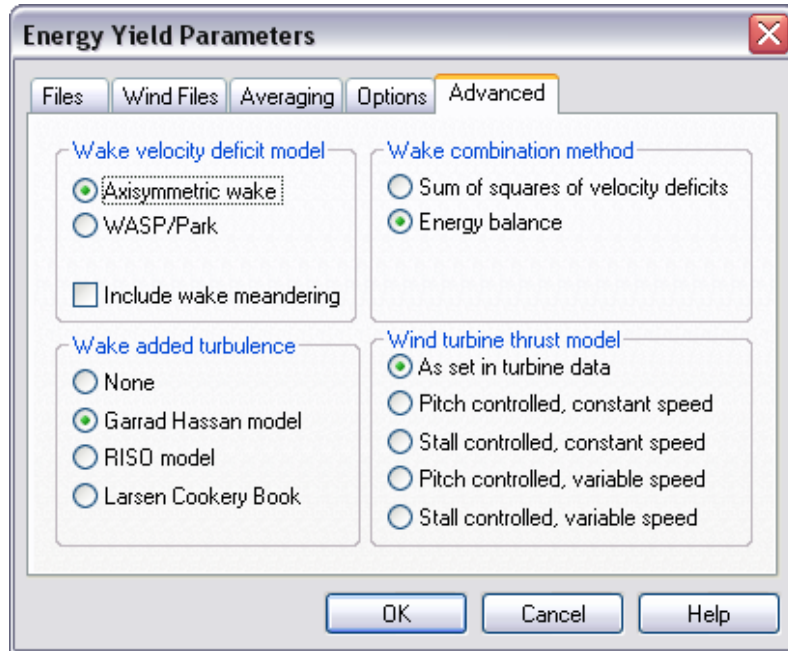


Figure B.4: Wake Model options in the WindFarm program. Picture from www.resoft.co.uk

B.5 Discussion on Commercial Wake Modelling Software

WAsP is currently the most advanced commercial wind turbine wake modelling software package. This is also clear from the fact that every other program supports data-formats used by WAsP and advertise this in their compatibility list. WindPro is even dependent on WAsP and WindFarm only supports relatively simplistic wake modelling. This makes WindFarmer from GH the only competitor to WAsP.

It is observed that the Larsen and Jensen model are often included in the program. This is perhaps due to these models being around for a longer period. It is clear what the strong and weak points of the model are. A trend is observed towards including a model based on CFD. This could be marketing, since CFD is still high on computational requirements. Table B.1 and B.2 sum up the findings of this small side-study.

Table B.1: Commercial Software Packages

Name	Developed by	Country	Models used
WAsP	DTU Risø	DK	Jensen, EV, CFD
WindPro	EMD International	DK	Wake model coupled to WaSP
WindFarmer	GL Garrad Hassan	UK	Jensen + EV + Turbulence Module
WindFarm	ReSoft	UK	Park + EV TI: Garrad Hassan Model + RISØModel
Topfarm	Various	EU	EV + CFD ACL + ADMS + Larsen
Fluxfarm	ECN	NL	UPMWAKE (WAKEFARM)
FLaP	University of Oldenburg	DE	unknown
openWind	AWS Truepower	USA	DAWM

Table B.2: Price Comparison of Commercial Wake Modelling Software

Software Package ¹	Single License [€]	License for 5 members [€]
WAsP	3600	10.800
WindPro ²	4250	9.350
WindFarmer	4800	12.000
WindFarm	3000	6.600

¹Prices are from 2014 and based on price listing on the official website, excluding VAT.

²It is unclear if an additional WAsP license is required.

Appendix C

Velocity Field Plots of the VRM-Larsen and Larsen Simulations

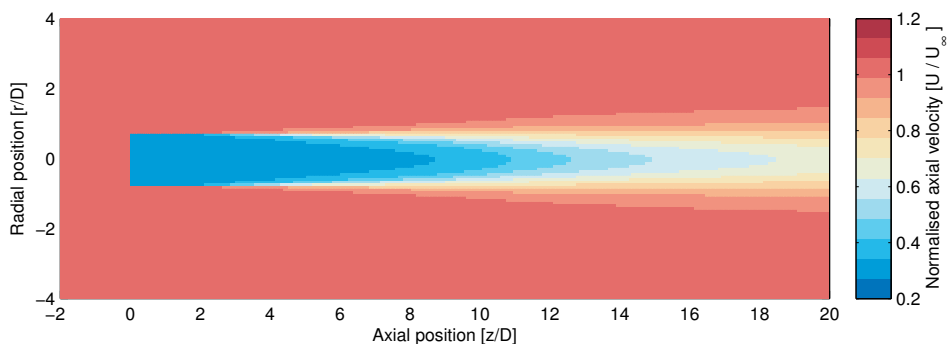


Figure C.1: Velocity field of a turbine operating at $C_T = 8/9$ in $TI = 0\%$ from the Larsen model

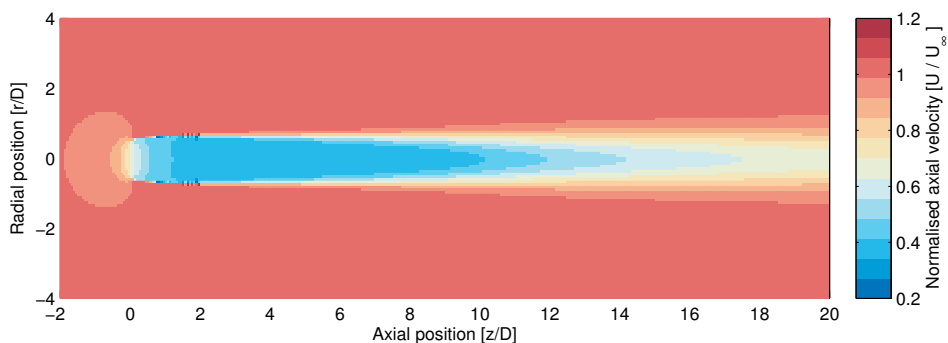


Figure C.2: Velocity field of a turbine operating at $C_T = 8/9$ in $TI = 0\%$ from the VRM-Larsen model

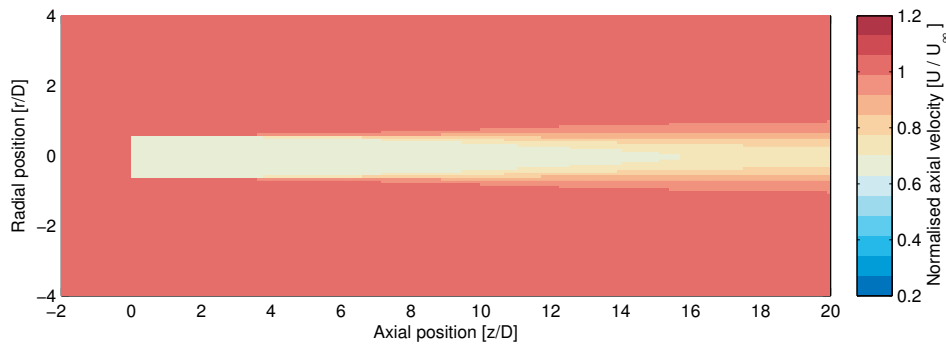


Figure C.3: Velocity field of a turbine operating at $C_T = 5/9$ in $TI = 0\%$ from the Larsen model

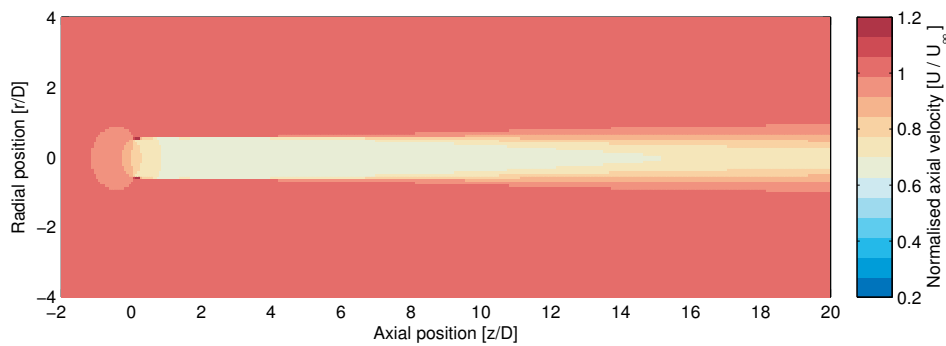


Figure C.4: Velocity field of a turbine operating at $C_T = 5/9$ in $TI = 0\%$ from the VRM-Larsen model

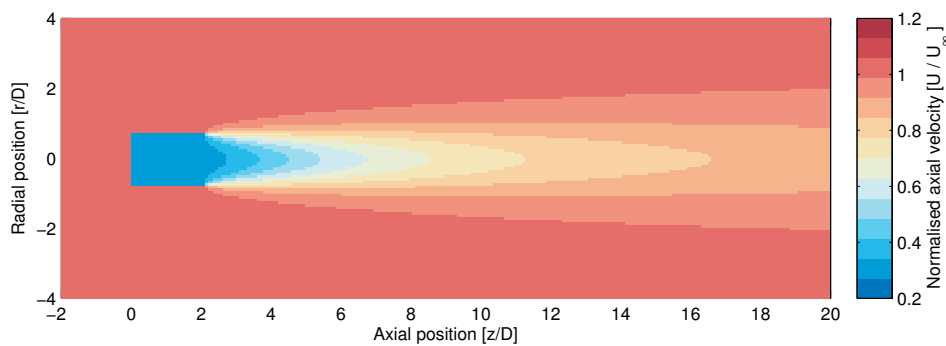


Figure C.5: Velocity field of a turbine operating at $C_T = 8/9$ in $TI = 25\%$ from the Larsen model

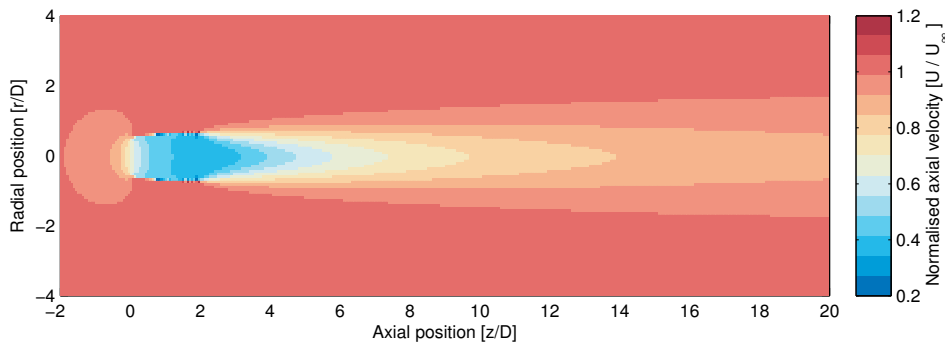


Figure C.6: Velocity field of a turbine operating at $C_T = 8/9$ in $TI = 25\%$ from the VRM-Larsen model

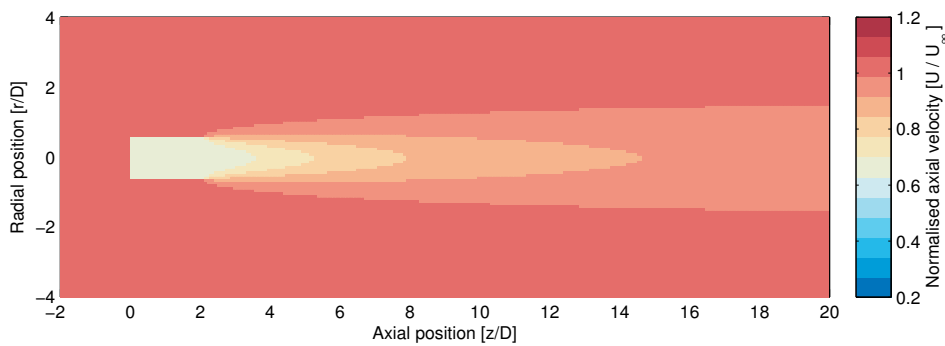


Figure C.7: Velocity field of a turbine operating at $C_T = 5/9$ in $TI = 25\%$ from the Larsen model

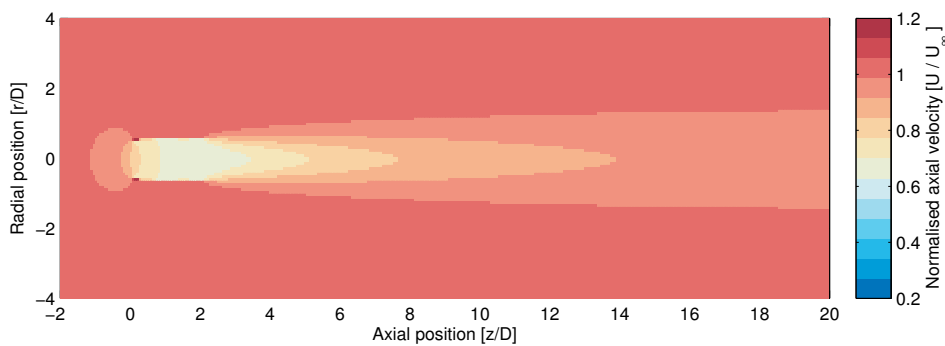


Figure C.8: Velocity field of a turbine operating at $C_T = 5/9$ in $TI = 25\%$ from the VRM-Larsen model



Appendix D

Velocity Field Plots of the Double Turbine LES Simulation

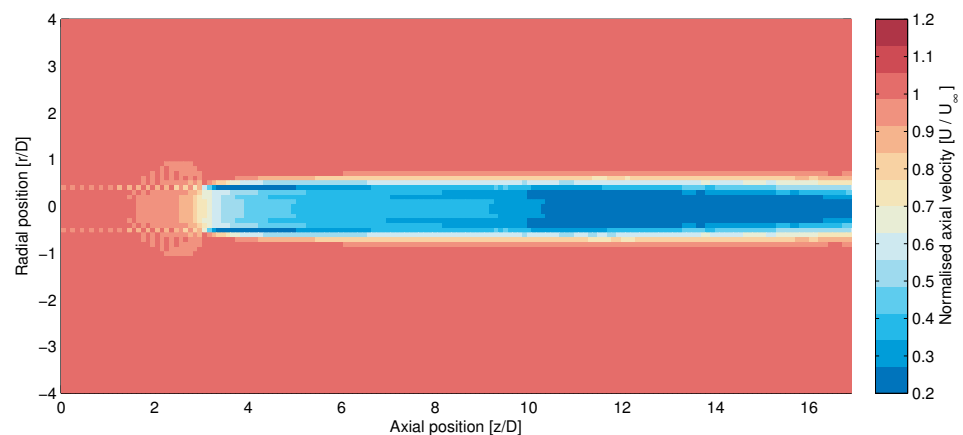


Figure D.1: Velocity field two turbines operating at $C_T = 8/9$ in $TI = 0\%$ from the LES model

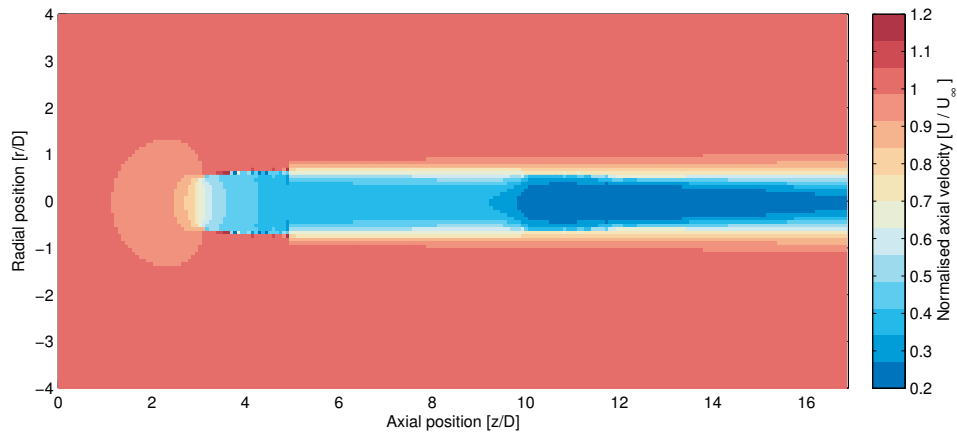


Figure D.2: Velocity field two turbines operating at $C_T = 8/9$ in $TI = 0\%$ from the VRM-Larsen model

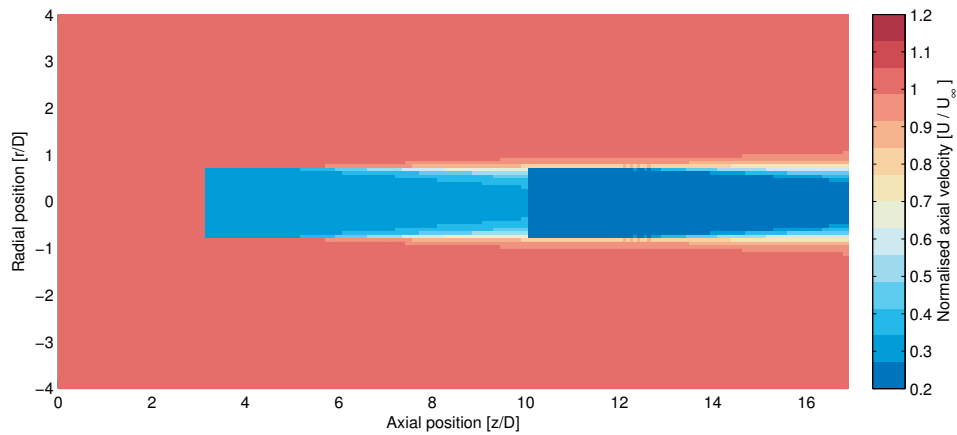


Figure D.3: Velocity field two turbines operating at $C_T = 8/9$ in $TI = 0\%$ from the streamtube-Larsen model